SPATIAL RELATIONSHIPS BETWEEN TREES AND SNOW IN A COLD REGIONS MONTANE FOREST

A Thesis Submitted to the
College of Graduate and Postdoctoral Studies
In Partial Fulfillment of the Requirements
For the Degree of Master of Science
In the Department of Geography and Planning
(Centre for Hydrology)
University of Saskatchewan
Saskatoon, Canada

By
Jacob W. Staines

© Copyright Jacob William Staines, September 2021. All rights reserved.
Unless otherwise noted, copyright of the material in this thesis belongs to the author.

Permission to use

In presenting this thesis in partial fulfillment of the requirements for a Master of Science degree from the University of Saskatchewan, I agree that the Libraries of this University may make it freely available for inspection. I further agree that permission for copying of this thesis in any manner, in whole or in part, for scholarly purposes may be granted by the professor or professors who supervised my thesis work or, in their absence, by the Head of the Department or the Dean of the College in which my thesis work was done. It is understood that any copying or publication or use of this thesis or parts thereof for financial gain shall not be allowed without my written permission. It is also understood that due recognition shall be given to me and to the University of Saskatchewan in any scholarly use which may be made of any material in my thesis.

Disclaimer

Reference in this thesis to specific commercial products, processes, and services by trade name, trademark, manufacturer, or otherwise, do not constitute or imply endorsement, recommendation, or favouring by the University of Saskatchewan. The views and opinions of the author expressed herein do not state or reflect those of the University of Saskatchewan and shall not be used for advertising or product endorsement purposes.

Requests for permission to copy or to make other uses of materials in this thesis/dissertation in whole or part should be addressed to:

Head of the Department of Geography and Planning
Kirk Hall Building, 117 Science Place
University of Saskatchewan
Saskatoon, Saskatchewan S7N 5C8 Canada

Or

Dean
College of Graduate and Postdoctoral Studies
University of Saskatchewan
116 Thorvaldson Building, 110 Science Place
Saskatoon, Saskatchewan S7N 5C9 Canada

Abstract

Vegetation structure is one of the primary factors that drives spatial variation of snow accumulation in forests due to interactions between falling snow, intercepted snow, and the forest canopy. These processes result in spatially heterogeneous snowpacks and snowpack energy fluxes, driving areal snow cover depletion rates during melt periods with repercussions for stand- and basin-scale ablation rates and snowmelt runoff quantities and timings. While spatial variation of forest snowpack has been documented at scales from individual tree branches to forest stands, the underlying processes are not fully understood. Understanding these relationships is critical to understanding the combined effects of climate and vegetation changes on streamflow and ecology in basins with seasonal snowpacks. To better understand these processes, this study examined the spatial relationships between branch-scale canopy structure and subcanopy snow accumulation over two accumulation events in February of 2019, at an instrumented montane forest site in Marmot Creek Research Basin on the eastern slope of the Canadian Rockies. Repeated UAV lidar surveys were paired with manual snow surveys to produce estimates of snowpack snow water equivalent (SWE) and change in snowpack (ΔSWE) over each event at high spatial resolutions. Lidar observations of the forest canopy were combined with contemporary hemispherical photography to produce a diverse set of canopy metrics, including light transmittance metrics from a novel voxel ray sampling method. Results showed that over 75% of the spatial variance in subcanopy ΔSWE for each event was found within 2.0 m of horizontal distance, indicating that the spatial scale of canopy effects on snow interception and redistribution were primarily found at the scale of tree branches in this forest. Significant vertical asymmetry was seen in the relationships between snow accumulation and surrounding vegetation which was explained by prevailing wind directions. A descriptive Gaussian snowfall model that was consistent with the tight coupling observed between near-overhead canopy characteristics and snow accumulation explained more of the spatial variation in observed ΔSWE than any canopy metric considered and performed better than two other forest snow accumulation models based on larger scale canopy characteristics found in the literature. These findings emphasize the importance of representing branch-scale forest heterogeneity in models of snow accumulation and suggest that representation of vertical asymmetry in parametrizations of snow-vegetation relationships may yield more physically realistic models.

Acknowledgements

This is a story about relationships between water and trees, people and land. It unwinds on the homeland of the Îyârhe Nakoda of Bearspaw, Chiniki, and Wesley First Nations, Tsuut'ina First Nation, those of the Blackfoot Confederacy, and Métis Nation. My relationship with this land is braided with my relationship with its Indigenous Peoples, guided by Treaty 7 and a commitment to working toward a respectful future through a shared journey of reconciliation.

This is a story of curiosity and collaboration to understand the collective stories written in snow by trees and wind. These stories were gathered with the hard work and bright energy of Greg Galloway and Robin Heavens, in the field and out. These stories were recorded and translated with empowering technical support from Phillip Harder, Dong Zhao, and Alistair Wallace. Their interpretations were supported by many encouraging conversations: within the community with Caroline Aubry-Wake, Stephan Boraks, Alex Cebulski, Natasha Hardy, Lindsey Langs, Nicolas Leroux, Daniel Nadeau, Karling Roberts, Kevin Shook, Paul Whitfield, and Ching Yu; with my research committee of Krys Chutko, Martyn Clark, and Nicholas Kinar; and in the many meetings shared with my adviser John Pomeroy.

I am immensely grateful for the support of my family – my grandmothers, parents, sister, brother, and nephew – for their inspiration and unconditional love that kept this story going. And for my research partner and life partner, María Elisa Sanchez Garcés, for sharing her perspective when my doubts overflowed and for being my partner in curiosity through it all.

Contents

Permission to use ii
Disclaimer ii
Abstract iii
Acknowledgements iv
Contents v
List of Tables viii
List of Figures x
List of Symbols xv
Thesis body 1
Chapter 1: Introduction 1
1.1 Motivation and relevance 1
1.2 Research background 2
1.2.2 Snow accumulation in forests 4
1.2.3 Measuring forest snow accumulation 6
1.2.4 Modeling forest snow accumulation 9
1.2.5 Characterizing vegetation structure for explaining snow accumulation processes . 12
1.2.6 Canopy light transmittance 14
1.3 Research gaps 16
1.4 Research design 19
1.4.1 Research purpose 20
1.4.2 Research objectives and questions 20
1.4.3 Thesis layout 20
Chapter 2: Methodology 21
2.1 Study site and period 21
2.2 Data collection 25
2.2.1 Field visits 25
2.2.2 UAV-lidar data collection and preprocessing 27
2.2.3 Snow surveys 29
2.2.4 Hemispherical photography 29
2.3 Lidar snow products 29

2.3.1 Lidar snow depth 29
2.3.2 Lidar SWE 30
2.3.3 Lidar ΔSWE 30
2.3.4 Rejection sampling of airborne lidar snow products 31
2.4 Lidar canopy products 33
2.4.1 Vegetation characterization from lidar point cloud reprojection 33
2.4.2 Vegetation characterization from voxel ray sampling of lidar 35
2.4.3 Other canopy metrics 40
2.5 Parameterizing canopy structure for modeling spatial variation of snow accumulation 42
2.5.1 Hedstrom-Pomeroy model 43
2.5.2 Moeser et al. model 44
2.5.3 Gaussian snowfall model 44
2.6 Conclusions 46
Chapter 3: Assessing the effects of beam occlusion on UAV lidar observations of snow and vegetation in forests 47
3.1 Introduction 47
3.2 Methods 48
3.3 Results 49
3.4 Discussion 56
3.4.1 Effects of sample bias with vegetation on areal snow depth distributions 56
3.4.2 Sources of error in estimating canopy metrics 58
3.5 Conclusions 61
Chapter 4: Relating spatial patterns of snow accumulation to branch-scale canopy structure . 62
4.1 Introduction 62
4.2 Methods 62
4.2.1 Describing spatial distributions of snow and canopy metrics 62
4.2.2 Quantifying spatial relationships between snow and canopy metrics 64
4.2.3 Exploring physical processes relating snow and canopy 64
4.3 Results 65
4.3.1 Spatial distributions of snow and canopy metrics 65
4.3.2 Spatial relationships between snow and canopy metrics 76

4.3.3 Physical processes relating snow and canopy 79
4.4 Discussion 83
4.4.1 Physical processes driving snow-vegetation relationships 83
4.4.2 Modeling spatial variation of snow accumulation in forests 86
4.4.3 Assessing canopy metrics for modeling snow accumulation 89
4.4.4 Feedbacks between snow interception and canopy structure 91
4.5 Conclusions 91
Chapter 5: Conclusions 93
5.1.1 Future directions 94
Chapter 6: References 96
Appendices 105
Appendix A: Surveys beyond study period 105
Appendix B: Validation of lidar snow depth, density, and SWE estimates 106
Appendix C: Optimization of light transmittance from lidar point cloud reprojection 110
Appendix D: Parameter fitting of contact number correction factor ωcχ for voxel ray sampling of lidar 112
..... 112
Appendix E: Sensitivity analysis of band-wise ray sampled contact number 113
Appendix F: Sensitivity analysis of Gaussian snowfall model parameters 120

List of Tables

Table 2.1: Survey dates and corresponding snow observations. Cumulative precipitation measured by the precip. gauge is reported from 1 October 2018. A linear snow density with depth relationship was assumed for the clearing plot with slope and intercept values shown, while a constant density was assumed within the forest plot, for each day. The final survey on 29 May 2019 was used for analysis of the snow-free ground surface. Two additional surveys conducted outside of the study period were omitted from analysis (see Appendix A). 28

Table 2.2: Interval dates and corresponding snow observations. Two additional intervals fell outside of the study period and were not considered in analysis (see Appendix A). 31

Table 2.3: Canopy metrics calculated from hemispherical analysis of synthetic hemispheres generated by reprojection of the lidar point cloud from snow-off canopy conditions surveyed on 27, May 2019 and are annotated (•) to differentiate metrics from similar metrics calculated by voxel ray sampling of lidar (▲ or △). 34

Table 2.4: Canopy metrics calculated from voxel ray sampling of lidar. All ray sampling metrics are annotated to distinguish between snow-off (▲) and snow-on (△) canopy conditions, and to differentiate from similar metrics calculated from point reprojection for snow-off canopy conditions (•)..... 39

Table 2.5: Additional canopy metrics considered in analysis with snow products 40

Table 3.1: Snow depth (HS_{lidar}) means (a) and standard deviations (b) for areal distributions over the forest and clearing plots and for all three survey days, calculated using rejection sampling, full interpolation, and limited interpolation methods. 49

Table 3.2: Root mean squared error (RMSE) of band-wise light transmittance estimated from lidar point cloud reprojection ($T_{a\text{-}b}^{\bullet}$) and from voxel ray sampling of lidar ($T_{a\text{-}b}^{\blacktriangle}$), compared with corresponding values from thresholded hemispherical photography of the snow-off canopy (n=15)..... 53

Table 4.1: Canopy metrics calculated over the forest plot for spatial analysis with SWE and ΔSWE estimates, and the canopy conditions and methodology sources used for their calculation. 63

Table 4.2: Areal means μ and coefficients of variation (c_v) of SWE over the forest and clearing plots, calculated from distributions corrected for sample bias with vegetation by rejection sampling..... 66

Table 4.3: Aggregate statistics of canopy metrics over the forest plot. Medians are reported for both the set of all pixels and the set of canopy pixels only, defined by CHM ≥ 1 m. 68

Table 4.4: Spearman's rank correlation coefficient (ρ_s) calculated between snow metrics (across) and select canopy metrics (down) over the forest plot. Canopy metric flags correspond to ray sampling under snow on (△) and snow-off (▲) canopy conditions, and snow-off point cloud

reprojection (•) methods. Significant ρ_s values are marked with an asterisk (*). Corresponding p-values are shown in parentheses below ρ_s for p-value > .001 only. 77

Table A.1: Snow survey observations for two dates lying outside of the study period..... 105

Table A.2: Interval dates and corresponding snow observations for two intervals lying outside of the study period..... 105

List of Figures

Figure 1.1: A conceptual diagram of water mass flux processes between the atmosphere, canopy, and snowpack systems. Labeled arrows correspond to each process and indicate the positive direction of flux in and out of each system (length is not representative of flux magnitudes). Arrows are colored by water phase: solid (blue), liquid (green), and vapour (red). 3

Figure 1.2 – Reproduced from Schmidt and Gluns (1991): A schematic illustrating the physical processes of bouncing (rebounding), bending (branch compression), and snow bridging at the branch scale from various perspectives, and under three snow loads..... 7

Figure 1.3 – Reproduced from Moeser, Stähli, et al. (2015): An example of two contradictory families of interception models found in the literature: the Moeser et al. sigmoidal model (black) first suggested by Satterlund and Haupt (1967), and the Hedstrom-Pomeroy exponential model (green). 11

Figure 2.1: (a) Site overview from satellite imagery (Google maps). Lidar-derived snow and canopy metrics were calculated over the extent of the site boundary (green), which was derived from a 15 m buffer of the outermost UAV flight path. Canopy structure analysis considered vegetation up to 50 m away from each ground point, with the outermost canopy extent shown in blue. Plot-specific analysis was conducted separately for each of the forest (red) and clearing (yellow) plots. (b) Locations of snow survey transects and meteorological stations within the site, plotted over an orthomosaic of the site generated from UAV photography collected on 21 Feb. 2019 and compiled using structure from motion with the Pix4D software (v. 4.6.2). 21

Figure 2.2: (top) clearing meteorological station on morning of 21 Feb. 2019, after storm 2. 22

Figure 2.3: (bottom) aerial view of clearing meteorological station in April 2013 (photo credit: John Pomeroy). 22

Figure 2.4: Changes in cumulative precipitation, tree lysimeter mass, and snow depths in the clearing and forest over the study period relative to the first survey date (Feb. 14). Dashed vertical lines correspond to the three field visits on 14, 19, and 21 of Feb. 2019. Two storms passed over the site over the study period which were bounded by surveys: storm 1 between 14 Feb. and 19 Feb. surveys, and storm 2 between 19 Feb. and 21 Feb. surveys. 23

Figure 2.5: Normalized histograms of wind speed (m s^{-1}) and wind direction (° clockwise from north, upward looking) over the storm 1 (a) and storm 2 (b) observation periods. The upward-facing perspective from the ground (flipped east-to-west from conventional downward-facing perspective) is used for simplified visual comparison with hemispherical analysis in Figure 3.3 and Figure 4.12. Plots were generated using the Python windrose package (v.1.6.8)..... 24

Figure 2.6: (left) Snow in the trees and on the ground at the field site and (right) view of the clearing tower meteorological station on 14 Feb. 2019 25

Figure 2.7: Several examples of intercepted snow on vegetation observed on visits to the field site. 26

Figure 2.8: (left) Preparation of the UAV and lidar systems at the field site on 17 April 2021. (right) UAV platform in operation (photo credit: Alistair Wallace)..... 27

Figure 2.9: Data workflow for voxel ray sampling of lidar, with data inputs (blue), processes (white), and data products (green). 35

Figure 3.1: Histograms of the lidar snow depth (HS_{lidar}) distributions within the forest (a) and clearing (b) plots for 19 Feb. 2019 using three resampling methods: limited interpolation (blue), full interpolation (green), and rejection sampling after limited interpolation (orange). Relative frequency distributions of laser penetration metric LPM-L over the forest (c) and clearing (d) plots, for all pixels (orange) and for the extent of the limited interpolation HS_{lidar} estimates for 19 Feb. 2019 (blue). 51

Figure 3.2: Normalized frequency distribution of canopy return height [m AGS] over the forest plot using the observed lidar point cloud (blue) and a resampled point cloud (orange) generated from voxel ray sampling of lidar. 52

Figure 3.3: Clockwise from top left: a) Hemispherical photograph which is subsequently thresholded (b) to differentiate canopy and sky pixels for estimating transmittances and contact numbers over zenith angle bands. c) A respective synthetic hemispherical image generated from reprojection of the lidar point cloud. d) Respective light transmittance estimates along hemispherical rays calculated by voxel ray sampling of lidar. All hemispherical images are shown from the upward-facing perspective, with north to the top and east to the left. 54

Figure 3.4: Comparisons of (a) light transmittance and (b) contact number estimates from synthetic hemispheres generated by lidar point cloud reprojection (x-axis) with those from voxel ray sampling of lidar (y-axis) for each of the four zenith angle analysis rings, with 1-to-1 line. (c) Comparison of leaf area index (LAI_{2000}) between the two methods, with 1-to-1 line. Synthetic hemispheres used in analysis were generated over a 1 m square grid of the forest plot (n = 1944). 55

Figure 4.1: Snow water equivalent SWE_f using the forest snow density assumption for 19 Feb. 2019 at 5 cm spatial resolution over the site (closeup on right). SWE maps were generated for all three survey dates using both the forest and clearing density assumptions. Gaps in observations (shown in grey) correspond to regions greater than 10 horizontal cm from lidar snow depth observations. 66

Figure 4.2: Change in snow water equivalent ΔSWE_f estimates for storm 1 (top) and storm 2 (bottom) calculated at 5 cm resolution over the siteusing the new snow density estimated for the forest. Gaps in observations are shown in gray. Tracks can be seen in both cases where snow was disturbed while conducting snow surveys, illustrating a clear violation of the snow density assumptions. All human-disturbed regions were masked prior to analysis. A close-up of the outlined square region is shown on the right. 69

Figure 4.3: (top) Lateral distance to nearest tree (DNT) in meters calculated at 10 cm resolution across the site, using tree-tops to identify trees and assuming vertical trunks. Treetops were identified from the canopy crown height model derived from the snow-free lidar point cloud following Khosravipour et al. (2016). A close-up of the outlined square region is shown on the right. 70

Figure 4.4: (bottom) Lateral distance to canopy edge (DCE) over the site, calculated from the lidar-derived canopy crown height model with 2 m AGS constituting the canopy edge following Mazzotti et al. (2019). A close-up of the outlined square region is shown on the right. 70

Figure 4.5: (top) Mean canopy height (MCH) [m AGS] calculated at 10 cm resolution over the site from the snow-free lidar point cloud following Khosravipour et al (2016). A close-up of the outlined square region is shown on the right. 71

Figure 4.6: (bottom) Laser penetration of canopy (LPM-L) calculated at 10 cm resolution across the site from near vertical (± 15°) lidar samples. A close-up of the outlined square region is shown on the right. 71

Figure 4.7: Contact numbers calculated for vertical rays (left) and rays 22.5° from zenith to the southeast (right) across the site at 25 cm resolution, from voxel ray sampling of the snow-free lidar point cloud. Contact numbers were calculated for over 30,000 ground points over the Forest plot at 1° angular resolution over the upper hemisphere, and for both snow-on and snow-off canopy conditions, for analysis with snow observations. 72

Figure 4.8: Clockwise from upper-left: (a) Mean light transmittance of the forest canopy in snow-on conditions (i.e. including intercepted snow) over the upper hemisphere, and (b) averaged by zenith angle and direction and shaded by standard deviation. (c) Comparison of mean light transmittances and (d) extinction efficiencies with zenith angle for snow-on and snow-off canopy conditions. 73

Figure 4.9: Distributions of (a) SWE_f and (b) ΔSWE_f within the forest plot and (c) SWE_c and (d) ΔSWE_c within the clearing plot, for all dates and intervals over the study period. All distributions were adjusted for sample bias by rejection sampling using the laser penetration metric LPM-L as a reference distribution. 74

Figure 4.10: SWE distributions corrected for sample bias and fitted lognormal distributions (left) and the corresponding Q-Q plots with model fit (right) for each survey day. Mean and standard deviation of the modeled lognormal distributions correspond to the intercept and slope of the respective Q-Q plot linear regression, following (Shook and Gray, 1997). 75

Figure 4.11: Variance with lag distance as a fraction of variance at 30 m for sets of sampled point pairs from (a) SWE and ΔSWE products and (b) ray sampled snow-off LAI metrics..... 78

Figure 4.12: (a) Spearman's correlation coefficient (ρ_s) between snow-on light transmittance of the snow-on canopy ($T^{\triangle}$) and ΔSWE_f for storm 1 (a), ΔSWE_f for storm 2 (b), and SWE_f for 21 Feb. 2019 (c) for angles across the hemisphere. The difference in colormaps represents a scale

change in ρ_s. $T^{\triangle}$ was calculated at 1° angular resolution across hemisphere, with nonsignificant values shaded in grey ($\alpha = 0.05$). All plots are shown using the upward-facing perspective from the ground, with north to the top and east to the left. 80

Figure 4.13: Scatter plots of observed ΔSWE_f within the forest (x-axis) vs. throughfall estimates (y-axis), for storm 1 (left) and storm 2 (right) modeled by Hedstrom-Pomeroy (top), Moeser et al. (middle), and the Gaussian snowfall (bottom) models. Spearman's rank correlation coefficients (ρ_s) are shown in the bottom right corner for each plot, with all corresponding p-values < 0.001 82

Figure B.1: Lidar snow depth bias with manual snow depth measurements for each Julian day (45, 50, …). 106

Figure B.2: Lidar snow depth validation with snow survey observations: (a) fractional error, (b) mean bias, and (c) root mean squared error (RMSE), after correction for mean bias of snow depth, for each Julian day within the study period (45, 50, 52). 107

Figure B.3: (a) Snow depth vs. density and (b) Snow depth vs. SWE from snow survey observations for each day, plotted with corresponding density models (Model parameters are reported in Table 2.1). 108

Figure B.4: Lidar SWE estimated using the Hedstrom-Pomeroy (1998) fresh snow density assumption compared with snow survey observations: (a) fractional error, (b) mean bias, and (c) root mean squared error (RMSE). 109

Figure C.1: (a) Weighted root mean squared error (WRMSE) and (b) weighted mean bias (WMB) of light transmittance calculated from synthetic hemispheres from lidar point cloud reprojection compared with values from corresponding hemispherical photographs taken below the canopy under snow-off canopy conditions (n = 15). 110

Figure C.2: Comparisons of band-wise light transmittance estimated from lidar point cloud reprojection (x-axis) with light transmittance estimated from thresholded hemispherical photography (y-axis) of the snow-off canopy, for the optimized point size scalar value of s = 0.063. 111

Figure D.1: Comparisons of band-wise light transmittance estimated by ray sampling (x-axis) with corresponding values from thresholded hemispherical photography (y-axis) for (a) snow-on and (b) snow-off canopy conditions. 112

Figure E.1: Comparison of contact numbers by zenith angle bands calculated by voxel ray sampling of lidar at 1° (x-axis) vs. 0.18° (y-axis) angular resolutions over the upper hemisphere, for (a) snow-on and (b) snow-off canopy conditions. 113

Figure E.2: Comparison contact numbers by zenith angle bands calculated by voxel ray sampling of lidar for rays up to a maximum distance of 50 m (x-axis) vs. 150 m (y-axis) from the origin, for (a) snow-on and (b) snow-off canopy conditions. 114

Figure E.3: Band-wise contact numbers calculated from mean thresholded transmittance (x-axis) vs. mean transmittance (y-axis) for voxel ray sampling optimization products, for (a) snow-on and (b) snow-off canopy conditions. Transmittances were thresholded at T = 0.772, represented by the Heaviside function H(T – 0.772). 116

Figure E.4: Band-wise contact numbers calculated by the natural logarithm of mean band-wise light transmittance (x-axis) compared with mean band-wise contact number (y-axis), for (a) snow-on and (b) snow-off canopy conditions, calculated from voxel ray sampling prodcts collocated with corresponding hemispherical photography. 116

Figure E.5: Comparisons of (a) light transmittance and (b) contact number estimates from synthetic hemispheres generated by thresholded voxel ray sampling of lidar (x-axis) with those from unthresholded voxel ray sampling of lidar (y-axis) for each of the four zenith angle analysis bands, with 1-to-1 line. (c) Comparison of leaf area index (LAI_{2000}) between the two methods, with 1-to-1 line..... 118

Figure E.6: Comparisons of (a) light transmittance and (b) contact number estimates from synthetic hemispheres generated by lidar point cloud reprojection (x-axis) with those from thresholded voxel ray sampling of lidar (y-axis) for each of the four zenith angle analysis rings, with 1-to-1 line. (c) Comparison of leaf area index (LAI_{2000}) between the two methods, with 1-to-1 line. 119

Figure F.1: Optimization landscape of (a) standard deviation (σ) and (b) snow contact absorption coefficient (ω^*) for ΔSWE_f for Storm 1. 120

Figure F.2: Optimization landscape of (a) standard deviation σ and (b) snow contact absorption coefficient ω^* for ΔSWE_f for Storm 2. 120

Figure F.3: Optimization landscape of (a) standard deviation σ and (b) snow contact absorption coefficient ω^* for SWE_f for 21 Feb. 2019. 121

List of Symbols

Abbreviations

AGS	above ground surface
AMSL	above mean sea level
Lidar	light detection and ranging
UAV	uncrewed aerial vehicle
LPM	laser penetration metric
GNSS	Global Navigation Satellite System
TIN	triangular irregular network

Snow mass balance

HS	snow depth [m]
S_{can}	water storage in the canopy system [mm SWE]
ΔS_{can}	interval change of water storage in the canopy system [mm SWE]
S_{snow}	water storage in the snowpack system [mm SWE]
ΔS_{snow}	interval change of water storage in the snowpack system [mm SWE]
$P\uparrow$	rate of above-canopy snowfall [mm hr $^{-1}$]
$P\downarrow$	rate of below-canopy snowfall [mm hr $^{-1}$]
I	rate of snow interception by the canopy [mm hr $^{-1}$]
F	rate of snow throughfall [mm hr $^{-1}$]
U	rate of unloading of intercepted snow from canopy to snowpack [mm hr $^{-1}$]
D	rate of liquid water drip from canopy to snowpack [mm hr $^{-1}$]
Q	rate of liquid water discharge from snowpack [mm hr $^{-1}$]
V	rate of sublimation of snow to the atmosphere [mm hr $^{-1}$]
V_{can}	rate of sublimation of intercepted snow from the canopy [mm hr $^{-1}$]
V_{snow}	rate of sublimation from snowpack [mm hr $^{-1}$]
W	rate of wind transport out of the snowpack system [mm hr $^{-1}$]

Statistical analysis

$\overline{x}$	Time average of variable x over a given time interval
μ	Mean of a set
σ	Standard deviation of a set
c_v	Coefficient of variation of a set
ρ_s	Spearman's rank correlation coefficient between to covariates
R^2	Coefficient of determination
R^2_{adj}	Coefficient of determination adjusted for degrees of freedom

Canopy transmittance

x	Easting in UTM zone 11N [m]
y	Northing in UTM zone 11N [m]
z	elevation [m AGS / m AMSL]
i	UTM zone 11N coordinate vector (x, y)
ϕ	zenith angle [° from zenith]
θ	azimuth angle [° clockwise from north from above looking down]
j	angle vector (ϕ, θ)
B	a theoretical beam of finite width and length passing through the canopy
b	a finite segment of a beam B
L_B	length of beam B [m]
v	a theoretical volume of the canopy
k_v	light attenuation coefficient [m^{-1}]
$f_v(\phi)$	mean contact frequency within volume v as a function of ϕ [m^{-1}]
χ_B	number of canopy contacts along beam B [-]
T_B	light transmittance of the canopy along beam B [-]
T_B^*	snow transmittance of the canopy along beam B [-]
ω	light contact absorption coefficient [-]
ω^*	snow particle contact absorption coefficient [-]
p_t	probability of light transmittance given a contact with the canopy [-]
p_a	probability of light absorption given a contact with the canopy [-]
p_t*	probability of snow transmittance given a contact with the canopy [-]
p_a^*	probability of snow interception given a contact with the canopy [-]
LAD	leaf area density (one-sided leaf area per unit volume) [m^{-1}]
LAI	leaf area index (one-sided leaf area above a unit area of ground) [-]
$G(\phi)$	extinction efficiency (ratio of leaf area to projected leaf area in ϕ direction)

Lidar snowpack estimates

HS_{lidar}	snow depth estimated from lidar observations [m]
ρ_f	snowpack density estimate for the forest plot [kg m^{-3}]
ρ_c	snowpack density estimate for the clearing plot [kg m^{-3}]
SWE_f	SWE estimated over the forest plot [mm]
SWE_c	SWE estimated over the clearing plot [mm]
ρ_{fresh}	snow density estimate of fresh snow immediately after snowfall [kg m^{-3}]
ρ_{new}	snow density estimate of the newest layer of snow at the time of survey [kg m^{-3}]
HS_{max}	maximum snow depth from acoustic sensor over a given time interval [m]
HS_{min}	minimum snow depth from acoustic sensor over a given time interval [m]
HS_{obs}	snow depth from acoustic sensor at the time of a given survey [m]
ΔSWE_f	change in SWE estimated over the forest plot
ΔSWE_c	change in SWE estimated over the clearing plot

Ray sampling of lidar

n	number of samples within a given volume [m^{-3}]
k	number of lidar returns within a given volume [m^{-3}]
L_s	ray sampling length [m]
L_r	ray resampling length [m]
L_{vox}	side length of a cubic voxel [m]
p_r	Bayesian probability of lidar return given a sample [-]
beta(α, β)	beta distribution with parameters α and β
α_{prior}, β_{prior}	Bayesian prior hyperparameters [-]
μ_{prior}, σ^2_{prior}	mean and variance of return rates estimated over the observed data [-]
α_{post}, β_{post}	Bayesian posterior hyperparameters [-]
$\langle \mu_B \rangle, \langle \sigma_B^2 \rangle$	estimated mean and uncertainty of modeled returns along beam B [-]
c_χ	contact number correction factor [contacts / return]

Canopy metrics

△	flag for voxel ray sampling metrics with snow-on canopy conditions
▲	flag for voxel ray sampling metrics with snow-off canopy conditions
•	flag for point cloud reprojection metrics with snow-off canopy conditions
CC	canopy closure [-]
LAI_{2000}	LAI calculated following Licor LAI-2000 device [-]
V_f	sky view factor [-]
CHM	canopy crown height model [m AGS]
DNT	horizontal distance to nearest tree [m]
DCE	horizontal rectilinear distance to canopy edge [m]
MCH	mean canopy height [m AGS]
fCov	fractional canopy cover [-]
MDC	mean distance to canopy [m]
TGA	total gap area [m^2]
$T^\dagger$	light transmittance estimated from thresholded hemispherical imagery [-]
$\chi^\dagger$	contact number estimated from thresholded hemispherical imagery [-]
LPM-L	laser penetration metric considering last returns [-]
g_F	count of first returns classified as ground within a given area [-]
g_L	count of last returns classified as ground within a given area [-]
c_F	count of first returns classified as canopy within a given area [-]

Rejection sampling

E	target distribution – normalized bias metric distribution over all pixels
O	sample distribution – normalized bias metric over observed pixels
r_b	sampling acceptance rate for bin *b* [-]
m	normalizing constant [-]

Snow accumulation modeling

I_{HP}	Rate of snow interception from Hedstrom and Pomeroy (1998)
F_{HP}	Rate of throughfall calculated from Hedstrom and Pomeroy (1998)
L_0	Antecedent canopy storage from Hedstrom and Pomeroy (1998)
S^*_{can}	Theoretical maximum intercepted snow load
S^0_{can}	Antecedent intercepted snow load from Hedstrom and Pomeroy (1998)
$\bar{S}$	Species dependent max snow load scalar from Hedstrom and Pomeroy (1998)
C_p	Maximum plan area of the canopy from Hedstrom and Pomeroy (1998)
J	downwind forested snow particle fetch from Hedstrom and Pomeroy (1998)
u	horizontal wind speed from from Hedstrom and Pomeroy (1998)
w	vertical snow particle fall speed from Hedstrom and Pomeroy (1998)
I_M	Rate of snow interception from Moeser, Stähli et al. (2015)
F_M	Rate of throughfall calculated from Moeser, Stähli et al. (2015)
F_j	Rate of throughfall calculated from Gaussian snowfall model

Chapter 1: Introduction

1.1 Motivation and relevance

Vegetation structure is one of the most important factors controlling the spatial and temporal variation of snow in forests at lengths from 1 m - 1000 m, with dominant length scales of variation typically observed within 40 m (Shook and Gray, 1997; Pomeroy et al., 2002; Deems et al., 2006; Trujillo et al., 2007; Clark et al., 2011; Zheng et al., 2015). This influence is attributed to the role of vegetation in altering snow accumulation, interception, and redistribution in combination with ablation processes (Musselman et al., 2008; Varhola et al., 2010). Spatial variation in snow accumulation shapes snow cover depletion curves in the melt season, driving ablation rates and contributing areas for snowmelt runoff (DeBeer and Pomeroy, 2010; Clark et al., 2011). Vegetation structure therefore influences both quality and timing of snowmelt runoff in forested basins with seasonal snowpack (Dickerson-Lange et al., 2017).

Changes in vegetation structure have been observed to drive significant changes in hydrology due to the coupling of canopy structure and snow accumulation processes (Varhola et al., 2010). Reduced snow interception and sublimation have been shown to drive increased accumulation following forest loss due to fire, pest, and clearcutting, accompanied by significant increases in ablation rates (Pomeroy and Goodison, 1997; Musselman et al., 2008; Pomeroy et al., 2012; Ellis et al., 2013; Harpold et al., 2014). These findings have led to efforts to alter forest structure by selective thinning to maximize snow melt runoff, with mixed results (Golding and Swanson, 1978; Troendle and Leaf, 1980; Harpold et al., 2020). Vegetation changes results in changes in local and downstream hydrology and influence water availability for ecosystems and human systems alike (Trujillo et al., 2012; Broxton et al., 2015). Land management, conservation and water resource decisions therefore stand to be informed by a robust understanding of snow-vegetation interactions, particularly in the contexts of global climate change, increased prevalence of forest loss from fire and pest, and ongoing forest loss due to deforestation and land use change (Volney and Fleming, 2000; Curtis et al., 2018; Johnston et al., 2020).

Efforts to explain and predict snow accumulation and interception in forests have yielded parameterizations of interception rates and canopy interception capacity as functions of a variety of canopy structure metrics (Schmidt and Gluns, 1991; Hedstrom and Pomeroy, 1998; Andreadis et al., 2009; Moeser, Stähli, et al., 2015; Roth and Nolin, 2019), but fundamental differences among models suggests that further validation is needed to determine advantages and limitations of model assumptions among diverse environments and conditions (Lundberg and Halldin, 2001; Rutter et al., 2009; Clark et al., 2011). A better understanding of the physical bases of snow accumulation processes in forests is important to advance snow hydrology in cold regions due consequences for quantity and timing of water availability in the melt season (Musselman et al., 2008; DeBeer and Pomeroy, 2017; Dickerson-Lange et al., 2017).

Technological developments in airborne lidar platforms have increased lidar availability and utility for forestry and snow hydrology applications in recent years (Wulder et al., 2012; Deems et al., 2013). Airborne lidar is a compelling tool for investigating snow accumulation in forests due in part to simultaneous acquisition of snow depth and canopy structure observations (Broxton et al., 2015; Mazzotti et al., 2019). Furthermore, lidar integration with uncrewed aerial vehicle (UAV) platforms contributes to increased access to airborne lidar methods and opportunities for increased survey frequency with reduced costs and logistics (Wallace et al., 2012; Harder et al., 2020). Combined with ground-based snow accumulation and canopy structure metrics, UAV-lidar has shown potential to help expand and unify existing understandings of snow accumulation in forests – across length scales from branches to basins, and across time scales from hours to seasons.

1.2 Research background

This section contains a review of the literature concerning conceptual understandings, measurement, and modeling of snow accumulation in forested environments. Terms are operationalized for use throughout this research, and a refined summary of relevant literature is presented to inform the research design.

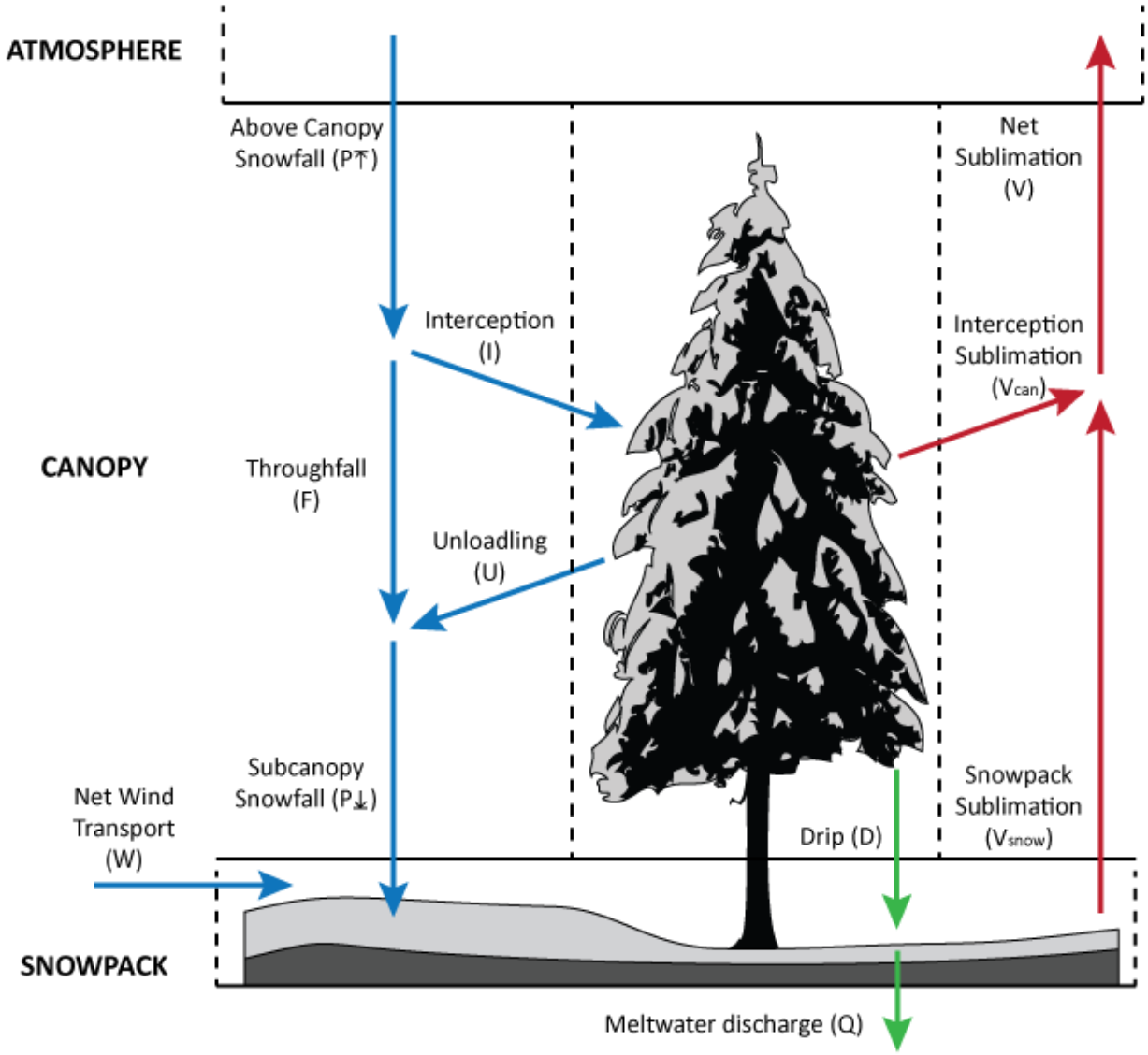

Figure 1.1: A conceptual diagram of water mass flux processes between the atmosphere, canopy, and snowpack systems. Labeled arrows correspond to each process and indicate the positive direction of flux in and out of each system (length is not representative of flux magnitudes). Arrows are colored by water phase: solid (blue), liquid (green), and vapour (red).

1.2.2 Snow accumulation in forests

Snow accumulation in forest environments can be considered as a mass exchange of water in various phases between the atmosphere, the forest canopy, and the snowpack on the ground (Figure 1.1). Storage of intercepted snow in the canopy (S_{can}, a.k.a. intercepted snow load) and of the seasonal snowpack (S_{snow}) represented in units of mm snow water equivalent (mm SWE) and depend on the cumulative sum of mass fluxes in and out of the respective systems from the beginning of the season. The rate of increase of intercepted snow load in the canopy system is expressed as:

$$\frac{dS_{can}}{dt} = \mathrm{N}_{\mathrm{can}} \qquad \text{Eq. 1.1}$$

where M_{can} is the total mass flux to the intercepted snow load. M_{can} can be broken into components corresponding to distinct mass flux processes following (Figure 1.1):

$$M_{\mathrm{can}} = P\uparrow - F - U - D - V_{can} \qquad \text{Eq. 1.2}$$

where $P\uparrow$ is the rate of above canopy snowfall, F is the rate of throughfall through the canopy, U is the rate of unloading of intercepted snow from the canopy, D is the rate of liquid water drip from intercepted snow, and V_{can} is the rate of sublimation of intercepted snow to the atmosphere. Change in intercepted snow storage over a time interval from t_0 to t_1 is expressed by the time integral:

$$\Delta S_{can} = \int_{t_0}^{t_1} M_{can}(t)\, dt \qquad \text{Eq. 1.3}$$

or similarly as:

$$\Delta S_{can} = \overline{M_{can}}\, \Delta t \qquad \text{Eq. 1.4}$$

where $\overline{M_{can}}$ is the mean mass flux to the intercepted snow load over the time interval and $\Delta t = t_1 - t_0$. Similarly, the rate of increase of storage in the snowpack is expressed as:

$$\frac{dS_{snow}}{dt} = M_{snow} \qquad \text{Eq. 1.5}$$

where M_{snow} is the total mass flux to the snowpack. M_{snow} can be broken into components corresponding to distinct mass flux processes following (Figure 1.1):

$$M_{snow} = P\uparrow - I + U + D + W - Q - V_{snow} \qquad \text{Eq. 1.6}$$

where W is the rate of wind transport of snow into the snowpack, Q is the rate of liquid water discharge from the snowpack, and V_{snow} is the rate of snowpack sublimation to the atmosphere. Change in storage of the snowpack over a time interval from t_0 to t_1 is expressed by the time integral:

$$\Delta S_{snow} = \int_{t_0}^{t_1} M_{snow}(t)\, dt \qquad \text{Eq. 1.7}$$

or similarly as:

$$\Delta S_{snow} = \overline{M_{snow}}\, \Delta t \qquad \text{Eq. 1.8}$$

where $\overline{M_{snow}}$ is the mean mass flux to the snowpack over the time interval.

Snowfall that passes through the canopy without interception is called "throughfall". The rate of throughfall (*F*) is sometimes expressed in terms of rates of above-canopy snowfall and interception and presumes active snowfall – that is, throughfall can only occur during snowfall:

$$F = P\uparrow - I \qquad \text{Eq. 1.9}$$

Similarly, snowfall observed at the bottom of the canopy ($P\downarrow$, a.k.a. subcanopy snowfall) is the combination of throughfall and unloading:

$$P\downarrow = F + U \qquad \text{Eq. 1.10}$$

and, like unloading, can be observed outside time intervals of active snowfall.

1.2.3 Measuring forest snow accumulation

Processes and rates of snow accumulation in forests differ from those in environments with low or sparse vegetation due primarily to the role of forest canopies in intercepting snow (Lundberg and Halldin, 2001; Friesen et al., 2015). Evergreen needleleaf canopies have been estimated to intercept as much as 60% of annual snowfall in midwinter (Hedstrom and Pomeroy, 1998). Intercepted snow is then preferentially sublimated compared with snow on the ground due to greater surface area and greater exposure to turbulent airflows (Pomeroy and Schmidt, 1993; Parviainen and Pomeroy, 2000; Molotch et al., 2007). As much as 40% of annual snowfall has been estimated to be sublimated in some forested environments, while the remaining intercepted snow is redistributed to the surface via unloading or melting and dripping (Pomeroy et al., 1998). A fundamental understanding of snow accumulation in forests therefore requires consideration of the role of snow interception in altering accumulation processes and rates.

While similar methods are typically used for measuring snow accumulation between open and forested areas, forest measurements present several additional challenges over measurements in unvegetated areas. Generally greater spatial variance in snowpack depth and SWE observed over shorter length scales around vegetation results in greater error of areal estimates compared with open observations, for the same number of samples (Shook and Gray, 1997). While some methods such as snow surveys can compensate for increased uncertainty with increased sampling, methods which rely on placement of a single sensor (e.g., precipitation and snow depth gauges) are less flexible and may result in systematic bias if sensor placement is not representative of the area of interest (Grünewald and Lehning, 2015; Lv and Pomeroy, 2020). Additionally, significant covariances of snow depth and SWE with vegetation density (Sturm, 1992) can coincide with sample bias away from dense vegetation for manual surveys, sensors, and even airborne lidar observations, resulting in systematic bias of areal estimates derived from such observations (Harding et al., 2001; Béland et al., 2019). Furthermore, direct measurement of above canopy precipitation ($P\bar{f}$), snow interception (ΔSWE_{can}), and sublimation of intercepted snow (V_i) is often challenging to do beyond the scale of individual branches or trees due to difficulty accessing the upper canopy. As a result, specific methodologies have been developed to measure and estimate snow accumulation within forests (Lundberg and Halldin, 2001).

Weighted measurement of intercepted snow mass has been implemented from the branch scale (Schmidt and Gluns, 1991) up through that of individual trees (Satterlund and Haupt, 1967; Hedstrom and Pomeroy, 1998; Storck, 2000) by various lysimeter designs, corrected for the mass of vegetation by taking the difference in mass between snow-on and snow-off canopy conditions. To calculate SWE in terms of ground surface area, intercepted snow mass is sometimes normalized by the projected surface area of the branch or tree (Satterlund and Haupt, 1967; Schmidt and Gluns, 1991). Morphological metrics of intercepted snow clumps such as surface area, volume, and fractal dimension have also been used to quantify storage at the branch scale (Pomeroy and Schmidt, 1993), though are less common in the literature.

Research into forest snow accumulation and interception processes conducted at the scale of individual branches has provided a foundational understanding of the physical processes relating snow interception to canopy structure. Satterlund and Haupt (1967) observed intercepted snow on needleleaf saplings in which there were low interception rates for snow-free branches that increased as snow accumulated, but which was ultimately limited to a finite interception storage. They inferred a sigmoidal relationship between storm precipitation and canopy storage. Schmidt and Gluns (1991) observed a similar sigmoidal interception response from individual branches for several different species. In contrast to Satterlund and Haupt (1967), however, Schmidt and Gluns (1991) found that meteorological conditions explained more of the observed variation in interception than tree species.

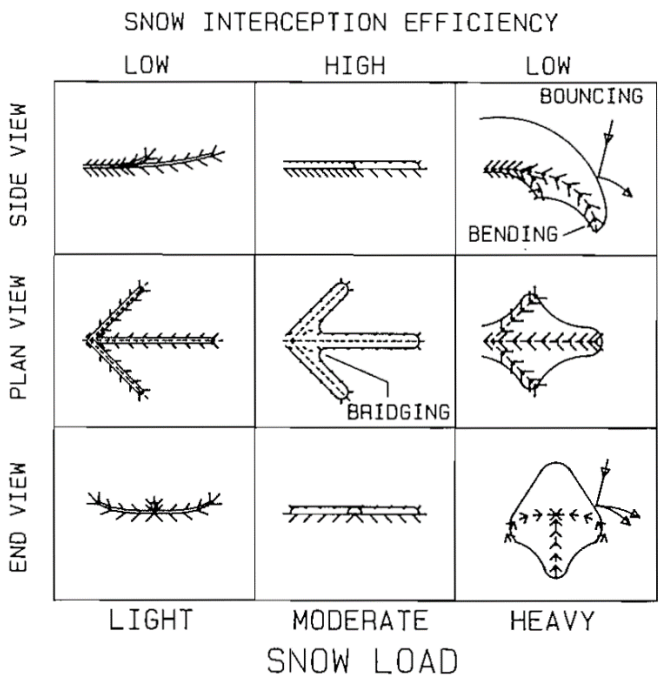

Figure 1.2 – Reproduced from Schmidt and Gluns (1991): A schematic illustrating the physical processes of bouncing (rebounding), bending (branch compression), and snow bridging at the branch scale from various perspectives, and under three snow loads

Efforts have been made to identify physical processes governing interception and unloading of snow by forest canopies (Pomeroy and Gray, 1995). Bridging of intercepted snow across small gaps in needles and branches (Figure 1.2) has been identified as a mechanism for positive feedback in interception, to which the initial increase in the sigmoidal relationship has been attributed (Schmidt and Gluns, 1991). The shape of intercepted snow clumps has been observed to be exhibit fractal properties, providing opportunities for relating projected circumference, projected surface area, and volume of snow clumps to aid in scaling assumptions and sublimation estimates (Pomeroy and Schmidt, 1993; Pomeroy, Gray, et al., 1998). Fractal dimensions of intercepted snow clumps were found to be insensitive to both perspective and

branch size, although a significant difference in fractal dimension and load was found between the bottom and top of the canopy. Previous research by Schmidt and Pomeroy, 1990 demonstrated the role of branch bending due to increased intercepted load (Figure 1.2) as a process which limits interception storage at the branch scale and identified temperature dependencies of branch elasticity as a mechanism for rapid unloading of intercepted snow in warming conditions.

Research into the collision dynamics of falling snow particles with branches and intercepted snow has been conducted in an effort to understand small-scale controls of interception processes (see Miller 1964 for a partial review). Extensive work by Kobayashi (1987) and later Pfister and Schneebeli (1999) examined the adhesion, cohesion, and rebound of falling snow particles on boards of varying widths, finding temperature dependence of interception rates and storage in connection with a reduction in collision elasticity above -3 °C. This work also observed an increase in interception efficiency (i.e., interception per unit branch area) with increased board width, a possible mechanism for the initial increase in interception efficiency at low snow loads due to bridging of snow as noted by Satterlund and Haupt (1967).

Few studies have demonstrated methods for measuring intercepted snow at the scale of forest stands. Calder (1990) implemented near-field remote sensing of intercepted snow by active gamma radiation attenuation sampling across a forest stand under varying intercepted loads. This required the suspension of a power radioactive source on a forest tower and the raising and lowering of this source through the canopy by remote control. By this method Calder observed an exponentially limiting relationship between cumulative snowfall and intercepted snow at the canopy scale. While these findings are valuable for informing a stand-scale understanding of snow interception processes (Lundberg et al., 1998), the reliance on a powerful radioactive source presents modern logistical hurdles and known health risks, limiting the accessibility of this method.

Satellite remote sensing provides many tools for snowpack and vegetation measurement, but none have yet been shown to serve well as a standalone method for quantifying intercepted snow in forest canopies. Passive visible and infrared satellite imagery is used to map snow covered area at relatively high spatial resolutions in open areas, but these methods face challenges in vegetated areas where albedos can vary greatly with slope, species, canopy structure, solar elevation angle, and the presence of intercepted snow (Frei et al., 2012; Hovi et al., 2016; Webster and Jonas, 2018). Lv and Pomeroy (2019) demonstrated the potential to detect the presence of intercepted snow in forest canopies using visible and infrared Landsat imagery, but further work is needed to develop such tools to quantify intercepted snow mass. While passive microwave remote sensing by satellite has been used to estimate snowpack SWE and rainfall interception remotely, it too faces challenges in the presence of vegetation (Sellers et al., 1997; Miralles et al., 2010). In addition to low spatial resolution, passive microwave and gamma

sensing of SWE in forests are complicated by radiation emission from exposed vegetation, and the segmentation of attenuation components from snowpack and intercepted snow is nontrivial (Frei et al., 2012).

1.2.4 Modeling forest snow accumulation

In the absence of accessible methods for direct observation of intercepted snow at the stand scale, methods have been developed to quantify interception rates and canopy storage indirectly. Snow mass budgeting estimates the change in intercepted snow storage by the residual of above-canopy snowfall and subcanopy SWE (Friesen et al., 2015):

$$\Delta S_{\mathrm{can}} = \overline{\mathrm{P}\,\overset{\uparrow}{\uparrow}}\,\Delta \mathrm{t} - \Delta S_{snow} \qquad \text{Eq. 1.11}$$

where $\overline{\mathrm{P}\,\overset{\uparrow}{\uparrow}}$ is the mean rate of above canopy snowfall over the given time interval. While estimates of subcanopy snowfall within a forest can be made from a variety of methods including snow surveys and precipitation gauges, cumulative above-canopy precipitation is often challenging to measure directly in absence of above-canopy precipitation gauges. A common practice is to estimate above-canopy precipitation by ΔSWE observations within a nearby clearing (e.g., Pomeroy et al., 2002). When using observations of ΔSWE, differences in energy fluxes between forested and open sites can result in biased snowpack observations if significant ablation of snow on the ground has occurred between observation timesteps (Musselman et al., 2008). Furthermore, as wind redistribution from open to forested areas can be difficult to distinguish from precipitation or throughfall, conditions or locations are often selected such that redistribution can be considered negligible (Pomeroy and Gray, 1995). The snow mass budgeting method is therefore simplified by observations close in time to snowfall events, cold environmental conditions which limit energy available for ablation, and locations where the redistribution of snow by wind can be considered negligible (Pomeroy et al., 2002; Lundberg and Koivusalo, 2003; Moeser, Stähli, et al., 2015). Additionally, due to large spatial variation of snow depth and density both below the canopy (Sturm, 1992; Deems and Painter, 2006) and in canopy gaps or clearings (Golding and Swanson, 1978; Grünewald and Lehning, 2015), care must be taken to ensure that accumulation or precipitation observations are not biased by factors such as forest edge effects or sample bias away from dense vegetation. When considering total accumulation over a snowfall event, it is difficult to distinguish between field observations of "true" throughfall (i.e., snow that does not encounter the canopy) from that which is intercepted and subsequently unloaded between observations. Using this method therefore requires careful navigation of model assumptions and sampling methods to minimize errors which are subsequently propagated into interception rate and canopy storage estimates (Lundberg et al., 1998; Friesen et al., 2015).

Clever navigation of these assumptions, however, has supported the development of several snow interception models which provide quantitative estimations of snow interception and

throughfall rates. Hedstrom and Pomeroy (1998) developed a physically motivated interception model, referred to as the "Hedstrom-Pomeroy model," which was validated by the snow budgeting method and upscaled tree lysimeter observations. The model is exponentially limiting (Figure 1.3) consistent with the findings of Calder (1990). The Hedstrom-Pomeroy model takes into consideration canopy structure parameters such as fresh snow density, leaf area index (LAI) and canopy closure (CC) and considers post-snowfall unloading under cold weather conditions. Further work was done to incorporate the sublimation (Pomeroy et al., 1998) and warm weather unloading and drip (Ellis et al., 2010) of intercepted snow into the Hedstrom and Pomeroy (1998) model, allowing for the representation of canopy storage hysteresis and the estimation of interception storage and accumulation over many storm cycles, and further validation of the improved model supported the relationship between LAI and stand-scale accumulation suggested by Hedstrom and Pomeroy (1998).

Snow accumulation observations in Norwegian pine forests in Switzerland were found to show stronger agreement with the sigmoidal model put forth by Satterlund and Haupt (1967), prompting efforts to incorporate elements of canopy structure into a model of this form (Moeser, Morsdorf, et al., 2015). By comparing snow budgeting interception storage estimates from meticulous snow surveys with a wide range of LiDAR-derived canopy structure metrics, Moeser, Stähli, et al. (2015) identified three canopy structure metrics sharing high covariances with maximum intercepted snow load, and low covariances with one another: mean distance to canopy (MDC), canopy closure (CC), and total gap area (TGA). A quadratic regression of the natural logarithm of these three metrics was then used to estimate the maximum interception efficiency of the sigmoidal interception model (Moeser, Stähli, et al., 2015), referred to hereafter as the "Moeser et al. model." The regression coefficients in the Moeser et al. model were optimized from snowfall events with no previous snow in the canopy, and with minimal wind redistribution (Moeser, Morsdorf, et al., 2015). Among sevral differences, the Moeser et al. and Hedstrom-Pomeroy models differ in their assumption of the relationship between interception efficiency and event precipitation, highlighted in Figure 1.3.

Several additional interception models have been developed over the years which differ notably from the Hedstrom and Pomeroy and Satterlund and Haupt models. Harestad and Bunnell (1981) developed an empirical formula incorporating a constant interception efficiency (I/P) for accumulated SWE at maximum seasonal snowpack with canopy closure based primarily on observations from the western United States. Storck (2000) developed an interception model for maritime snowpacks and forests with a piecewise temperature relationship and dependence on LAI, which was later validated by Andreadis et al. (2009). The combinations of Storck's model for warm weather conditions with the Hedstrom-Pomeroy model for cold weather conditions has resulted in additional interception models (Essery *et al.*, 2003; Gelfan *et al.*, 2004). Roth and Nolin (2019) proposed a model which incorporated metrics of median gap length at different elevations within the canopy into an interception model to represent variation snow interception

with vertical canopy structure in a maritime climate. Still other snow interception models exist beyond those mentioned here.

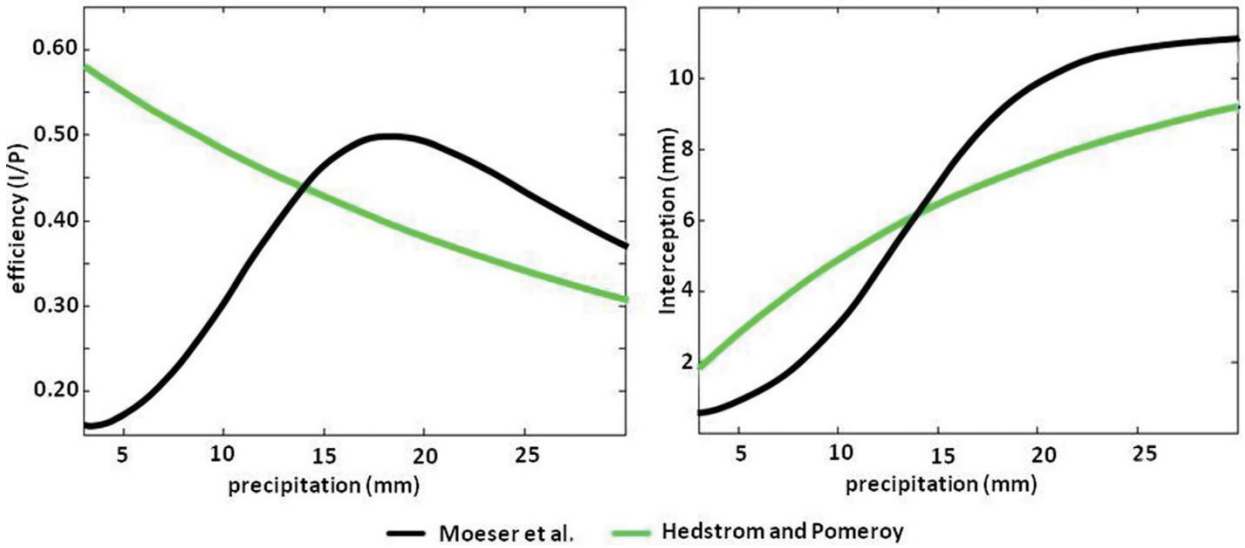

Figure 1.3 – Reproduced from Moeser, Stähli, et al. (2015): An example of two contradictory families of interception models found in the literature: the Moeser et al. sigmoidal model (black) first suggested by Satterlund and Haupt (1967), and the Hedstrom-Pomeroy exponential model (green).

Discrepancies between snow interception models persist despite extensive field validation of each model, and with few indications of which model assumptions are most appropriate for a given application in unvalidated canopies and conditions (e.g., Huerta et al., 2019). Differences in model validation environments such as air temperature, humidity, wind regime, and precipitation amount, as well as site variables such as species composition, crown height, and sun exposure may be a source of discrepancy, although some models have been validated with observations from multiple sites and climates (e.g., Ellis et al., 2010; Roth and Nolin, 2019). While some studies have directly compared model performances for select sites and climates (Huerta et al., 2019; Roth and Nolin, 2019), a hydrological fourth paradigm "characterized by the rigorous application of large datasets towards testing hypotheses" (Peters-Lidard et al., 2017) is arguably not yet accessible for snow interception models due primarily to a lack of large datasets of snow interception observations. It follows therefore that an important step toward the fourth paradigm is the development of standardized and accessible methods for measuring model inputs and outputs such as current and maximum intercepted snow loads, and above- and below-canopy precipitation at the modeled scales of forest stands and hydrological basins. Furthermore, rigorous hypothesis testing would benefit from observations of branch-scale physical processes such as branch bending and snow bridging between leaves which control stand-scale interception rates, and which are often implicitly encoded in models but are challenging to validate across forest stands (Lundberg and Halldin, 2001).

Snow interception has been shown to alter the structure of forest canopies. The bridging of snow across canopy gaps (Pomeroy and Schmidt, 1993; Satterlund and Haupt, 1967) and the bending

of branches due to increased intercepted load (Schmidt and Pomeroy, 1990) are two processes whereby intercepted snow can alter canopy structure with implications for subsequent interception rates. While rarely explicitly represented, such feedback mechanisms provide the physical justification for the asymptotic behavior of interception curves seen in Figure 1.3 (Hedstrom and Pomeroy, 1998). Despite such implicit considerations of interception – canopy structure feedbacks, however, most models parameterize canopy structure by metrics derived from snow-off canopy conditions. A better understanding of snow interception feedbacks could be informed by observations of canopy structure in the presence of different intercepted loads and would inform model suitability and further development.

1.2.5 Characterizing vegetation structure for explaining snow accumulation processes

While there is agreement in the literature on the importance of vegetation structure for snow accumulation processes in and around forests, there is great diversity among methods used to characterize vegetation structure for parameterizing throughfall, redistribution and interception (Varhola et al., 2010). Accessibility of methods changes over time depending on cost, scale, logistics, and application, and which continue to evolve with technological developments. To simplify comparisons among disparate methods, canopy metrics are often established as quantitative benchmarks which are generally based on physical principals (Varhola and Coops, 2013; Moeser, Morsdorf, et al., 2015). For example, leaf area index (LAI) is a canopy metric defined as the one-sided leaf area per unit horizontal ground surface area (Chen and Black, 1991) which is frequently used in hydrological modeling, among other fields. Common methods to estimate LAI include direct leaf measurement by leaf litter collection for deciduous trees or destructive sampling (e.g., Chen et al., 1997), passive optical measurement by terrestrial photography (e.g., Thimonier et al., 2010), satellite imagery (e.g., Zhao and Popescu, 2009) or other optical devices (e.g., Li-Cor, 1992), and lidar measurement by terrestrial (e.g., Grotti et al., 2020), airborne (e.g., Alonzo et al., 2015) or spaceborne laser scanners (Béland et al., 2019; Yan et al., 2019). Canopy crown height (CHM), fractional cover (fCov), sky view factor (V_f) and hemispherical canopy closure (CC) are several additional examples from the wide body of canopy metrics described in the literature and commonly applied to snow accumulation and ablation processes (e.g., Hedstrom and Pomeroy, 1998; Varhola and Coops, 2013; Mazzotti et al., 2019; Helbig et al., 2020).

The body of canopy metrics found in the literature and used to parameterize snow-vegetation interactions has seen substantial growth in recent years due to advances and increased accessibility of lidar methods. With this growth have come opportunities for assessing and selecting for canopy metrics which are most appropriate for parameterizing a given hydrological process. The suitability of a given metric parameterization of a hydrologic process can be evaluated along several bases including predictive performance, physical realism, and accessibility due to data and computational requirements (Clark et al., 2017). These efforts are ongoing in the context of snow accumulation processes. For example, Hedstrom and Pomeroy

(1998) used a combination of representative LAI, CC, crown height, and downwind forested fetch estimates in combination with environmental variables of wind speed, air temperature, and antecedent intercepted load to parameterize interception and unloading rates based on a conceptual model of forest structure. While the conceptual model of the Hedstrom-Pomeroy model provides a clear framework of assumptions and implications for physical processes, the suitability of the input metrics for explaining tree-scale variance in snow interception and subcanopy accumulation has been called into question (Moeser et al., 2016). Moeser, Morsdorf, et al. (2015) conducted an extensive analysis of common and novel canopy metrics derived from airborne lidar for prediction of snow interception over low-wind accumulation events, identifying three metrics which were both strongly correlated with snow interception and shared low correlation with one another: canopy closure (CC), mean distance to canopy (MDC), and total gap area (TGA). Log transforms of these metrics were subsequently combined through an empirical quadratic equation with independent variables to estimate maximum interception capacity for field sites in the Swiss alps (Moeser, Stähli, et al., 2015). This model showed improved performance at the scale of meters over the Hedstrom-Pomeroy model for the validating observations. However, the physical bases and implications of the empirical metric parameterizations in the Moeser, Stähli, et al. (2015) model remain unclear for unvalidated forests and environments (Huerta et al., 2019). Mazzotti et al. (2019) demonstrated the utility of a novel set of metrics – collectively related to distance to canopy edge (DCE) – for characterizing directional and nondirectional canopy structure for modeling snow depth around vegetation and demonstrated the relatively small data and computational requirements for these metrics. Roth and Nolin (2019) parameterized maritime snow interception by median gap length and canopy crown height using an empirical power law relationship. The development of such metric parametrizations is motivated by discrepancies between existing models and observations, and more work remains to understand the physical bases relating such canopy metrics and the snow-vegetation interactions that they are used to parameterize, to extend their applications to unvalidated forests and environments.

Ray tracing of lidar for canopy characterization represents a growing field of research concerned with attempting to reconstruct a 3-D model of light or canopy structure properties of a portion of a canopy from lidar observations (Yan et al., 2019). Ray tracing of lidar has been used to estimate LAI, gap fraction, canopy openness (Béland et al., 2014; Hancock et al., 2017; Grotti et al., 2020; Westling et al., 2020), and leaf angle distribution, and light extinction coefficient (Ma et al., 2017). This technique takes advantage of multiple perspectives of the vegetation of interest from the lidar sensor, and is particularly promising for reducing the sensitivity of canopy metric estimates to non-uniform lidar sampling due to irregular scanning or attenuation of the lidar beam through dense vegetation (Béland et al., 2019). The utility of lidar ray tracing methods for characterizing vegetation structure for snow accumulation parameterizations is uncertain, and we found no previous research in this area.

1.2.6 Canopy light transmittance

Among the body of methods proposed for estimating canopy metrics, those based on optical measurements (including photography, lidar, and other optical sensors) have seen increased accessibility and use over the past few decades resulting from further technological developments, reduced cost of sensors and platforms, and increased accessibility (Yan et al., 2019). While optically derived metrics are quite varied across the literature, many rely on a similar framework and set of assumptions concerning canopy structure and canopy-light interaction, outlined below.

Consider a beam B of finite width which follows the ray with of angle ϕ from vertical and θ clockwise from north (from above, looking down), which intersects the ground surface at coordinates (x, y). For notation simplicity, $B(\phi, \theta, x, y,) = B(i, j)$ where $i = (\phi_i, \theta_i)$ represents the angle and $j = (x_j, y_j)$ represents the location of the ground intercept. The fractional light transmittance T_b of a segment b of beam B which transects a volume of canopy v is modeled following the Beer-Lambert law (Ross, 1981):

$$\mathrm{T_b} = \mathrm{e}^{-\mathrm{k_v}(\phi)\mathrm{L_b}} \qquad \text{Eq. 1.12}$$

where $k_v(\phi)$ [m^{-1}] is the attenuation rate as a function of beam angle from vertical ϕ, and L_b is the length of the transect [m]. This assumes 1) a homogenous canopy throughout volume v with 2) circularly symmetric anisotropy around the vertical axis and 3) small leaves relative to the cross-sectional area of the beam. T_b is sometimes referred to in literature as "gap fraction." Contact number $\chi_b(\phi)$ [-] which describes the number of times a ray along beam b contacts the canopy in length L_b can be expressed:

$$\chi_\mathrm{b}(\phi) = \mathrm{f_v}(\phi)\,\mathrm{L_b} \qquad \text{Eq. 1.13}$$

where $f_v(\phi)$ [m^{-1}] is the mean contact frequency per unit length within the volume. Note that contact number and contact frequency are sometimes alternatively defined in the literature in terms of the relative canopy thickness by including a $\cos(\phi)$ factor (e.g., Schleppi et al., 2007). The light contact absorption coefficient ω can be found by:

$$\omega = \frac{\mathrm{k_v}(\phi)}{\mathrm{f_v}(\phi)} \qquad \text{Eq. 1.14}$$

representing the mean e-folding of radiation intensity per canopy contact, assumed here to be independent of ϕ and constant across the canopy. Substituting Eq. 1.13 and Eq. 1.14 into Eq. 1.12 yields the following expression for fractional light transmittance:

$$\mathrm{T_b} = \mathrm{e}^{-\omega\chi_\mathrm{b}(\phi)} \qquad \text{Eq. 1.15}$$

Note that this is equivalent to the probabilistic case:

$$\mathrm{T_b} = \mathrm{p_t}^{\chi_b(\phi)} \qquad \text{Eq. 1.16}$$

where $p_t = e^{-\omega}$ is the transmittance probability given a single contact and is related to the absorption probability $p_a = 1 - p_t$.

Canopy density can be expressed in terms of leaf area density LAD_v [m^{-1}], defined as the one-sided leaf area per unit volume (Béland et al., 2014):

$$\chi_b(\phi) = G(\phi) LAD_v \mathrm{L_b} \qquad \text{Eq. 1.17}$$

where $G(\phi)$ is the ratio of the projected leaf area in the ϕ direction to one-sided leaf area according to an assumed leaf angle distribution (Ross, 1981). As this research concerns the physical structure of the entire canopy and not just the photosynthetically active parts, all vegetation surfaces (i.e., leaves, branches, trunks, intercepted snow) are included in this definition of *LAD*. Solving for LAD_v in terms of an observed transmittance T_b yields:

$$LAD_v = \frac{-\ln(T_b)}{\omega G(\phi) L_b} \qquad \text{Eq. 1.18}$$

Light transmittance along a beam *B* which traverses multiple volumes $\{v_i \mid i = (1, 2 \ldots n)\}$ can be expressed as a product of transmittances along each segment b_i transecting volume v_i, or equivalently as the transmittance through the sum of canopy contacts along *B*:

$$\begin{aligned} \mathrm{T_B} &= \prod_b \mathrm{T_b} \\ &= \prod_b \mathrm{e}^{-\omega\chi_b(\phi)} \\ &= \mathrm{e}^{-\omega\chi_B(\phi)} \end{aligned} \qquad \text{Eq. 1.19}$$

where $\chi_B(\phi) = \sum_b \chi_b(\phi)$ is the total contact number along beam *B*.

Leaf area index *LAI*, defined as the one-sided leaf area per unit ground area, can be calculated explicitly along an arbitrary beam *B* as the vertical component of the integral of *LAD* along *B*:

$$\begin{aligned} LAI &= \int_B LAD\, dz \\ &= \int_B LAD\, cos(\phi) dL \end{aligned} \qquad \text{Eq. 1.20}$$

and which can be expressed in terms of discrete segments *b* of beam *B* by:

$$LAI = cos(\phi) \sum_{b} \frac{\chi_b(\phi)}{G(\phi) L_b} \qquad \text{Eq. 1.21}$$

LAI derived from transmittance observations is sometimes referred to in literature as "*effective LAI"*, to differentiate from *LAI* derived from direct measurement of leaf areas (J.M. Chen and Black, 1991). Substantial differences between *LAI* and *effective LAI* result from violations of the assumptions used for estimating effective LAI from light transmittance, including branch clumping, influence of stems and trunks, and the orientation of scattering elements (Pomeroy and Dion, 1996).

1.3 Research gaps

While horizontal length scales of variation in forest snowpacks are typically limited to within 40 m, scaling of snow accumulation processes within this range remains a persistent research problem (Clark et al., 2011). Processes which determine the resting place of an individual snowflake falling into a forest exhibit complex behaviour, with sensitive dependence on initial conditions including snow crystal and vegetation structure, fall velocity, collision angle, and temperature which all influence particle adhesion, cohesion, and rebound probabilities (Kobayashi, 1987; Pfister and Schneebeli, 1999). The interactions of these physical processes result in emergent behaviors at the branch scale including bridging of snow across gaps between needles (Schmidt and Gluns, 1991) and bending of branches under intercepted loads (Schmidt and Pomeroy, 1990). Efforts to explicitly represent particle collision parameters or branch-scale emergent behaviors to scales of forest stands and precipitation events are quickly overwhelmed by prohibitive data requirements and uncertainty, however (Varhola et al., 2010). Instead, snow-vegetation interactions are more-conveniently considered in terms of stand- and event-scale emergent behaviours, such as stand-scale interception and unloading rates, maximum and antecedent intercepted loads, and mean event wind speeds and directions (Hedstrom and Pomeroy, 1998; Moeser, Stähli, et al., 2015). Furthermore, vegetation structure is often conveniently described in term of stand-scale characteristics such as species composition and stem density, while changes in vegetation structure are commonly described by broad mechanisms such as logging, thinning, fire, and disease (Varhola et al., 2010; Pomeroy et al., 2012). While stand-scale parameters and emergent behaviours are essential for a practical understanding of the effects of climate change and forest disturbance on stand- and basin-scale hydrology, models which parameterize them are only as robust as the understanding of their relationships from the fundamental system components of snowflakes and branches. A better understanding of the physical bases of emergent behaviors of snow accumulation in forests is needed to robustly parameterize them and assess their sensitivities to systematic changes.

Subcanopy upward-facing hemispherical photography analysis ("hemispherical analysis") is a body of methods for estimating canopy structure and light transmittance properties in forests from angular variation in ambient light transmittance of the canopy across the hemispherical field of view (J. B. Miller, 1967; Ross, 1981). At its core, hemispherical analysis relies on binary ("thresholded") canopy transmittance inputs which require aggregation across a representative angular region to arrive at non-binary descriptive metrics. This methodology facilitates the estimation of many canopy metrics from photography, including transmittance, contact number, leaf angle distribution, and effective leaf area index (LAI). The convenience of data collection and analysis for hemispherical analysis has improved greatly with the development of specific sensors for in-situ metric estimates (e.g., Li-Cor, 1992), software for analysis of digital hemispherical photos (e.g., Caneye, DHP, Hemisfer, HPEval), and methods for the synthetic generation of hemispherical photos from lidar point clouds (Varhola and Coops, 2013; Moeser et al., 2014; Webster et al., 2020). The diversity of metrics and relative convenience of these methods for characterizing canopy structure presents the opportunity to assess which metrics are most appropriate for parameterizations of specific snow-vegetation interactions. Additionally, methodological developments have supported more nuance in the assumptions used to characterize canopy structure from variations in binary transmittances (e.g., Chen and Cihlar, 1995; Schleppi et al., 2007; Thimonier et al., 2010). Despite these advances, central assumptions such as a representative angular region (Miller, 1967), spatially random leaf distributions (Nilson, 1971) and spatially uniform photographic sampling (Thimonier et al., 2010) or lidar sampling (Grotti et al., 2020) continue to limit the application of these methods to higher spatial resolutions. As the development of these and other methods continues, there is further opportunity to reassess these assumptions for more-refined analyses.

Sampling bias is inherent to airborne lidar measurements of subcanopy surfaces due to inhomogeneous occlusion of the ground from the lidar sensor by variable-density vegetation. The result is reduced surface sample densities below higher-density vegetation compared with in vegetation gaps (Broxton et al., 2015) which can vary from negligible to consequential depending on several factors including: the size of the lidar beam footprint relative to vegetation elements, beam intensity and sensor sensitivity, areal sample density, post-processing methodology, and the questions being asked of the data (Béland et al., 2019). Sample bias away from dense vegetation is particularly problematic when the subcanopy surface is related to canopy vegetation. This is commonly the case with snow surfaces, where shallow snowpack typically found below dense vegetation correspond to lower lidar point densities. Generating surface models from these data results in larger interpolation lengths and associated errors below dense vegetation, and significant bias can be introduced by interpolating over regions of dense vegetation using observation from surrounding gaps in vegetation (Harder et al., 2020). One solution is to limit interpolation lengths to less than half of the snowpack length scales of variation of interest (Nyquist, 1928). While this prevents large data gaps of dense vegetation from being masked with unrepresentative interpolations, it may nonetheless result in estimates

that are skewed toward the higher surface point densities found in canopy gaps. Of additional concern, ground validation may also be biased away from dense vegetation. Careful consideration must be taken therefore to ensure that estimations of areal snow depths statistics are representative, not biased toward lower vegetation densities. There is a need for further methods to assess and correct vegetation sample bias in areal estimates of snow depth from airborne lidar.

Similarly, lidar vegetation return densities in forests and other vegetated environments are inherently nonuniform due to occlusion of the lidar beam by vegetation, with disproportionately high return densities from foreground vegetation relative to the sensor compared with those beyond (Harding et al., 2001; Chasmer et al., 2006; Webster, 2017; Grotti et al., 2020). This effect becomes more pronounced with small-footprint lidar (relative to the size of the vegetation elements), where a beam may be entirely occluded by a single branch or trunk (Béland et al., 2019). Many methods for quantifying vegetation density and subcanopy snow depths from lidar rely on the assumption of sample uniformity, however. The validity of this assumption should be assessed on a case-by-case basis, and alternative methods should be developed and implemented for cases when this assumption is not justified.

Laser penetration metrics (LPMs) are a class of methods used to estimate vegetation density in terms of lidar beam occlusion (Hopkinson et al., 2005; Zhao and Popescu, 2009; Musselman et al., 2015). While LPMs are normalized by sample density and are therefore insensitive to nonuniform sampling, their analyses are limited to explicit lidar beam trajectories. For parallel beam samples (e.g., ALS) this often necessitates assumptions of angular dependence of beam attenuation to generalize laser penetration to unsampled angles (e.g., Alonzo et al., 2015). Even for sampling methods which allow for scanning of targets from a wider set of angles and perspectives (e.g., TLS and UAV-lidar), sampling becomes sparse and irregular when analyzed over several spatial and angular dimensions and necessitates similar assumptions to generalize in space and across angles (Liu et al., 2018). There is a need for methods which allow for the combination of laser penetration observations and generalizing assumptions to develop generalized spatial models of vegetation that are robust to non-uniform and non exhaustive sampling.

Voxel ray tracing of lidar is a developing set of methods which provides a general solution for building vegetation density models from inhomogeneous lidar sampling (Béland et al., 2014; Hancock et al., 2017; Grotti et al., 2020). Specifically, these methods can be used to provide estimates of contact number and transmittance along arbitrary, unobserved rays over much smaller angular footprints than are needed for hemispherical analysis. These methods are limited by the need for extensive validation to interpret lidar sensor observations in terms of physical canopy properties. There have been few applications of these methods to forest-scale plots, and

none to our knowledge which have been applied to understanding relationships between vegetation and snow.

1.4 Research design

In summary, spatial variation of snow accumulation occurs down to the scale of individual branches, with hydrologic ramifications at the stand and basin scales. Direct measurement of accumulation and interception rates is challenging to conduct at length scales greater than those of individual trees, however. Many models have been developed to estimate snow accumulation processes at the scale of forest stands, but discrepancies between models are prevalent and a lack of standardized observations for robust hypothesis testing across canopy and environmental variables is lacking. A refined understanding of the physical processes of branch-scale snow accumulation is needed for further model assessment and development and requires observations of snow accumulation spanning from the branch scale of processes to the stand scale of models.

UAV lidar technology provides a unique opportunity to measure both subcanopy snow depth and forest canopy structure at the scale of branches, across forest stands. Assumptions of sampling uniformity commonly used to characterize snow depths and vegetation densities from airborne lidar observations may not be appropriate for higher-resolution and lower-power applications of UAV lidar observations and therefore require careful consideration.

This research is designed to improve the current understanding of snow interception and accumulation processes in needleleaf forests. Novel and traditional methods are used in parallel to measure and analyze the relationships between canopy structure and subcanopy snow accumulation in needleleaf forests down to the scale of branches. Results are then discussed in the context of physical processes of snow-vegetation interactions. Understanding the physical processes relating branch-scale snow-vegetation interactions to stand-scale snow accumulation and interception is a fundamental component of building robust models and making informed land management decisions.

1.4.1 Research purpose

The purpose of this research is to quantify the branch-scale effects of canopy on the spatial patterns of snow accumulation and interception within a cold region needleleaf forest.

1.4.2 Research objectives and questions

Two objectives were identified to pursue the purpose of this research:

1. Assess the implications of UAV lidar beam occlusion in needleleaf canopies for branch-scale observations of snow and vegetation in forests.

   This objective is guided by the following questions:
   a. To what extent does occlusion of the subcanopy surface by evergreen canopy vegetation result in biased areal snow depth estimates from UAV lidar?
   b. How significant are the effects of nonuniform UAV lidar sampling of vegetation due to beam occlusion on vegetation density and light transmittance metrics?

2. Relate spatial patterns of snow accumulation and interception to branch-scale spatial patterns of evergreen canopy structure.

   This objective is guided by the following questions:
   a. How do the spatial distributions of branch-scale snow and canopy metrics compare between the forest and clearing, and with previous observations in the literature?
   b. How do spatial distributions of subcanopy SWE and ΔSWE relate to branch-scale canopy structure?
   c. How can the observed relationships between subcanopy snow accumulation and canopy structure be explained by physical processes of snow accumulation?

1.4.3 Thesis layout

Chapter 2 describes the methodology which is fundamental to all subsequent chapters, including study site and study period descriptions, data collection, processing, and analysis methods.
Chapter 3 presents methodological considerations for analysis of UAV lidar observations for canopy and subcanopy snow metrics, in support of Objective 1.
Chapter 4 investigates the spatial relationships between snow and canopy metrics and the corresponding processes, in support of Objective 2.
Chapter 5 summarizes the conclusions from research presented in the previous chapters and discusses directions for future research.

Chapter 2: Methodology

2.1 Study site and period

This research was conducted in a secondary-growth forest located within Marmot Creek Research Basin (MCRB) in the Kananaskis River Valley, Alberta, Canada. MCRB forms part of the headwaters of the South Saskatchewan River Basin on the eastern slope of the Canadian Rocky Mountains (50.9570°N, -115.1760°W). The 17,144 m^2 site ranges in elevation from 1815 m – 1841 m above mean sea level (AMSL) and has an average slope of 7° to the NE. Vegetation consists primarily of Engelmann spruce (*Picea engelmannii*), subalpine fir (*Abies lasiocarpa*), and lodgepole pine (*Pinus contorta var. Latifolia*), patches of which were logged and cleared in the 1970s as part of a forest snow hydrology experiment (see Rothwell et al., 2016) and which have since seen partial juvenile regrowth (Figure 2.1).

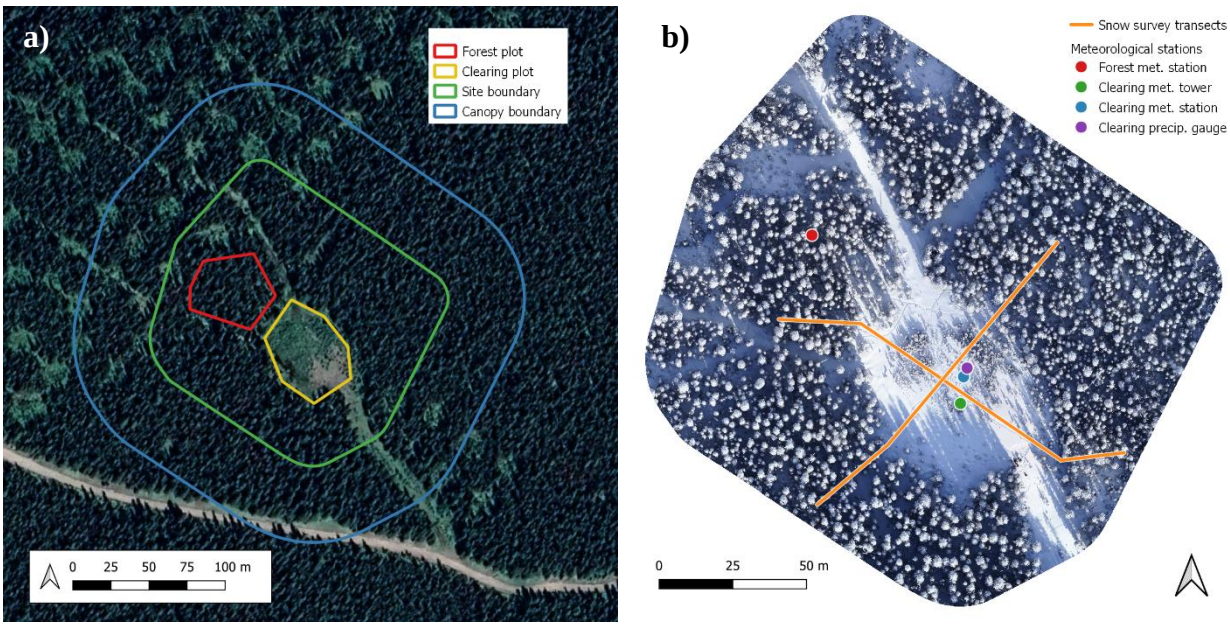

Figure 2.1: (a) Site overview from satellite imagery (Google maps). Lidar-derived snow and canopy metrics were calculated over the extent of the site boundary (green), which was derived from a 15 m buffer of the outermost UAV flight path. Canopy structure analysis considered vegetation up to 50 m away from each ground point, with the outermost canopy extent shown in blue. Plot-specific analysis was conducted separately for each of the forest (red) and clearing (yellow) plots. (b) Locations of snow survey transects and meteorological stations within the site, plotted over an orthomosaic of the site generated from UAV photography collected on 21 Feb. 2019 and compiled using structure from motion with the Pix4D software (v. 4.6.2).

Between 2006 and 2016 the large clearing received an average of 362 mm of snowfall annually (Xing Fang et al., 2019). As little as 50% of seasonal snowfall at this site has been found to reach the forest floor, with the remainder primarily lost to interception by the canopy and subsequent sublimation back into the atmosphere (Ellis et al., 2010; X. Fang et al., 2013).

An array of instruments has been established and maintained across the site to monitor and record meteorological and hydrological conditions (see Fang et al., 2019 for a full description of instrumentation and for published datasets). 15-minute time series from the forest and clearing meteorological stations were utilized in this study (Figure 2.1.b), including acoustic snow depth, air temperature, relative humidity, and wind speed and direction. Additionally, 15-minute time series from the 17 m above ground surface (AGS) clearing meteorological tower were also used, including air temperature, wind speed and wind direction, as was 15-minute cumulative precipitation from the clearing precipitation gauge (Geonore T200B with Alter shield), corrected for undercatch following Smith (2007).

Figure 2.2: (top) clearing meteorological station on morning of 21 Feb. 2019, after storm 2.

Figure 2.3: (bottom) aerial view of clearing meteorological station in April 2013 (photo credit: John Pomeroy).

A suspended tree lysimeter was established in November 2018 to continuously measure the weight of a suspended juvenile spruce tree plus the intercepted snow load. A Sensortronics 60001A75-1000 s-type load cell connected to a CR10X data logger recorded the weight of the system every 15 minutes throughout the winter season (Figure 2.4).

The study period spanned 7 days – from 14 to 21 of February 2019 – during which time two distinguishable accumulation events ("storms") passed over the site (Figure 2.4). Within the study period three snow surveys were conducted (Table 2.1) – one each before, between, and after the two storms– resulting in two time intervals referred to chronologically as storm 1 and storm 2 (Table 2.2). Snow was observed in the canopy over the extent of the study period, referred to as "snow-on" canopy conditions. Air temperatures within the forest ranged from -8 °C to -23 °C over the study period, with relative humidity near saturation. Conditions were slightly cooler and calmer for storm 1 compared with storm 2, with median air temperatures of -15.5 °C and -12.6 °C and median wind speeds of 0.34 m s^{-1} and 0.45 m s^{-1} (Figure 2.5) at 17 m AGS for storms 1 and 2, respectively. The azimuths of the mean 17 m wind vectors were 136° and 125° clockwise from north for storms 1 and 2. Wind speeds within the forest at 2.77 m AGS reached maximum values of 0.205 m s^{-1} and 0.779 m s^{-1} with median values of 0.0 m s^{-1} and 0.108 m s^{-1} for storms 1 and 2, respectively.

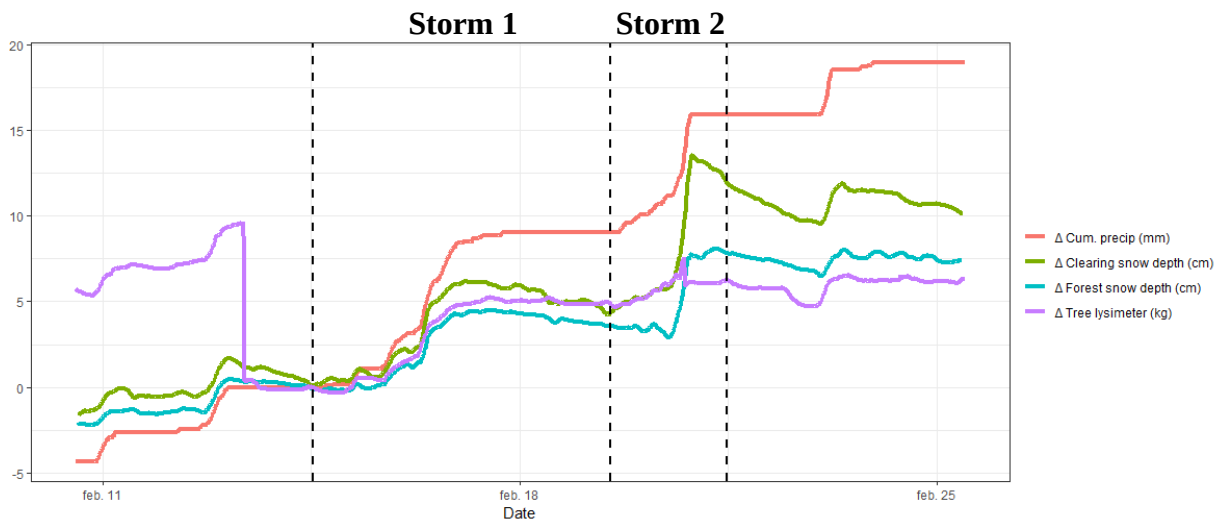

Figure 2.4: Changes in cumulative precipitation, tree lysimeter mass, and snow depths in the clearing and forest over the study period relative to the first survey date (Feb. 14). Dashed vertical lines correspond to the three field visits on 14, 19, and 21 of Feb. 2019. Two storms passed over the site over the study period which were bounded by surveys: storm 1 between 14 Feb. and 19 Feb. surveys, and storm 2 between 19 Feb. and 21 Feb. surveys.

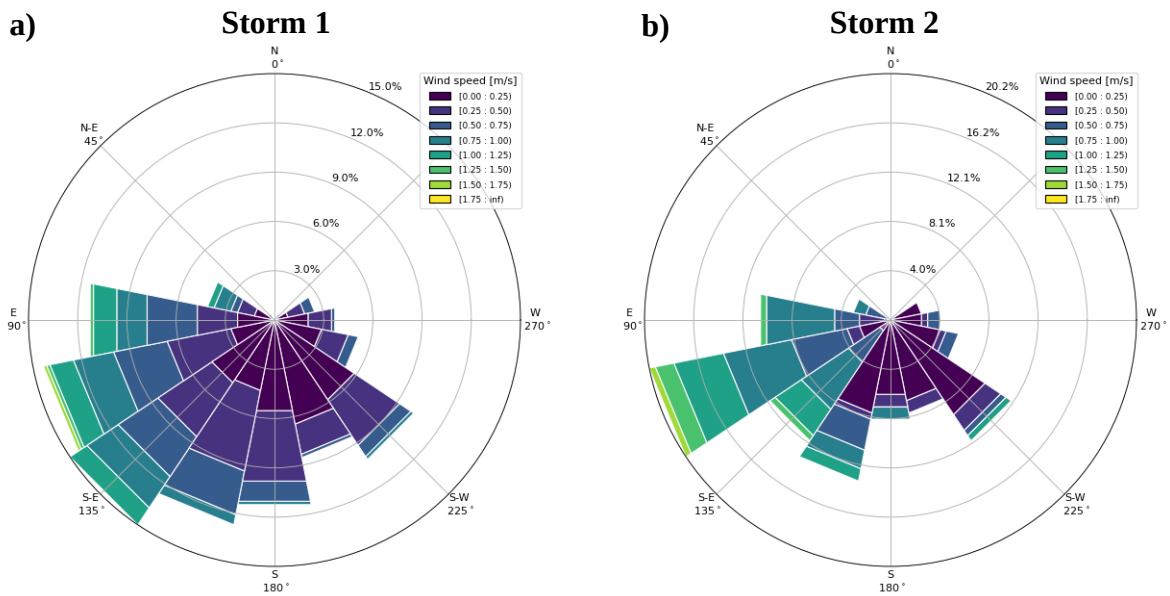

Figure 2.5: Normalized histograms of wind speed (m s^{-1}) and wind direction (° clockwise from north, upward looking) over the storm 1 (a) and storm 2 (b) observation periods. The upward-facing perspective from the ground (flipped east-to-west from conventional downward-facing perspective) is used for simplified visual comparison with hemispherical analysis in Figure 3.3 and Figure 4.12. Plots were generated using the Python windrose package (v.1.6.8).

2.2 Data collection

2.2.1 Field visits

Eight visits to the field site at Marmot Creek Research Basin were carried out between November 2018 and May 2019 to establish a suspended tree lysimeter, and to conduct UAV lidar surveys and manual snow surveys specific to this study. All materials were transported 7 km from winter road access to the site and back, with over 380 m elevation gain each day. This involved transportation of over 40 kg of equipment on ski and on foot, and occasionally by ski lift and snowmobile with help from the nearby Nakiska Ski Area operations team. Field days took approximately 8 hours car-to-car, with approximately 4.5 hours at the field site each day.

Figure 2.6: (left) Snow in the trees and on the ground at the field site and (right) view of the clearing tower meteorological station on 14 Feb. 2019

Figure 2.7: Several examples of intercepted snow on vegetation observed on visits to the field site.

2.2.2 UAV-lidar data collection and preprocessing

Six UAV-lidar surveys of the field site were conducted between 14 February 2019 and 29 May 2019, comprising 5 snow surveys and 1 bare ground survey (see Table 2.1). Two surveys conducted outside of the study period were processed but were not included in the final analysis. Lidar observations were collected using a RIEGL miniVUX-1UAV lidar sensor and integrated Applanix APX-20 inertial measurement unit (IMU), mounted on a DJI M-600 Pro uncrewed aerial vehicle (UAV, see Harder 2020 for detailed platform specifications). The laser beam from this device has a wavelength of 905 nm with primary-axis beam divergence of 1.6 mrad and a beam waist of 0.34 mm. A 45° rotating mirror results in a 360° cylindrical scanning pattern, with the axis of rotation parallel to the flight path. Lidar samples were collected at a rate of 100 kHz with a mirror rotation speed of 50 Hz. The miniVUX-1UAV conducts onboard processing of the lidar waveforms to produce a discrete-return output with up to 5 returns per shot. The combined system results in a horizontal accuracy of < 0.05 m and vertical accuracy of < 0.1 m for individual lidar returns (Harder et al., 2020). A co-registered Sony a6000 RGB camera collected aerial photos of the ground every 2 seconds.

Figure 2.8: (left) Preparation of the UAV and lidar systems at the field site on 17 April 2021. (right) UAV platform in operation (photo credit: Alistair Wallace).

Six pre-programmed flight paths were paired up and executed across 3 flights for each survey, with each flight limited to 15 minutes due to battery capacity. The polygon created by the outermost flight path fully contained the forest and clearing plots, all met stations, and all ground survey transects. Three different classes of flight patterns were implemented to provide more varied perspectives of the canopy and forest floor from the sensor compared with that of a single elevation scanning pattern, taking advantage of the agility of the UAV platform. Flight paths were built and executed using the UgCS flight control software (SPH Engineering, 2020).

Lidar, IMU, and GNSS observations were integrated into georeferenced lidar point clouds following the workflow of Harder et al. (2020). Post-processed flight trajectories were generated by reconciling the APX-20 IMU data with GNSS observations from the UAV platform, georeferenced with PPP-corrected base station GNSS observations (Natural Resources Canada, 2021) using the POSPac UAV software. Lidar return point clouds were then converted from a sensor-referenced to georeferenced frame using the proprietary RIEGL RiPROCESS software.

Table 2.1: Survey dates and corresponding snow observations. Cumulative precipitation measured by the precip. gauge is reported from 1 October 2018. A linear snow density with depth relationship was assumed for the clearing plot with slope and intercept values shown, while a constant density was assumed within the forest plot, for each day. The final survey on 29 May 2019 was used for analysis of the snow-free ground surface. Two additional surveys conducted outside of the study period were omitted from analysis (see Appendix A).

Date	Day of year	UAV survey end time	Cumulative clearing precip. gauge SWE [mm]	Clearing SR50 HS [cm]	Forest SR50 HS [cm]	Clearing snow density intercept b_c [kg m^{-3}]	Clearing snow density slope m_c [kg m^{-4}]	Forest snow density constant ρ_f [kg m^{-3}]
2019-02-14	045	12:55	171	57.0	32.8	109	1.27	165
2019-02-19	050	12:41	180	60.9	36.4	118	1.09	159
2019-02-21	052	11:40	187	68.4	40.6	76.7	1.44	134
2019-05-29	145	11:54	326	0	0	n/a	n/a	n/a

The georeferenced lidar point cloud from each survey day was then subject to quality control measures and surface and vegetation return classification using the LAStools software package (Isenburg, 2020). Batch scripts of the quality control code can be found at https://github.com/jstaines/upper-clearing-lidar/tree/master/lastools. Point clouds were cropped to the region of interest, defined by a 15 m lateral buffer of the outermost flight path for ground analysis, and 65 m buffer for canopy analysis (green and blue paths in Figure 2.1.a, respectively). Duplicate points were dropped. Surface returns (whether ground or snowpack) were identified from the subset of last returns using the Lastools "lasground_new" function with a step size of 0.5 m and an offset of 0.1 m, removing upward and downward spikes greater than 0.1 m. Each set of surface returns was then thinned to the finest scale of interest by selecting the surface return with the median elevation within each 5 cm-by-5 cm cell, to minimize the presence of vertical outliers from low-lying vegetation. Vegetation returns were subsequently identified as those with elevations within 0.05 m - 35 m above the ground surface. Returns with no neighbors within the surrounding 1 m x 1 m x 1 m cube were flagged as noise and removed. Processed point clouds yielded a mean return density of 3860 returns m^{-2} over the forest plot, consisting of 3090 first returns m^{-2} and 839 surface returns m^{-2}.

2.2.3 Snow surveys

Ground-based snowpack observations were collected following the completion of each aerial survey to validate and supplement aerial surveys. Snow surveys were conducted along two perpendicular transects originating and terminating in the forest and traversing the clearing plot (Figure 2.1.b). A minimum total of 20 clearing and 20 forested snow depth samples were collected at regular intervals along the transects. Destructive SWE measurements were taken with an ESC-30 snow tube at every other snow depth point where snow depth exceeded 20 cm. All snow depth and SWE sample points were surveyed with a differential GPS (dGPS) rover where signal quality permitted for point validation of LiDAR-derived snow depth and SWE estimates.

2.2.4 Hemispherical photography

Upward-looking hemispherical photographs were collected with a Nikon Coolpix 4500 and EC-F8 hemispherical lens, from 1.8 m above the ground at georeferenced points of 5 m intervals along the snow survey transects, following each UAV survey (n = 20). Hemispherical photographs were inspected for quality control, cropped to the hemispherical horizon, resized to 1000x1000 pixels, and thresholded manually over all RGB channels to differentiate between sky and canopy (including any intercepted snow) pixels. In some cases, particularly when snow was present in the canopy, a single threshold was insufficient to differentiate the canopy from the sky, and manual darkening or lightening was applied to discrepant regions prior to thresholding. Images were then analyzed in the Hemisfer software (Version 2.2, Thimonier et al., 2010) across 4 angle bands of 15° width spanning 0-60° from vertical to calculate average band transmittance, weighted by within-band solid angle (Schleppi et al., 2007).

2.3 Lidar snow products

2.3.1 Lidar snow depth

Lidar-derived snow depth (HS_{lidar}) was calculated for each day within the study period using a point-to-grid subtraction method (Deems et al., 2013). A triangular irregular network (TIN) was generated from the thinned snow-free ground returns to represent the bare ground surface. Each thinned snow surface return was normalized to the height above ground by subtracting the bare ground TIN elevation at the corresponding coordinates from the return elevation, yielding a point cloud of snow depths from which a snow depth TIN was generated. Each snow depth TIN was then rasterized to resolutions of 5 cm, omitting TIN edges which exceeded 10 cm to omit cell values derived from interpolation over relatively large distances, referred to as “limited interpolation”. Fully interpolated products (with no maximum TIN edge length) were also generated for comparison with the limited interpolation products. Lidar snow depths were bias-corrected for each day with a constant offset by minimizing error with the manual snow depths (see Appendix B) to correct for centimeter-scale discrepancies in elevation georeferencing between surveys, similar to Broxton et al. (2019). The snow depth products were then cleaned by

excluding negative values and those which exceeded the .999th quantile, and masking regions where snow was trampled due to snow surveys and two remaining snow patches in the "bare ground" survey.

2.3.2 Lidar SWE

The spatial distribution of snow water equivalent within the forest (SWE_f) and within the clearing (SWE_c) were estimated with two independent density models derived from snow survey observations (see Appendix B). Within the forest the density of the shallow snowpack did not show a significant relationship with snow depth, consistent with the findings of Shook and Gray (1994) for prairie snowpacks less than 60 cm in depth. Constant density models were therefore used to estimate SWE_f [mm] from HS_{lidar} [m] within the forest for each survey day:

$$SWE_f = \rho_f \cdot HS_{lidar} \qquad \text{Eq. 2.1}$$

where ρ_f [kg m^{-3}] is the mean snow density calculated from daily forest snow survey observations. In contrast, the density of the deeper snowpack found within the clearing yielded a significant linear relationship with snow depth for two of the three surveys within the study period (see Appendix B). SWE_c [mm] within the clearing was therefore estimated from HS_{lidar} for each day using linear models of snow density with depth:

$$SWE_c = \rho_c \cdot HS_{lidar} \qquad \text{Eq. 2.2}$$

where ρ_c [kg m^{-3}] is the clearing snow density calculated by:

$$\rho_c = m_c \cdot HS_{lidar} + b_c \qquad \text{Eq. 2.3}$$

with snow depth coefficient m_c [kg m^{-2}] and intercept b_c [kg m^{-3}] calculated from linear regressions of daily snow survey observations within the clearing plot.

2.3.3 Lidar ΔSWE

The spatial distributions of changes in snowpack snow water equivalent over the two storms were estimated independently over the forest (ΔSWE_f) and clearing (ΔSWE_c) plots, for each sample interval within the study period (Table 2.2). ΔSWE values were calculated from ΔHS_{lidar} rather than differences in consecutive SWE_f and SWE_c estimates to avoid sensitivity to noise in daily snowpack density models. Densities of newly fallen snow at the end of each time interval ρ_{new} were estimated from 15-minute time series of air temperature T_a and snow depth HS from sensors located within each corresponding plot. The HS time series were collected with SR50 acoustic sensors were corrected for speed of sound fluctuations with air temperature (Campbell Scientific Canada, 2009) and smoothed using a 3.25 h moving average to minimize noise prior to analysis (Ryan et al., 2008).

Table 2.2: Interval dates and corresponding snow observations. Two additional intervals fell outside of the study period and were not considered in analysis (see Appendix A).

Sample interval name	Date interval	DOY interval	Clearing precip. gauge ΔSWE [mm]	Clearing SR50 ΔHS [cm]	Forest SR50 ΔHS [cm]	Clearing new snow density [kg m^{-3}]	Forest new snow density [kg m^{-3}]
Storm 1	2019-02-14 to 2019-02-19	045-050	9.03	3.9	3.6	96.9	85.1
Storm 2	2019-02-19 to 2019-02-21	050-052	6.85	7.5	4.2	83.4	72.2

One distinct accumulation event was identified within each sample interval time series by the temporal range of minimum to maximum snow depths (HS_{min} to HS_{max}). The fresh snow density ρ_{fresh} [kg m^{-3}] for each accumulation event was estimated from the empirical model proposed by Hedstrom and Pomeroy (1998):

$$\rho_{fresh} = 67.92 + 51.25 \cdot e^{\frac{T_a}{2.59}} \qquad \text{Eq. 2.4}$$

where the air temperature T_a is the mean air temperature over the accumulation event. Relaxation of the snow depth between the maximal snow depth HS_{max} and the snow depth at the end of the interval HS_{obs} is assumed to be exclusively from densification of the new snow layer (Lv & Pomeroy, 2020), yielding the following estimate for ρ_{new}:

$$\rho_{new} = \rho_{fresh} \cdot \frac{HS_{max} - HS_{min}}{HS_{obs} - HS_{min}} \qquad \text{Eq. 2.5}$$

ΔSWE_f (within the forest) and ΔSWE_c (within the clearing) were calculated for each sample interval by scaling the raster-wise difference in lidar snow depths ΔHS_{lidar} over a given interval by the respective new snow density ρ_{n}:

$$\Delta SWE = \rho_{new} \cdot \Delta HS_{lidar} \qquad \text{Eq. 2.6}$$

with separate ΔSWE_f and ΔSWE_c estimates from ρ_{new} values calculated from forest and clearing sensor arrays and for each respective sample interval.

2.3.4 Rejection sampling of airborne lidar snow products

Snowfall is not the only process that is spatially influenced by vegetation: airborne lidar observations of snow and ground surfaces are often occluded by vegetation, resulting in fewer observations below dense vegetation than in gaps. When sample coverage of the subcanopy is biased away from vegetation, significant covariance between snow depths and subcanopy return densities from airborne lidar observations may therefore indicate that areal distributions of

observed snow depths product are not representative of true snow depth distributions. At the same time, nonuniform sampling due to overlapping flight lines and sensor roll-pitch-yaw variations presents challenges to relating snow depths and ground return densities explicitly. With specific regard to rasterized snow depth products, there is a need to assess and correct for systematic bias in areal statistics calculated from observed subcanopy surface pixels to make them representative of all pixels within a region of interest – both observed and unobserved.

To address this, rejection sampling was used to resample the set of observed pixels to compensate for bias with vegetation density (Bolstad, 2009). For this application a secondary metric related to beam occlusion by vegetation and insensitive to sample density was needed. The laser penetration metric considering first and last returns (*LPM-L*) proposed by Alonzo et al. (2015) was selected for this purpose, calculated from lidar returns with scanning angles within ±15° from nadir by:

$$LPM\text{-}L = \frac{g_F + g_L}{g_F + g_L + c_F} \qquad \text{Eq. 2.7}$$

where g_F and g_L are the counts of first and last ground returns, and c_F is the count of first canopy returns, within a given pixel. The normalized *LPM-L* distribution over the set of observed pixels (*O*) was resampled by piecewise rejection sampling using the normalized *LPM-L* distribution over all pixels (*E)* as the target distribution. Both distributions were binned by equal quantiles of *E* (n=50). Observed pixels within each bin *b* were then randomly accepted into the resampled subset with a probability of:

$$r_b = m\frac{E_b}{O_b} \qquad \text{Eq. 2.8}$$

where O_b and E_b are the quantiles of the corresponding distributions found within bin *b*, and $m = min_b(O_b / E_b)$ is a scaling constant to ensure that the target distribution is greater than the sample distribution for all bins. This results in a resampled subset of observed pixels whose *LPM-L* distribution representative of all pixels, correcting for bias in areal snow depth distributions associated with snow depth and ground return density covariance with *LPM-L*. The total acceptance rate is found by:

$$R = \frac{\sum_b r_b E_b}{\sum_{b'} E_{b'}} \qquad \text{Eq. 2.9}$$

In the case of no significant sample bias with vegetation density, the normalized arial distributions of *LPM-L* for all pixels (*E*) and for the set of observed pixels (*O*) are statistically similar, and the rejection sampling operation results statistically in an identity relation. In

general, however, these distributions differ. Note that the acceptance rates r_b can also be used as weights for importance sampling (Bolstad, 2009).

2.4 Lidar canopy products

Lidar observations were used to characterize the canopy structure over the site using a variety of different methods. Light transmission metrics were calculated from the lidar observations using two methods in parallel: point cloud reprojection and voxel ray sampling. Some elements of the voxel ray sampling methodology are novel, adapted voxel ray tracing methods found in the literature to address some of the known issues with the point cloud reprojection methods. Voxel ray sampling and point cloud reprojection were used in parallel to provide a comparison of the novel and traditional methods in both validation and application contexts. Additional metrics which are not conceptually rooted in light transmission of the canopy were calculated from lidar observations following existing methods found in the literature.

2.4.1 Vegetation characterization from lidar point cloud reprojection

Synthetic hemispherical images were generated by hemispherical reprojection of the snow-off lidar point cloud following methodologies by Varhola et al. (2012) and Moeser et al. (2014). The snow-off point cloud was transformed to a spherical reference frame with origin located at the reference coordinates of interest. Points coordinates were flipped east-to-west to simulate the upward-looking perspective. Distant points beyond 50 m from the origin were omitted due to reduced influence on modeled transmittance (Alexander et al., 2013) and to increase computational efficiency. Points were then filtered to the upper hemisphere and flattened in the radial dimension. The reprojected were plotted with point area weighted by the inverse-square of distance from origin (Moeser et al., 2014), with an optimized scalar term determined by minimizing the solid-angle-weighted squared error of band-wise transmittance with corresponding georeferenced hemispherical photography (see Appendix C). Images were output in 8-bit greyscale format with pixel values corresponding to fractional cover of each pixel by projected points, before being thresholded at a value of 127 ($\gamma = 2.2$). The point cloud reprojection algorithm was scripted in Python (version 3.7.9) utilizing the laspy package (version 1.7.0) and can be found at https://github.com/jstaines/upper-clearing-lidar/blob/master/python/libraries/laslib.py (function "hemigen"). A total of 1944 reprojected synthetic hemispherical images were generated over a 1 m grid across the forest plot at 25 cm AGS, with dimensions of 1000x1000 pixels, and with an average of 1.39×10^7 points per image. Computation time for synthetic images by point reprojection was approximately 154 seconds per image when generated in series using a personal computer with Intel i7-7500U processor.

Reprojected synthetic hemispherical images were analyzed using the Hemisfer software (Version 2.2, Thimonier et al., 2010), with metrics calculated from each image shown in Table 2.3. Transmittances and contact numbers were estimated for each of the four zenith angle bands 15° in width spanning 0°-60°, for each image. Angles beyond 60° were omitted from analysis due to

observed sensitivity to the 50 m max distance cut-off (see Appendix E). LAI_{2000} was calculated over the four angle bands by extrapolating the fourth band to the horizon (Stenberg et al., 1994; Thimonier et al., 2010).

Table 2.3: Canopy metrics calculated from hemispherical analysis of synthetic hemispheres generated by reprojection of the lidar point cloud from snow-off canopy conditions surveyed on 27, May 2019 and are annotated (•) to differentiate metrics from similar metrics calculated by voxel ray sampling of lidar (▲ or △).

Symbol	Metric name	Calculation
$T_{(a-)b}^{\bullet}$	Light transmittance by angle band [-]	Fraction of light pixels in thresholded hemispherical photograph for angle band $\phi \geq$ a° (or 0° if not stated), $\phi <$ b°, corrected for within-band solid angle (Schleppi et al., 2007)
$\chi_{(a-)b}^{\bullet}$	Contact number by angle band [-]	Average band-wise contact number $\chi_{(a-)b}^{\bullet} = -ln\left(T_{(a-)b}^{\bullet}\right)$ for angle band $\phi \geq$ a° (or 0° if not stated), $\phi <$ b°
$LAI_{2000}^{\bullet}$	LICOR LAI-2000 [-]	Leaf area index calculated from the weighted average of $\chi_{a-b}^{\bullet} \cdot \cos(\phi)$ for the four angle bands {0-15°, 15-30,° 30-45°, 45-60°} with weights {.034, .104, .160, 0.702} (LICOR), corrected for canopy clumping (Jing M. Chen and Cihlar, 1995) and within-band solid angle (Schleppi et al., 2007)
$CC^{\bullet}$	Canopy closure [-]	$1 - T_{60}^{\bullet}$

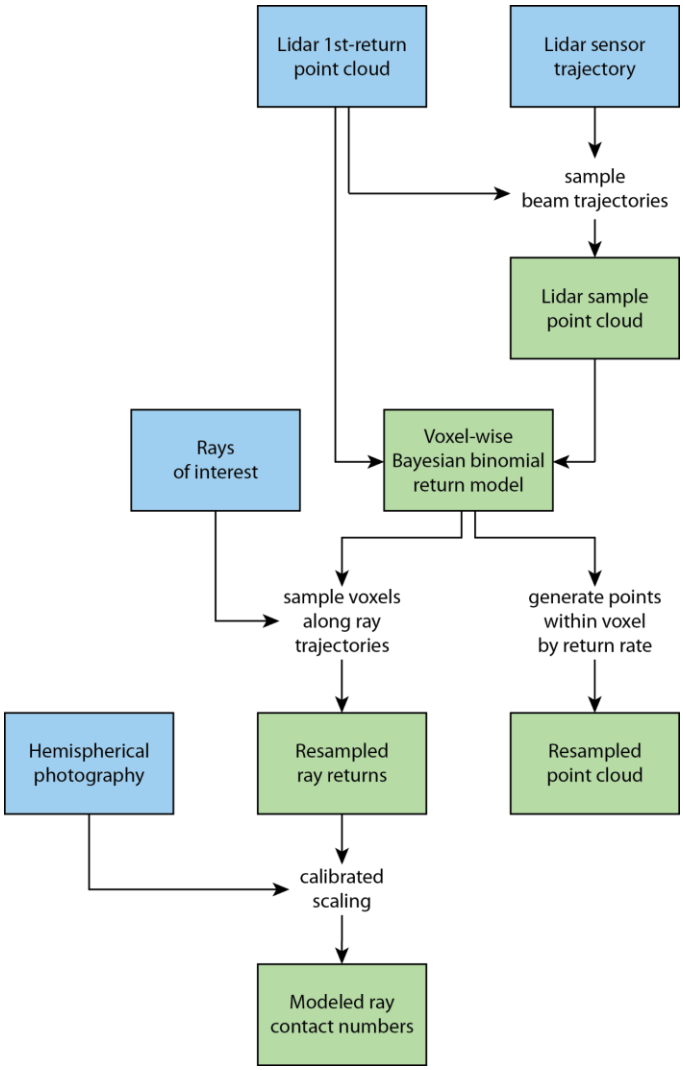

Figure 2.9: Data workflow for voxel ray sampling of lidar, with data inputs (blue), processes (white), and data products (green).

2.4.2 Vegetation characterization from voxel ray sampling of lidar

To quantify vegetation density at high spatial and angular resolution, a novel ray sampling method was developed in Python for estimating vegetation contact number along arbitrary rays through the canopy from discrete return lidar observations (code can be found at https://github.com/jstaines/upper-clearing-lidar/tree/master/python/voxel_ray_sampling_of_lidar). This method utilizes georeferenced lidar sensor trajectories in combination with the point cloud of first returns to create a voxel-wise Bayesian model of lidar return probability over the sampled region. The voxel model is then resampled along rays of interest, with a scalar correction for lidar beam specifications, to arrive at estimates of contact number (Figure 2.9). Resampled point clouds were also generated, with volumetric point densities related to modeled return rates and insensitive to sample density. The

development of this method was motivated by the need for high resolution vegetation density metrics which are insensitive to the non-uniform point sampling typical of lidar sampling of vegetation (Webster, 2017).

Voxel ray sampling of lidar is built on the consideration of the network of beam samples through space in addition to discrete lidar returns. Only intact beams are considered in this analysis to limit dependence of return probability on return number. The point cloud of first returns is therefore merged in time with the corresponding lidar sensor trajectory to create a dataset of uninterrupted lidar beams. The rays formed by each sensor-return pair are then point-sampled at a regular interval length L_S, with a random offset from the sensor drawn from the interval $[0, L_S)$ for each ray to avoid synchrony between related rays, yielding a point cloud of lidar ray samples.

A 3-dimensional voxel map is generated over the region of interest using uniform cubic volumes of side-length L_{vox}. The number of lidar first returns (k) and lidar samples (n) found within each voxel is then recorded. Note that $n * L_S$ is a computationally efficient estimate of the total length of lidar beam which has traversed a given voxel, avoiding explicit ray tracing which can be computationally expensive.

The probability of a return given a beam sample p_r is modeled for each voxel with a binomial likelihood given n trials (samples) and k successes (returns):

$$P(p_r|n,k) = \binom{n}{k} p_r^k (1-p_r)^{n-k} \qquad \text{Eq. 2.10}$$

In the relatively few cases where $n < k$, n was updated to $n = k$ to reflect that each observed return requires a minimum of one unique sample within a given voxel, thereby constraining p_r to the range [0, 1] valid for a binomial distribution. Note that, as there is no consideration of incident lidar beam angle in this calculation, equivalent to assuming a spherical (random) leaf angle distribution below the voxel scale.

A *beta*(α, β) distribution was selected as the conjugate prior for a binomial likelihood (Bolstad and Curran, 2016) to yield an analytical posterior distribution. A beta prior with parameters (α_{prior}, β_{prior}) was selected to match the mean μ_{prior} and variance σ^2_{prior} of return rates over the whole observed data set, yielding prior parameters:

$$\alpha_{prior} = \left(\frac{1-\mu_{prior}}{\sigma^2_{prior}} - \frac{1}{\mu_{prior}}\right) \cdot \mu^2_{prior} \qquad \text{Eq. 2.11}$$

$$\beta_{prior} = \alpha_{prior} \cdot \left(\frac{1}{\mu_{prior}} - 1\right) \qquad \text{Eq. 2.12}$$

where $\mu_{prior} = \sum_i k_i / n_i$ and $\sigma^2_{prior} = \sum_i \left(\mu_{prior} - k_i/n_i\right)^2$, and where *i* is the set of voxels with $n_i > 0$. The posterior distribution of a binomial likelihood with a beta prior is a beta distribution with posterior hyperparameters:

$$\alpha_{post} = \alpha_{prior} + k \qquad \text{Eq. 2.13}$$

$$\beta_{post} = \beta_{prior} + n\frac{L_S}{L_R} - k \qquad \text{Eq. 2.14}$$

The resulting posterior distribution $beta(\alpha_{post}, \beta_{post})$ provides a model for the likelihood of a lidar return given a lidar sample within each voxel.

The voxel-wise Bayesian binomial return model is then resampled along rays of interest to yield resampled returns without beam occlusion. The expected number of returns along an arbitrary ray *B* is calculated as the sum of return probability distributions of the voxels found from resampling along ray *B*. A series of samples is generated with constant resample interval length L_R, offset by uniform sub-step noise in phase to avoid synchrony with related rays. Each sample along the ray is assigned the binomial probability distribution of the voxel it is found within. The probability of the sum of many binomial distributions is found by their collective convolution, the analytical form of which is generally unknown. The cumulative distribution of returns from many samples along a ray is approximated by a normal distribution following central limit theorem, calculated parametrically as a function of the means and variances of all composite return distributions. The mean $\langle \mu_B \rangle$ and variance $\langle \sigma^2_B \rangle$ of the cumulative expected returns for each sample along a given ray are found by (Bolstad and Curran, 2016):

$$\langle \mu_B \rangle = \sum_B \frac{\alpha_{post}}{\alpha_{post} + \beta_{post}} \qquad \text{Eq. 2.15}$$

$$\langle \sigma^2_B \rangle = \sum_B \frac{\alpha_{post} \cdot \beta_{post}}{\left(\alpha_{post} + \beta_{post}\right)^2 \cdot \left(\alpha_{post} + \beta_{post} + 1\right)} \qquad \text{Eq. 2.16}$$

The theoretical relationship between lidar returns and contact numbers depends on many factors including lidar wavelength, vegetation reflectance, discrete return threshold intensity, beam length, diameter, angular divergence, and occlusion by vegetation (Béland et al., 2011; Hancock et al., 2017; Grotti et al., 2020). These intensive calculations and validations were avoided by establishing an empirical correction factor c_χ between the expected returns $\langle \mu_B \rangle$ and contact number χ_B:

$$\chi_B = c_\chi \langle \mu_B \rangle \qquad \text{Eq. 2.17}$$

with corresponding uncertainty:

$$\sigma_{\chi_B}^2 = c_\chi \langle \sigma_B^2 \rangle \qquad \text{Eq. 2.18}$$

Substituting Eq. 2.17 into Eq. 1.15 yields an estimate of transmittance along ray *B*:

$$T_B = e^{-\omega\, c_\chi \langle \mu_B \rangle} \qquad \text{Eq. 2.19}$$

This method results in estimates of contact number and transmittance along arbitrary rays, with flexible spatial and angular resolutions and limited sensitivity to nonuniform lidar sampling, where regions of lower sampling resulting in greater uncertainty with minimal bias of contact number estimates. Contact number correction factor c_χ was determined by minimizing the solid-angle-weighted squared error of band-wise transmittance with that from corresponding georeferenced hemispherical photography, considering the four zenith angle bands of 15°-width from 0° to 60° (see Appendix D).

The voxel-wise Bayesian binomial return model was also used to generate a resampled point cloud with volumetrically uniform sampling rates. Points were iteratively generated with a probability of $\mu_{post} = \alpha_{post}/(\alpha_{post} + \beta_{post})$ within each voxel, for the desired number of samples per voxel. Uniform within-voxel noise was added to all point positions to randomize sampling. The resultant point cloud can then be passed to standard point cloud workflows for calculation of vegetation density and structure metrics which are insensitive to sample bias from vegetation self-occlusion.

Voxel ray sampling of lidar was conducted from lidar observations from both "snow-on" and "snow-off" canopy conditions, over the extent of the canopy boundary (Figure 2.1.a), spanning in elevation from the lowest to highest returns, and with a voxel length of L_{vox} = 25 cm and sample and resample lengths of $L_R = L_S = L_{vox} / \pi$. Snow-off canopy conditions were represented by the point cloud from 27 May 2019, while snow-on canopy conditions were represented by the aggregation of point clouds from the three survey dates within the February study period (see Table 2.1). The resulting voxel spaces contained 3.01×10^8 voxels (approximately 40% of which were below ground), comprising a total of 3.02×10^8 first returns and 3.99×10^9 samples for the snow-on point cloud, and 6.06×10^7 first returns and 2.32×10^9 samples for the snow-off point cloud. n was updated to $n = k$ in 0.46% and 0.16% of cases where $n < k$, for snow-on and snow-off cases respectively. Prior parameters μ_{prior} = 0.0104 and σ^2_{prior} = 0.0733 for the snow-on case and μ_{prior} = 0.0117 and σ^2_{prior} = 0.0766 for the snow-off case were calculated from the subset of voxels where $n > 0$. Optimization yielded ωc_χ = 0.372 for snow-on and ωc_χ = 0.387 for snow-off canopy conditions. Computation time for sampling of the voxel space was approximately 226 seconds per 10^6 lidar returns when generated in series using a personal computer with Intel i7-7500U processor.

Contact numbers were estimated at 31,123 points comprising a 25 cm grid at 25 cm AGS (above snow surface for the snow-on case) across the forest plot, along rays spanning the hemisphere at 1° angular resolution for a total of 25,445 rays per point, or 7.92×10^8 rays for each model run. Resampled point clouds were also generated for each model run with sample densities of 50 samples per voxel. Computation time for synthetic hemispheres by voxel ray sampling was approximately 4.27 seconds per image when generated in series using a personal computer with Intel i7-7500U processor. Image generation was parallelized for efficiency.

Several secondary products were calculated from the contact number datasets and resampled point clouds and are summarized in Table 2.4. Mean band-wise contact numbers were calculated over the 15° zenith angle bands spanning 0°-60°. Contact number bands beyond 60° were shown to under-estimate contact numbers due to the max distance cut-off of 50 m (see Appendix E). Mean band-wide contact numbers showed negligible sensitivity to angular resolution at 1°.

Table 2.4: Canopy metrics calculated from voxel ray sampling of lidar. All ray sampling metrics are annotated to distinguish between snow-off (▲) and snow-on (△) canopy conditions, and to differentiate from similar metrics calculated from point reprojection for snow-off canopy conditions (•).

Symbol	Metric name	Calculation
$\chi_{(a\text{-})b}$▲ $\chi_{(a\text{-})b}$△	Contact number by angle band [-]	Average contact number χ_B for $\phi_B \in$ [a°, b°) (a = 0° if not stated), weighted by solid angle
$T_{(a\text{-})b}$▲ $T_{(a\text{-})b}$△	Light transmittance by angle band [-]	Average light transmittance $T_B = e^{-\chi_B}$ for $\phi_B \in$ [a°, b°) (a = 0° if not stated), weighted by solid angle
LAI_b▲ LAI_b△	Leaf area index by angle band [-]	Average leaf area index $LAI_B = 2\,\chi_B \cos(\phi_B)$ for $\phi_B \in$ [0°, b°), weighted by solid angle
LAI_{2000}▲ LAI_{2000}△	LICOR LAI-2000 [-]	Leaf area index calculated from the weighted average of $\chi_{a\text{-}b} \cdot \cos(\phi)$ for angle bands {0-15°, 15-30°, 30-45°, 45-60°} with weights {.034, .104, .160, .702} (LICOR)
C_c▲ C_c△	Canopy closure [-]	1 - T_{75} (e.g., Hedstrom and Pomeroy, 1998; Moeser, Morsdorf, et al., 2015)
V_f▲ V_f△	Sky view factor [-]	Vertical projection of hemispherical light transmittance calculated as T_{75} weighted by $\cos(\phi_B)$ (e.g., Essery et al., 2008; Helbig et al., 2020)
MCH▲ MCH△	Mean canopy height [m AGS]	Mean height above ground of canopy points in resampled point cloud from voxel ray sampling

2.4.3 Other canopy metrics

Additional canopy metrics from the literature which are not conceptually rooted in light transmittance were calculated in Python for analysis with snow products and are shown in Table 2.5 (code can be found at https://github.com/jstaines/upper-clearing-lidar/tree/master/python/canopy_metrics).

Table 2.5: Additional canopy metrics considered in analysis with snow products

Symbol	Metric name	Calculation
CHM	Canopy crown height [m AGS]	Crown height above ground (Khosravipour et al., 2016)
DNT	Distance to nearest tree [m]	Horizontal Euclidean distance to nearest treetop, treetops classified following Khosravipour et al. (2016)
DCE	Distance to canopy edge [m]	Rectilinear horizontal distance (0.1 m steps) from 2 m AGS canopy edge (Mazzotti et al., 2019)
MCH	Mean canopy height [m AGS]	Mean height above ground of canopy points in lidar point cloud (e.g., Mazzotti et al., 2020)
fCov	Fractional canopy cover [-]	Fraction of canopy returns to total returns (Varhola and Coops, 2013)
LPM-L	Laser penetration metric [-] considering first and last returns	Eq. 2.7 (Alonzo et al., 2015)
MDC	Mean distance to canopy [m]	Mean distance to canopy calculated at 1.25 m AGS for 192 azimuthal directions (Moeser, Morsdorf, et al., 2015)
TGA	Total gap area [m^2]	Area of the polygon made by distance to canopy vectors at 1.25 m AGS for 192 azimuthal directions (Moeser, Morsdorf, et al., 2015)

Canopy crown height was calculated and treetops were identified over the site following Khosravipour et al. (2016). First a triangular irregular network (TIN) of the canopy crowns was created from the snow-free lidar point cloud in lastools using the spike-free methodology presented by Khosravipour et al. with a maximum tin edge of 30 cm (Isenburg, 2020). The canopy TIN was then rasterized to a canopy elevation model at 10 cm spatial resolution. A canopy crown height model (CHM) was then calculated over the site by subtracting the snow-free DSM from the crown elevations.

Treetops were identified from the canopy crown elevation model by morphologically opening the crown elevations with a disk of 70 cm diameter, representing the diameter of the smallest trees of interest (Khosravipour et al., 2016). The opened image was then morphologically reconstructed using the original crown elevations as a mask. Inverted morphological

“watersheds” within the canopy were returned by subtracting the reconstructed image from the crown elevations. Distinct watersheds were identified as isolated 8-connected features, with the watershed maximum corresponding to the local peak and the watershed area corresponding to the tree crown area. Peaks with a minimum height of 2 m AGS and minimum crown area of 1 m^2 were identified as treetops, the coordinates of which were recorded with subpixel noise added.

Distance from nearest tree (DNT) was calculated at 10 cm resolution across the site by calculating the horizontal Euclidean distance from each pixel to the nearest identified treetop. This assumes that trees are vertical such that bases of trees reside below their corresponding tree-tops and neglects any vertical distance components due to hillslope.

Distance from canopy edge (DCE) was calculated using the algorithm presented in Mazzotti et al. (2019). The 10 cm resolution CHM was thresholded at 1 m AGL yielding a binary mask of the canopy. The mask was then iteratively convolved with a 3 x 3-pixel kernel, and unmasked pixels with convolution values > 0 were identified as transition pixels in each iteration. The iteration (1, 2, ...) was recorded for all corresponding transition pixels, and transition pixels were then added to the mask for the next iteration run. By this process, the rectilinear distance (in pixel steps) of each open (non-canopy) pixel from the canopy edge was recorded. The process was repeated using the inverse canopy mask to measure the distance from the canopy edge of canopy pixels, with negative step values (0, -1, …) used to indicate distance from the edge away from open pixels. Output iterations were scaled by a factor of 0.1 m to indicate the rectilinear step size, equivalent to the CHM resolution.

Mean canopy height (MCH) [m AGS] was calculated from the snow-free resampled point cloud from voxel ray sampling. The point cloud was filtered for noise by removing points with less than 2 neighbouring points in the surrounding 0.75 m x 0.75 m x 0.75 m cube using the LAStools “lasnoise” function (Isenburg, 2020). Remaining points were normalized to height above the ground. The mean canopy height was then calculated as the mean elevation of points above 1 m AGS within a given pixel.

Fractional canopy cover fCov [-] was calculated as the fraction of first canopy returns over the total first returns within a given pixel, with counts limited to returns with scan angles within 15° from nadir. A laser penetration metric using first and last returns (LPM-L) [-] was also calculated following Alonzo et al. (2015) (see Section 2.3.4 for calculation).

Two canopy metrics were calculated from the vector search algorithm put forth by Moeser, Morsdorf, et al. (2015). The 0.25 m resolution canopy crown height model calculated following Khosravipour et al. (2016) from the snow-off lidar point cloud was thresholded at 1.25 m AGS and subsequently smoothed using a 3 x 3 pixel kernel. Each of 192 azimuthal vectors around a given point was then searched for the nearest value which exceeded 0.9, considering minimum

and maximum distances of 0.75 m and 50.75 m and a distance search resolution of 0.125, and the corresponding distance was recorded. Mean distance to canopy (MDC) [m] was calculated by:

$$MDC = \frac{\sum \mathrm{d_i}}{\mathrm{n}} \qquad \text{Eq. 2.20}$$

where d_i is the minimum distance [m] to canopy for azimuthal angle *i* and n = 192 is the number of azimuthal angles considered. Additionally, total gap area (TGA) [m^2] was calculated by:

$$TGA = \frac{\pi \sum \mathrm{d_i}^2}{\mathrm{n}} \qquad \text{Eq. 2.21}$$

2.5 Parameterizing canopy structure for modeling spatial variation of snow accumulation

Three parametrizations of canopy structure were considered for comparison with spatial variations in snow accumulation within the forest. The "Hedstrom-Pomeroy" model (Hedstrom and Pomeroy, 1998) and "Moeser et al." (Moeser, Stähli, et al., 2015) models were selected for analysis based on their prevalence in the literature. Both were developed to estimate snow accumulation on a snowfall event timescale, considering interception and unloading processes, and parameterize spatial variation by nonlinear combinations of canopy metrics. A third descriptive model – the "Gaussian snowfall" model – is a light transmittance analogue model for throughfall developed to explain observations from this research in terms of throughfall processes.

For all three models, mean mass flux rates for drip $(\overline{D})$, melt $(\overline{M})$, and snowpack sublimation $(\overline{V_{snow}})$ were assumed to be negligible over the two storm intervals compared to the mean rate of throughfall $(\overline{F})$ due to air temperatures well below zero and relative humidity near saturation over the study period. The mean rate of wind transport of snow out of each forested pixel $(\overline{W})$ was assumed to be negligible due to low wind speeds (< 0.3 m s^{-1}) within the forest over the study period. The mean rate of unloading from the canopy $(\overline{U})$ was assumed to be negligible compared to the mean rate of throughfall $(\overline{F})$ for each storm. The subsequent snowpack mass balance for a given pixel thus yields:

$$\Delta S_{snow} = \overline{F}\Delta t \qquad \text{Eq. 2.22}$$

such that changes in storage of the snowpack over each event are attributed to throughfall processes only.

2.5.1 Hedstrom-Pomeroy model

Hedstrom and Pomeroy (1998) estimated the mean rate of snow interception by a forest canopy over a given time interval by:

$$\overline{I_{HP}} = (S^*_{can} - S^0_{can})\left(1 - e^{-\frac{C_p \overline{P\uparrow}}{L^*}}\right) \qquad \text{Eq. 2.23}$$

where S^*_{can} is the maximum canopy storage, S^0_{can} is the antecedent canopy storage, C_p is the maximum plan area of the canopy (plus intercepted snow) per unit area of ground, and $\overline{P\uparrow}$ is the mean rate of event precipitation at the top of the canopy. Maximum canopy storage is parameterized as:

$$S^*_{can} = \bar{S}\left(0.27 + \frac{46}{\rho_{fresh}}\right) LAI \qquad \text{Eq. 2.24}$$

where $\bar{S}$ is a species-dependent max snow load scalar taken as $\bar{S}$ = 5.9 kg m^{-2} for spruce trees (Schmidt and Gluns, 1991) and ρ_{fresh} is the fresh snow density estimated by Eq. 2.4. Furthermore, C_p is parameterized by:

$$C_p = \frac{C_c}{1 - \frac{C_c\, u\, CHM}{w\, J}} \qquad \text{Eq. 2.25}$$

where C_c is the hemispherical canopy closure, u is the horizontal wind velocity, w is the vertical snow particle fall speed, CHM is the canopy crown height, and J is the downwind forested snow particle fetch.

For this study, the downwind forested particle fetch was assumed to be spatially homogenous and represented by:

$$\mathrm{J} = \max(\mathrm{CHM})\frac{u}{w} \qquad \text{Eq. 2.26}$$

where CHM is the 10 cm resolution canopy crown height. Horizontal wind speed u and particle fall velocity w were also assumed to be horizontally homogenous, cancelling out with the corresponding terms in Eq. 2.25, such that C_p becomes:

$$C_p = \frac{1}{\frac{1}{C_c} - \frac{CHM}{max(CHM)}} \qquad \text{Eq. 2.27}$$

Throughfall is then estimated from mean interception rate $\overline{I_{HP}}$ following Eq. 2.23 by:

$$\overline{\mathrm{F_{HP}}}\Delta t = \left(\overline{P\uparrow} - \overline{I_{HP}}\right)\Delta t \qquad \text{Eq. 2.28}$$

2.5.2 Moeser et al. model

Moeser, Stähli, et al. (2015) estimated the mean rate of snow interception by a forest canopy over a given time interval by:

$$\overline{I_M} = \frac{S^*_{can}}{1 + e^{-0.3\left(\overline{P\uparrow} - 13.3\right)}} \qquad \text{Eq. 2.29}$$

where $\overline{P\uparrow}$ is the mean rate of event precipitation at the top of the canopy and S^*_{can} is the maximum intercepted load, calculated by:

$$S^*_{can} = 20.819 + 2.167x_1 - 3.410x_1^2 + 55.761x_2 + 181.858x_2^2 - 2.493x_3 + 0.499x_3^2 \qquad \text{Eq. 2.30}$$

where x_1 = ln(MDC), x_2 = ln(C_c), and x_3 = ln(TGA). Here MDC is mean distance to canopy [m], C_C is canopy closure [-], and TGA is total gap area [m^2].

Throughfall is then estimated from mean interception rate $\overline{I_M}$ following Eq. 2.29 by:

$$\overline{\mathrm{F}_M}\Delta t = \left(\overline{P\uparrow} - \overline{I_M}\right)\Delta t \qquad \text{Eq. 2.31}$$

2.5.3 Gaussian snowfall model

The Gaussian snowfall model was developed to quantitatively compare relationships observed between ΔSWE_f and transmittance over the hemisphere between events and canopies. The model of canopy light transmittance was adapted to describe the mean canopy snowfall transmittance over a given time interval $\left(\overline{T^*_{i,j}}\right)$ along a given ray (i, j) as:

$$\overline{T^*_{i,j}} = \frac{\overline{P\uparrow_{i,j}}}{\overline{F_{i,j}}} \qquad \text{Eq. 2.32}$$

where $\overline{P\uparrow_{i,j}}$ is the mean rate of above-canopy snowfall over the time period along ray (i, j), $\overline{F_{i,j}}$ is the mean rate of throughfall over the time period along ray (i, j), $i = (\phi_i, \theta_i)$ is the angle of the ray with zenith angle ϕ_i and azimuth θ_i, and $j = (x_j, y_j)$ is the geographical coordinates of the point at which the ray intersects the ground surface. The mean throughfall at point j ($\overline{F_j}$) was determined by rearranging Eq. 2.32 and integrating over all angles i in the upper hemisphere:

$$\overline{F_j} = \int_i \overline{P \uparrow_{i,j}} \cdot \overline{T^*_{i,j}}\, di \qquad \text{Eq. 2.33}$$

The average precipitation above the forest over each event was assumed to be homogeneous in space and only a function of angle $\left(\overline{P \uparrow_{i,j}} \rightarrow \overline{P \uparrow_i}\right)$, such that Eq. 2.33 becomes:

$$\overline{\mathrm{F}_j} = \int_i \overline{P \uparrow_i} \cdot \overline{T^*_{i,j}}\, di \qquad \text{Eq. 2.34}$$

Snow particles do not interact with a forest canopy as light does; they drift, rebound on impact, and on occasion adhere to (are intercepted by) the canopy, resulting in generally different absorption characteristics between light and snow. To estimate the mean snowfall transmittance $\overline{T^*_{i,j}}$ along the given ray (i, j), the model for light transmittance (Eq. 1.15) was adapted to:

$$\overline{T^*_{i,j}} = e^{-\omega^* \chi_{i,j}} \qquad \text{Eq. 2.35}$$

where $\chi_{i,j}$ is the contact number along ray (i, j) and ω^* is the contact absorption coefficient for snow particles, related to the transmittance probability given a single particle-canopy collision by $p^*_t = e^{-\omega^*}$ and corresponding interception (a.k.a. absorption) probability $p^*_a = 1 - p^*_t$. The light transmittance analogue model assumes that ω^* is constant with angle and that the snow particle trajectories for a given event are linear in space. Next it is assumed that the relative contribution of snowfall across angles follows a Gaussian distribution, where the estimate of mean above-canopy snowfall rate $\overline{P \uparrow_i}$ for a given angle i is represented by:

$$\overline{P \uparrow_i} = c_n \cdot \overline{P \uparrow}\, e^{\frac{-\sigma^2 \cdot r_i^2}{2}} \qquad \text{Eq. 2.36}$$

where σ [°] is the standard deviation of the Gaussian distribution, c_n is a normalization constant, and r_i is the central angle between a given angle (ϕ_i, θ_i) and the angle of maximal above-canopy snowfall over the hemisphere (ϕ_{max}, θ_{max}), calculated by:

$$r_i = arccos[cos(\phi_{max})cos(\phi_i) + sin(\phi_{max})sin(\phi_i)cos(\theta_{max} - \theta_i)] \qquad \text{Eq. 2.37}$$

Substituting Eq. 2.36 into Eq. 2.34 yields an estimate of throughfall as:

$$\overline{F_j} = c_n \cdot \overline{P \uparrow} \int_i e^{\frac{-\sigma^2 \cdot r_i^2}{2}} e^{-\omega^* \chi_{i,j}}\, di \qquad \text{Eq. 2.38}$$

Calculating this integral for discrete samples of contact number over the hemisphere and multiplying by the length of the time interval results in the discrete sum:

$$\overline{F_j}\Delta t = c_n \cdot \overline{P \Uparrow} \, \Delta t \sum_i e^{\frac{-\sigma^2 \cdot r_i^2}{2}} e^{-\omega^* \chi_{i,j}} \qquad \text{Eq. 2.39}$$

2.6 Conclusions

This chapter presents the methods used to collect, process, and analyze observations of snowpack depth and density, and to produce a suite of canopy metrics. In several cases, multiple methods to estimate similar quantities were outlined using different sets of assumptions: areal snow depth distributions were calculated using three different interpolation schemes; and synthetic hemispheres and subsequent light transmittance metrics were generated using both lidar point cloud reprojection and voxel ray sampling of lidar methods. Chapter 3 takes a close look at the sensitivities of results to methodology by comparing results from parallel methods in pursuit of Objective 1, to inform their appropriate application for addressing Objective 2.

Chapter 3: Assessing the effects of beam occlusion on UAV lidar observations of snow and vegetation in forests

3.1 Introduction

Airborne lidar observations collected over vegetated environments yield spatially nonuniform samples of vegetation and subcanopy ground and snow surfaces due to the occlusion of lidar beams by vegetation (Harding et al., 2001; Chasmer et al., 2006). While the physical basis of beam occlusion is fairly well understood, ramifications for analysis are nontrivial and can vary from negligible to significant depending on physical factors (including optical transmittance and reflectance of vegetation, size of vegetation elements, sensor sensitivity, and lidar beam wavelength, power and footprint) and data collection and analysis factors (including point densities, discrete return classification schemes, surface interpolation methods, and vegetation density calculation methods) (Béland et al., 2019). In this chapter the effects and implications of nonuniform sampling due to lidar beam occlusion on areal snow depth statistics and vegetation density and light transmittance metrics are examined for the UAV lidar observations, study site, and methodologies specific to this study.

Occlusion of the subcanopy surface from airborne sensors by vegetation is not spatially homogenous because vegetation densities between the ground surface and the sensor are not spatially homogenous (Harding et al., 2001). Complete obstruction of the lidar beam by vegetation for a given sample results in no information about the elevation of the subcanopy surface, and is more common for small footprint lidar beams typical of UAV lidar platforms (Béland et al., 2019). The general result is a covariance of surface point density with vegetation density. This can be problematic when surface elevations also covary significantly with vegetation density, as is common for snow surfaces (Sturm, 1992), potentially resulting in bias of mean areal surface elevations. Methods which omit analysis over data-poor regions can amplify these effects (Harpold et al., 2014; Broxton et al., 2015). Alternatively, resampling surface measurements has the potential to reduce bias in areal estimates without explicitly characterizing the covariances, if care is taken to ensure that unobserved regions are represented accurately and proportionately.

Linear interpolation of surface points by Delaunay triangulation is a common method for resampling surface observations to represent an area of interest (Isenburg, 2020). This is an effective method for representing data gaps when local extrema are included in the set of observations but can perpetuate bias when local extrema are systematically omitted from observations (i.e., where extrapolation is needed). Limiting interpolation distances allows for some compromise between areal coverage and systematic interpolation bias. More elaborate methods such as rejection sampling and importance sampling, where points are either systematically dropped or weighted to account for sample bias, can be used to explicitly evaluate and correct for sample bias.

Dense vegetation does not only occlude the ground from airborne sensors; it also occludes itself. The attenuation of lidar beam energy with distance through vegetation is often considered analogous to the exponential attenuation of radiation through a solution as modeled by the Beer-Lambert law (Solberg et al., 2006). By this model, reflected waveforms from upper (or proximal) vegetation carry generally greater energy than those from equivalent understory (or distal) vegetation (Harding et al., 2001). For discrete return lidar, this results in a higher probability of understory vegetation reflections with intensities below the return threshold compared with those from the upper canopy (Alonzo et al., 2015), such that the lower layers of canopy are commonly under-represented in discrete return lidar point clouds compared with upper layers. This effect varies spatially with vegetation structure, and its handling is complicated by the absence of Null values in return point cloud data such that the absence of returns in a region is ambiguous between unsampled space and sampled but empty space. As a result, canopy metrics calculated directly from return point clouds may systematically underestimate contributions from the lower canopy (Webster et al., 2020), with the significance of such errors depending on the metrics, methods, instruments, scanning patterns, and vegetation being considered. Ray tracing of lidar is one method to account for the effects of nonuniform lidar sampling across vegetation layers (Béland et al., 2011), such that returns can be considered within the context of spatial sampling patterns.

3.2 Methods

The significance of the effects of beam occlusion on areal snow depth distributions was assessed by comparing results from different resampling methods. Snow depth distributions were calculated over the forest and clearing plots from 5 cm resolution snow depth maps (HS_{lidar}) generated for each of the three survey days within the study period using three separate methods: 1) full interpolation of the snow surface, 2) limited interpolation (see section 2.3.1) of the snow surface up to a maximum horizontal distance of 10 cm, and 3) limited interpolation with rejection sampling by LPM-L (see section 2.3.4). The means of the full interpolation and limited interpolation distributions were tested for equivalence with those of the rejection sampled distribution for each respective day and plot using Student's t-test ($\alpha = 0.05$), and variances were compared using Levene's test ($\alpha = 0.05$). Distribution means and variances were reported relative to those of the corresponding rejection sampled values. Snow depth distributions were also compared visually.

The significance of the effects of nonuniform sampling of vegetation on canopy metrics was assessed by comparing snow-off canopy metrics calculated over the forest plot using both resampling and non-resampling methods. The effects of nonuniform sampling on vegetation return heights [m AGS] were assessed by comparing means of the return height distributions between the lidar return point cloud and the resampled point cloud generated from voxel ray sampling of lidar (see Section 2.4.2) using Student's t-test ($\alpha = 0.05$). Variances of return heights were compared between methods with Levene's test ($\alpha = 0.05$). Means of light transmittance

over 15° zenith-angle bands were calculated from synthetic hemispheres from lidar point cloud reprojection (Section 2.4.1) and voxel ray sampling of lidar (Section 2.4.2), and root mean squared errors (RMSE) with corresponding georeferenced hemispherical photography were calculated and compared between methods. Canopy height, light transmittance, contact number, and LAI_{2000} distributions were also compared visually between methods.

3.3 Results

Spatial coverage of 5 cm resolution snow depth (HS_{lidar}) products from limited interpolation ranged from 46.0% to 66.2% within the forest plot, and from 82.1% to 85.4% within the clearing plot, across days. Rejection sampling by LPM-L resulted in total acceptance rates ranging from 28.6% to 34.8% of limited interpolation samples within the forest and 20.5% to 22.6% within the clearing, with resulting sample counts exceeding 1.02 x 10^5 within the forest and 1.62 x 10^5 within the clearing for all days.

Table 3.1: Snow depth (HS_{lidar}) means (a) and standard deviations (b) for areal distributions over the forest and clearing plots and for all three survey days, calculated using rejection sampling, full interpolation, and limited interpolation methods.

a)

Date	Snow depth means μ [m]					
	Forest plot			Clearing plot		
	rejection sampling	full interpolation	limited interpolation	rejection sampling	full interpolation	limited interpolation
2019-02-14	0.235	0.243	0.266	0.598	0.611	0.639
2019-02-19	0.254	0.262	0.286	0.632	0.642	0.672
2019-02-21	0.334	0.331	0.371	0.745	0.749	0.777

b)

Date	Snow depth standard deviations σ [m]					
	Forest plot			Clearing plot		
	rejection sampling	full interpolation	limited interpolation	rejection sampling	full interpolation	limited interpolation
2019-02-14	0.103	0.112	0.113	0.136	0.145	0.117
2019-02-19	0.109	0.118	0.119	0.135	0.148	0.121
2019-02-21	0.121	0.126	0.133	0.135	0.145	0.121

Means of lidar snow depth (HS_{lidar}) calculated using full interpolation and limited interpolation were significantly different from those of the corresponding rejection sampling method for both plots, for all days (p-values < .001). Within the forest, means of HS_{lidar} calculated from full interpolation were between 99.2% - 103.4% of means from the rejection sampled distributions, while those from limited interpolation were between 111.2% - 113.4% of means from the rejection sampled distributions, across days (Table 3.1.a). Similarly, variances of HS_{lidar} calculated using full interpolation and limited interpolation were significantly different from

those of the corresponding rejection sampling method for both plots, for all days (p-values < .001). Standard deviations of HS_{lidar} within the forest ranged between 103.8% - 108.7% and 109.1% - 109.5% of rejection sampled standard deviations for the full interpolation and limited interpolation distributions, respectively (Table 3.1.b). Within the clearing, distribution means from full interpolation were between 100.5% - 102.2% of those from the rejection sampled distributions, and between 104.3% - 106.9% for the limited interpolation distributions. Distribution standard deviations within the clearing ranged from 106.7% - 110.2% and 86.4% - 89.9% of rejection sampled standard deviations for the full interpolation and limited interpolation distributions, respectively.

Upon visual comparison, the maximum relative frequencies of the rejection sampled distributions were consistently greater than those of the other two methods within the forest, and consistently less within the clearing, across all days (Figure 3.1.a-b). Additionally, consistent artifacts were seen in snow depth distributions from full and limited interpolation methods that were not found in rejection sampled. Within the forest, full and limited interpolation products yielded snow depth distributions with heavier tails than were seen in distributions from rejection sampling (Figure 3.1.a). Within the clearing, three local peaks in relative frequency distributions were consistently present among full and limited interpolation products, contrasting single maxima among corresponding rejection sampled distributions (Figure 3.1.b). A comparison of laser penetration (LPM-L) distributions for observed pixels compared with all pixels showed that limited interpolation snow depth products were biased away from pixels with lower laser penetration in both the forest and clearing plots (Figure 3.1.c-d).

The observed point cloud underrepresents the density of lower canopy relative to upper canopy due to lidar beam occlusion, compared with the resampled point cloud. Figure 3.2 shows normalized frequency distributions of canopy return heights [m AGS] for the observed ($n = 4.69 \times 10^6$) and resampled ($n = 3.23 \times 10^6$) point clouds. Means and variances differed significantly between the two methods (p-values < .001), with observed point cloud yielding 115.7% of the resampled mean (10.7 m compared with 9.26 m) and 115.2% of the resampled variance (23.2 m compared with 20.2 m). Visual comparison shows observed point heights skewed toward higher elevations above the ground compared with the resampled point heights.

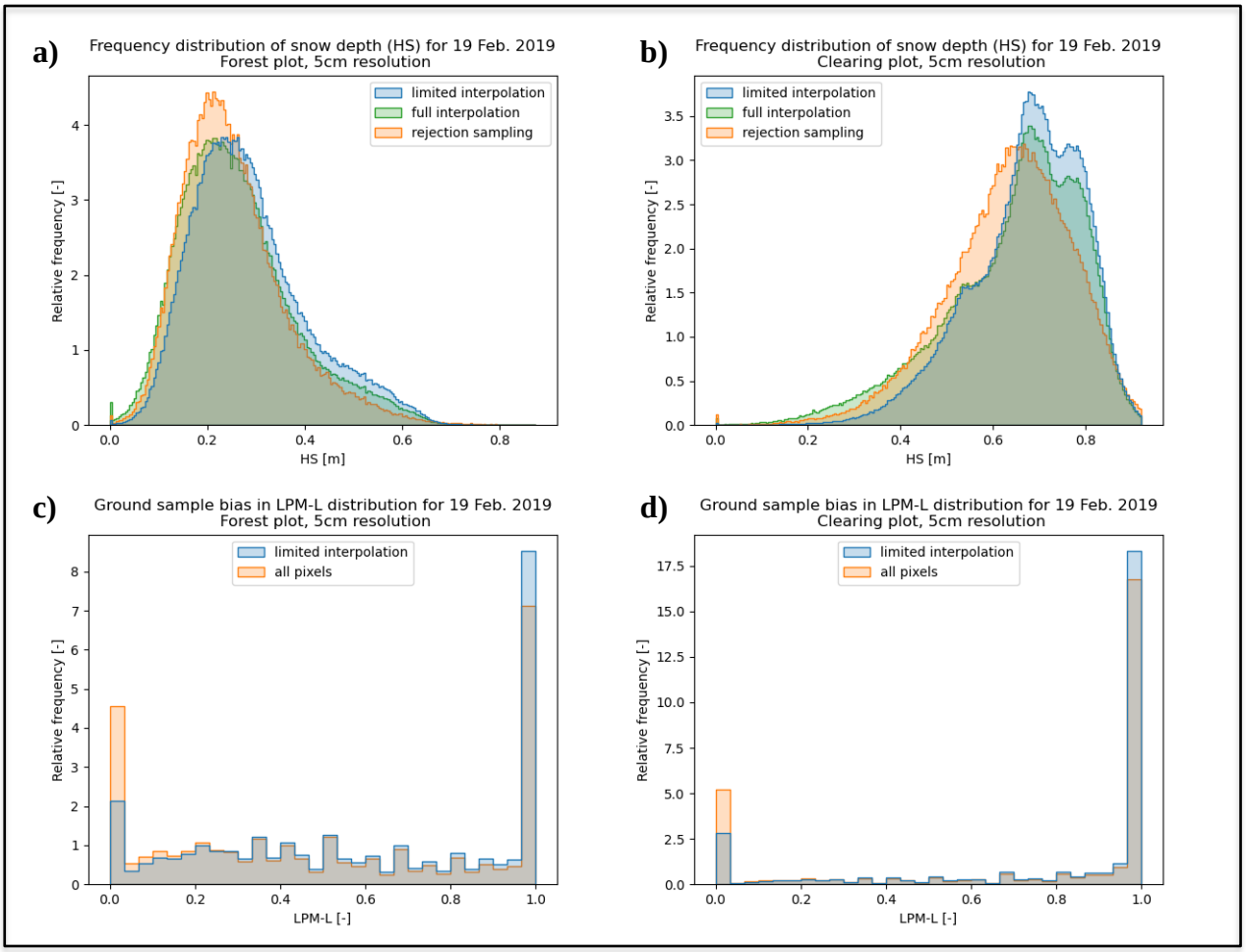

Figure 3.1: Histograms of the lidar snow depth (HS_{lidar}) distributions within the forest (a) and clearing (b) plots for 19 Feb. 2019 using three resampling methods: limited interpolation (blue), full interpolation (green), and rejection sampling after limited interpolation (orange). Relative frequency distributions of laser penetration metric LPM-L over the forest (c) and clearing (d) plots, for all pixels (orange) and for the extent of the limited interpolation HS_{lidar} estimates for 19 Feb. 2019 (blue).

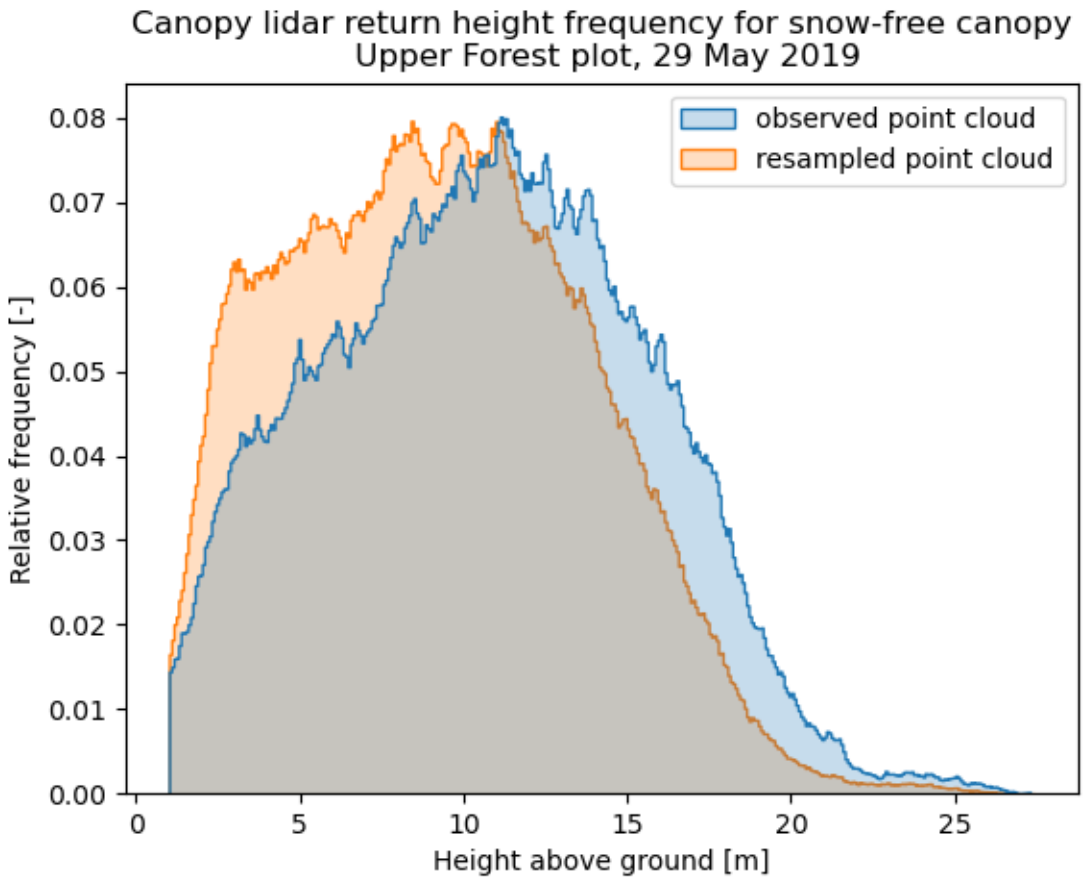

Figure 3.2: Normalized frequency distribution of canopy return height [m AGS] over the forest plot using the observed lidar point cloud (blue) and a resampled point cloud (orange) generated from voxel ray sampling of lidar.

Differences in assumptions of the two synthetic hemisphere methods resulted in visible differences among outputs (Figure 3.3), with different systematic biases when compared with light transmittance estimated by thresholded hemispherical photography. Light transmittance of synthetic hemispheres over all four 15° zenith angle bands and weighted by solid angle showed lower root mean squared error (WRMSE) with light transmittance from thresholded hemispherical photography for synthetic hemispheres from point reprojection (weighted WRMSE = 0.0444, n = 15) compared with those from ray sampling (WRMSE = 0.0663, n = 15). Root mean squared error (RMSE) values for each 15° zenith angle band were also lower for point reprojection outputs compared with ray sampling outputs (Table 3.2). Light transmittance derived from synthetic hemispheres calculated over a 1 m square grid over the forest plot showed different patterns of agreement and discrepancy between synthetic hemisphere methods depending on zenith angle (Figure 3.4.a). Furthermore, while light transmittance metrics showed minimal visual bias between methods, bias between contact number estimates was visually apparent (Figure 3.4.b) and carried over into LAI_{2000} estimates (Figure 3.4.c).

Table 3.2: Root mean squared error (RMSE) of band-wise light transmittance estimated from lidar point cloud reprojection ($T_{a\text{-}b}^{\bullet}$) and from voxel ray sampling of lidar ($T_{a\text{-}b}^{\blacktriangle}$), compared with corresponding values from thresholded hemispherical photography of the snow-off canopy (n=15).

Zenith angle band (a°-b°)	RMSE of light transmittance from point cloud reprojection ($T_{a\text{-}b}^{\bullet}$) [-]	RMSE of light transmittance from voxel ray sampling ($T_{a\text{-}b}^{\blacktriangle}$) [-]
0° - 15°	0.0809	0.120
15° - 30°	0.0483	0.0746
30° - 45°	0.0477	0.0591
45° - 60°	0.0286	0.0533

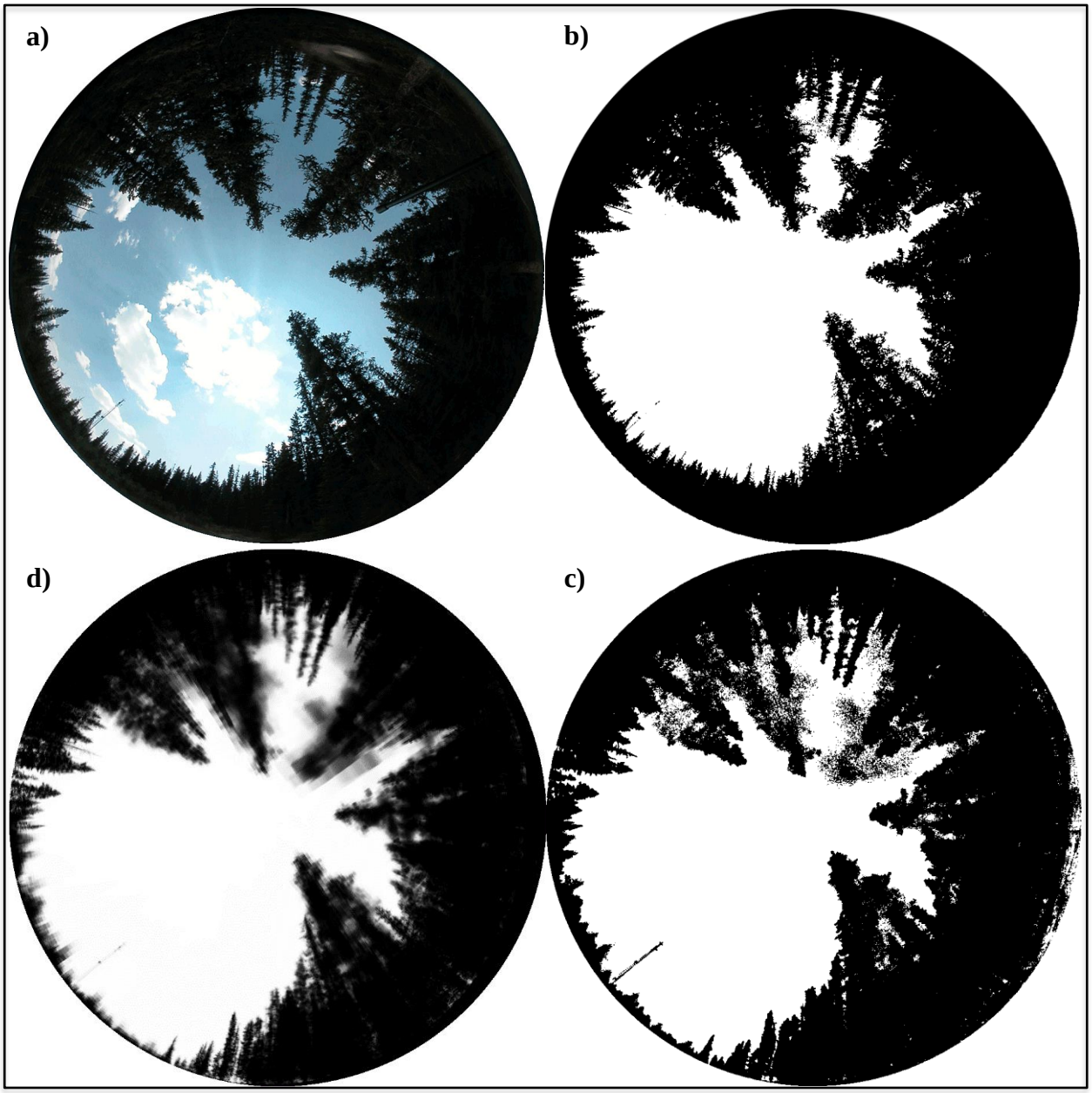

Figure 3.3: Clockwise from top left: a) Hemispherical photograph which is subsequently thresholded (b) to differentiate canopy and sky pixels for estimating transmittances and contact numbers over zenith angle bands. c) A respective synthetic hemispherical image generated from reprojection of the lidar point cloud. d) Respective light transmittance estimates along hemispherical rays calculated by voxel ray sampling of lidar. All hemispherical images are shown from the upward-facing perspective, with north to the top and east to the left.

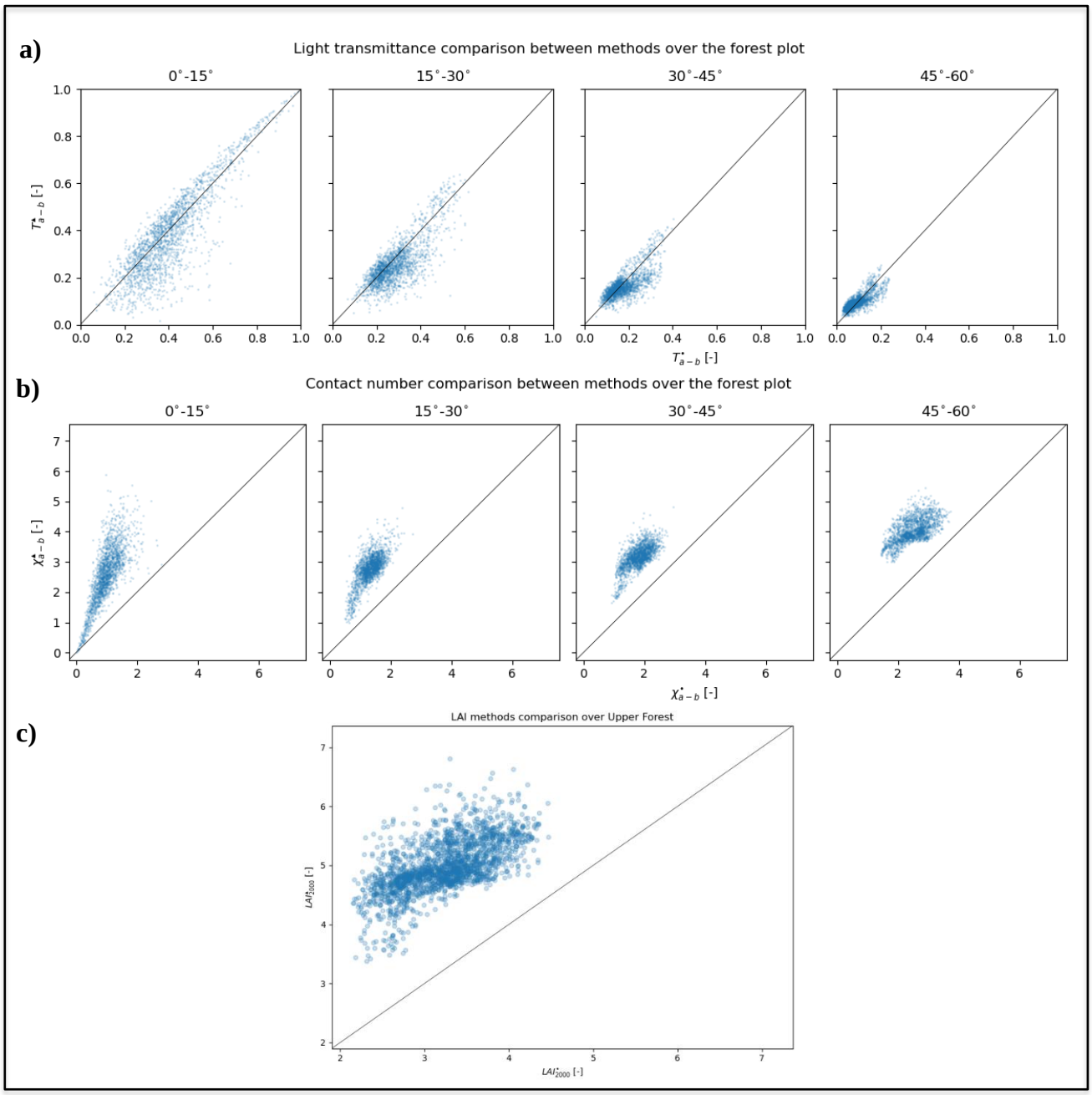

Figure 3.4: Comparisons of (a) light transmittance and (b) contact number estimates from synthetic hemispheres generated by lidar point cloud reprojection (x-axis) with those from voxel ray sampling of lidar (y-axis) for each of the four zenith angle analysis rings, with 1-to-1 line. (c) Comparison of leaf area index (LAI_{2000}) between the two methods, with 1-to-1 line. Synthetic hemispheres used in analysis were generated over a 1 m square grid of the forest plot (n = 1944).

3.4 Discussion

3.4.1 Effects of sample bias with vegetation on areal snow depth distributions

Significant differences in areal snow depth distributions were observed between the three methods which are attributed to beam occlusion by vegetation. Mean snow depths from full interpolation showed better agreement with those rejection sampled in all cases compared with those from limited interpolation (Table 3.1.a). Standard deviations of snow depths from both full and limited interpolation methods showed consistent systematic bias compared with those from rejection sampling, however (Table 3.1.b). Additionally, complementary artifacts were seen in snow depth distributions from full and limited interpolation methods that were not found in rejection sampled distributions which are attributed to bias with vegetation density (Figure 3.1a-b). While full interpolation may be appropriate for estimating areal snow depth means, neither interpolation method is recommended for estimating standard deviations or other distribution statistics when covariance between snow depth and vegetation density is observed.

Areal snow depth distributions estimated by full and limited interpolation – which both assume random lidar sampling of subcanopy surfaces – consistently differed from those estimated by rejection sampling which implicitly corrects for sample bias with vegetation density (Figure 3.1.a-b). If lidar beam occlusion by vegetation were negligible, or if there were no significant covariance between snow depth and vegetation density, gridded sampling of snow depth would be effectively random, and therefore all three methods would yield qualitatively and quantitatively similar results. The statistically significant and visually apparent differences between distributions among the three methods supports the contrapositive: both that beam occlusion is not negligible *and* that snow depths covary significantly with vegetation density, resulting in systematic bias for methods which rely on random lidar sampling of subcanopy snow depths. These findings challenge the assumption of random sampling when characterizing areal snow depth distributions below vegetation from UAV lidar and support the implicit or explicit handling of sample bias due to beam occlusion by vegetation to improve areal estimates. A discussion of the possible mechanisms for these biases follows.

The observed overestimation of areal mean snow depths calculated by limited interpolation relative to rejection sampled values was consistent with the areal underrepresentation of densely vegetated pixels seen in Figure 3.1.c-d due to lidar beam occlusion, which resulted in the omission of ground points in regions of generally shallower snowpack. This was reinforced by the observed reduction of areal mean errors when considering the full interpolation estimates, such that regions of dense vegetation were proportionately represented. As the full and limited interpolation snow depth models only differed among cells which require interpolation beyond 10 cm, this is equivalent to stating that full interpolation results in greater accuracy than simply padding cells beyond the 10 cm interpolation length with the mean observed values when estimating snow depth means in these regions. While fully interpolated areal means were found

to differ significantly from the corresponding rejection sampled values, observed relative errors within 3.4% in both the forest and clearing were within GPS base station error margins of this study and therefore may be functionally as accurate.

Despite yielding smaller errors in mean snow depth estimates, however, distributions from full interpolation consistently shared artifacts with limited interpolation that were not seen in the rejection sampled distributions. This was qualitatively observed in the histograms of snow depths within the clearing (Figure 3.1.b) as the three localized peaks which were not seen in the rejection sampled output, and to a lesser extent in the heavy tails at greater snow depths seen within the forest (Figure 3.1.a). Quantitatively, areal estimates of snow depth standard deviations were consistently higher for full interpolation products than for rejection sampling products in both the forest and clearing (Table 3.1.b). This was due in part to a higher occurrence of extreme values – both high and low – returned by interpolating snow surfaces over distances beyond 10 cm, inflating the set standard deviation relative to the rejection sampled distributions while having limited effects on the means (Table 3.1.a).

Limited interpolation also yielded higher areal snow depth standard deviations within the forest, but lower standard deviations within the clearing, relative to rejection sampling (Table 3.1.b). This was explained by the differences in the skewness of the distributions observed between the two plots (Figure 3.1.a-b). Due to the prevalence of thin snowpacks within the forest, over-representation of deep snowpacks shifted values *away* from the distribution means, yielding greater standard deviation. Within the clearing, however, the corresponding prevalence of deep snowpacks meant that over-representation shifted values *closer* to the distribution means, reducing the standard deviation of the set relative to the rejection sampled values.

The effects of rejection sampling are sensitive to length scales of analysis. While sample bias with vegetation was evident at 5 cm resolution due to discrepancies between rejection sampling and limited interpolation outputs, increasing raster cells to 1 m resulted in no unobserved pixels, no difference between target and sample distributions for rejection sampling, and therefore no evidence of sample bias despite using the same observations (results not shown). It is critical therefore to conduct rejection sampling at or below the length scales of variation of snow depth, as any sample bias below the raster resolution will be masked by rasterization.

Of the three methods considered for areal snow depth estimates in this study, rejection sampling was assumed to provide the best estimates of the areal snow depth distributions, but systematic differences between rejection sampled and actual snow depth distributions are possible. For example, metrics used as target distributions for rejection sampling (LPM-L in this study) may not fully parameterize the covariance of sampling with snow depth. Despite this, partial parameterizations nonetheless reduce the sample bias compared with the uncorrected limited interpolation distributions. Significant differences between rejection sampled and interpolated

areal distributions are therefore sufficient to demonstrate the significance of the effects of lidar beam occlusion on areal snow depth estimates despite the potential for residual differences between rejection sampled and true snow depth distributions. Further rejection sampling by additional metrics could be considered to make sample bias assessment and correction more robust, if a single metric is determined to be insufficient to characterize the sample bias. While rejection sampling of UAV lidar snow depths may not address all sample bias issues, it is a tool which complements traditional snow survey techniques which are generally more labour intensive for a given number of samples, more destructive of the snowpack, and often also subject to mechanisms for sample bias with dense vegetation.

3.4.2 Sources of error in estimating canopy metrics

Vegetation densities calculated from UAV lidar return densities were over-estimated for the upper canopy relative to understory vegetation across the forest plot (Figure 3.2). The consistent above-canopy perspective of the UAV lidar sensor resulted in significant positive bias in estimates of vegetation height above ground from the observed point cloud compared with estimates resampled estimates from voxel ray sampling of lidar. This was consistent with previous observations of airborne lidar beam occlusion where vegetation beyond the most proximal layer of vegetation to the sensor was systematically undersampled (Hopkinson and Chasmer, 2009; Béland et al., 2019). Resampling methods such as voxel ray sampling of lidar should therefore be applied in combination with the UAV lidar sampling and when analyses require comparison of derived vegetation densities among different heights within the canopy, to avoid systematic bias due to beam occlusion.

Light transmittance estimates from synthetic hemispheres generated by point cloud reprojection showed better agreement with validating thesholded hemispherical photography across all angle bands than did estimates from synthetic hemispheres generated by voxel ray sampling of lidar (Table 3.2). Additionally, despite minimal bias of light transmittance estimates between the two synthetic hemisphere methods, visually apparent bias between subsequent contact number estimates were seen and resulted in similar discrepancies between LAI_{2000} estimates by the two methods (Figure 3.4). These results were unexpected and suggested that nonuniform sampling may not be the only (or even primary) source of differences in transmittance metrics between the two synthetic hemisphere methods. Further analysis led to the identification of two assumptions (Eq. 3.1 and Eq. 3.2) used in analysis of the binary synthetic hemispheres from point reprojection *and* thresholded hemispherical photography used for validation, which explain the observed discrepancies between methods (see Appendix E). These findings highlight some limitations of the utility of thresholded hemispherical photography for validation of light transmittance estimates. While this does not immediately inform the significance of lidar beam occlusion on light transmittance estimates, these findings provide insights into the strengths and limitations of each method with important implications for their applications to characterizing snow vegetation relationships. These two assumptions and the potential for associated errors are discussed below.

In analysis of both thresholded hemispherical photography and synthetic hemispheres from lidar point cloud reprojection, mean zenith-angle band-wise transmittances $\mathrm{T}_{a-b} = E[T]_{a-b}$ are estimated by the mean values of the thresholded hemispherical transmittance:

$$\mathrm{T}_{a-b} \cong T^{\dagger}_{a-b} = E[H(T - T')]_{a-b} \qquad \text{Eq. 3.1}$$

where $E[x]_{a-b}$ denotes the arithmetic mean of a variable *x* over the region of hemisphere within zenith angles a° - b°, and $H(x - x')$ is the unit step (or "threshold") function centered at x'. For a given distribution of *T* within a° - b° there is a unique threshold $T'_{=}$ such that the approximation $T_{a-b} \cong T^{\dagger}_{a-b}$ is explicitly equal. Mean band-wise transmittance $E[T]_{a-b}$ is not known a priori, however, and so direct observation of $T'_{=}$ is generally not possible. Instead, a threshold value *T'* is commonly selected to minimize error in sky-canopy binary classification under the assumption that all canopy pixels correspond to transmittances of *T* = 0 (e.g., Ridler & Calvard, 1978; Nobis & Hunziker, 2005). The validity of the threshold assumption (Eq. 3.1) depends on agreement between *T'* and $T'_{=}$ which may be sensitive or insensitive to discrepancy depending on the images and transmittance regimes of the canopy. Resulting discrepancies between $T^{\dagger}_{a-b}$ and T_{a-b} are carried over into estimates of band-wise contact number and leaf area index (see Figure E.3).

Analysis of binary images from thresholded hemispherical photography and point cloud reprojection also relies on estimating mean zenith-angle band-wise contact numbers $\chi_{a-b} = E[-ln(T)]_{a-b}$ by:

$$\chi_{a-b} \cong \chi^{\dagger}_{a-b} = -ln(E[T]_{a-b}) \qquad \text{Eq. 3.2}$$

This approximation assumes that the two operations $E[x]_{a-b}$ and $-ln(x)$ are commutative, which is only explicitly true for singular (i.e., Dirac delta) distributions of *T* within a given angle band. For non-singular distributions of *T*, this assumption results in $\chi_{a-b} > \chi^{\dagger}_{a-b}$ due to the convexity of the $-ln(x)$ function (see Figure E.4).

Both the threshold (Eq. 3.1) and commutation (Eq. 3.2) assumptions are used in analyses of hemispherical photos and lidar point cloud reprojection. Point cloud reprojection results in binary synthetic hemispherical images and requires band-wise means to arrive at nonbinary values of light transmittance over the interval [0, 1]. As light transmittance analysis of hemispherical photography also relies on these two assumptions, resulting biases may be matched in the validation of reprojection estimates. In contrast, voxel ray sampling of lidar is a contact number model and does not rely on thresholding or band-wise means to arrive at estimates of light transmittance or contact number. This may explain the unexpected smaller errors observed for reprojection contact number estimates than for ray sampling estimates when

compared with validating photography (Table 3.2). Comparison of $\chi_{a-b}^{\dagger}$ values calculated from thresholded synthetic hemispheres from ray sampling with the corresponding known χ_{a-b} values from ray sampling (Figure E.5) showed consistent patterns of discrepancy with those observed in Figure 3.4, supporting the argument that the discrepancies seen in Figure 3.4 are primarily due to errors from the threshold and commutation assumptions. Further comparison of $\chi_{a-b}^{\dagger}$ from ray sampling with $\chi_{a-b}^{\bullet}$ from reprojection showed better agreement, with errors from the two assumptions represented in both point cloud reprojection and ray sample metrics (see Figure E.6).

While there is evidence of bias in mean vegetation height estimates from return point clouds due to lidar beam occlusion, the effects on light transmittance estimates are somewhat opaque. In a horizontally homogenous forest, light transmittances derived from the integration of return point densities through all layers of the canopy should yield relatively accurate estimates across angles despite the potential for under-representation of understory vegetation. Introducing spatial variation in vegetation density results in spatial variation in sampling of lower vegetation, and underrepresentation of lower canopy layers may result in relative errors in transmittance in space, and across angles. This can be circumstantially observed in the comparison of individual synthetic hemispheres across methods (e.g., Figure 3.3) where transmittances from reprojection both underestimate and overestimate transmittance in various regions due to nonuniform sampling. It is expected therefore that transmittance from point cloud reprojection should result in more bias from beam occlusion in regions with greater spatial variation in vegetation density, such as in sparse forests or near clearing edges. Further work is required to fully explain the differences observed between methods, to quantify the effects of nonuniform sampling on light transmittance estimates.

If there were no significant covariance between vegetation and lidar sampling densities, spatial variations in observed point cloud density should be representative of vegetation densities and both observational and resampling methods should yield qualitatively and quantitatively similar vegetation height distributions. The divergence of canopy height distributions between observational and resampling methods therefore supports the contrapositive: that there is significant covariance between vegetation and lidar sampling densities due to non-random sampling of vegetation with height, resulting in point cloud densities which are not spatially representative of vegetation densities. While the explicit effects of lidar beam occlusion on transmittance estimates are unclear, significant effects can be anticipated in forests and at scales where there is significant horizontal variation in vegetation density. Resampling methods which account for nonuniform sampling due to beam occlusion should be considered when analysis requires comparison of vegetation densities across heights, or when light transmittance analysis is conducted across a forest with substantial spatial heterogeneity.

3.5 Conclusions

Effects of lidar beam occlusion were evident in the analysis of branch-scale snow depth and canopy density metrics calculated from the UAV lidar observations of this study site. Significant differences in areal subcanopy snow depth distributions were observed between interpolated and rejection-sampled products, suggesting the potential for bias in areal snow depth statistics if resampling methods are not used. Significant bias in mean vegetation height calculated from the UAV lidar return point cloud was also observed due to systematic occlusion and underrepresentation of understory vegetation compared with the canopy crown. Light transmittance estimated by voxel ray sampling of lidar showed more error with validating thresholded photography than did similar estimates from lidar point cloud reprojection. These findings may be confounded by two methodological assumptions – thresholding and commutation – which are utilized in analysis of both the reprojection products and thresholded hemispherical photography used for validation. Greater discrepancies between lidar point reprojection products and hemispherical photography are nonetheless anticipated in regions of greater spatial heterogeneity in vegetation density. These findings demonstrate significant effects of lidar beam occlusion by vegetation on branch-scale observations of snow and vegetation for the instruments, methods, and site considered in this study, with more research needed to understand the effects on light transmittance estimates.

Resampling methods were indicated for areal snow depth statistics and vegetation height metrics. Rejection sampling was therefore implemented to reduce bias in areal statistics of snow depth, SWE, dSWE for spatial analysis in Chapter 4. Furthermore, mean canopy height (MCH) was calculated from the resampled point cloud, rather than directly from the lidar point cloud of canopy returns. Note that canopy crown height (CHM) was still calculated from the return point cloud as occlusion was expected to be minimal for the upper-most layer of vegetation. Due to the ambiguity of the effects of lidar beam occlusion on light transmittance metrics, all transmittance metrics were estimated using both point cloud reprojection and voxel ray sampling of lidar for subsequent analysis in Chapter 4.

Chapter 4: Relating spatial patterns of snow accumulation to branch-scale canopy structure

4.1 Introduction

Canopy structure is one of the most important factors determining spatial variation of snow accumulation in forests, but the physical processes that drive spatial relationships between canopy structure and snow accumulation are not fully understood. Substantial differences among snow accumulation model assumptions persists despite extensive validation of individual models. Further model development stands to benefit from observations of snow accumulation and canopy structure, made at the scale of branches and collected over the extent of forest stands, over a variety of conditions. To this end, this study uses observations from UAV lidar in combination with manual snow surveys and hemispherical photography to relate patterns of snow accumulation to branch scale patterns of needleleaf canopy structure over a forest stand, for two mid-winder storms in the Canadian Rockies.

4.2 Methods

4.2.1 Describing spatial distributions of snow and canopy metrics

Descriptive statistics of high-resolution subcanopy snow products were calculated for comparison between the forest and canopy plots, as well as with other values reported in the literature. Spatial distributions of SWE and ΔSWE distributions within the forest and clearing plots were estimated from corresponding 5 cm-resolution products using rejection sampling according to the LPM-L metric. SWE_f distributions within the forest plot from each day of measurement were fitted to lognormal distributions following (Shook and Gray, 1997), and the means (μ) and standard deviations (σ) were calculated. Means and coefficients of variation (c_v) were reported for both the forest and clearing snowpacks for each day. Means and standard deviations of rejection-sampled ΔSWE estimates were reported for each plot and storm event.

Areal statistics of a suite of canopy metrics (Table 4.1) were calculated over the forest plot to describe the general structure of the forest for comparison with values reported in the literature, to compare values between methods, and to consider the effects of intercepted snow on canopy structure. Canopy metrics were calculated for “snow-on” or “snow-off” canopy conditions (and in some cases both). Mean, median, and maximum values of canopy metrics were calculated, as were median values of metrics for the subset of canopy pixels (CHM ≥ 1 m). Canopy metric values were not reported for the clearing plot.

Table 4.1: Canopy metrics calculated over the forest plot for spatial analysis with SWE and ΔSWE estimates, and the canopy conditions and methodology sources used for their calculation.

Symbol	Metric	Canopy Cond.	Method
CHM	Canopy crown height [m AGS]	snow-off	Section 2.4.3 (Khosravipour et al., 2016)
DNT	Distance to nearest tree [m]	snow-off	Section 2.4.3
DCE	Distance to canopy edge [m]	snow-off	Section 2.4.3 (Mazzotti et al., 2019)
MCH	Mean canopy height [m AGS]	snow-off	Section 2.4.3
fCov	Fractional canopy cover [-]	snow-off	Section 2.4.3 (Varhola and Coops, 2013)
LPM-L	Laser penetration metric [-] considering first and last returns	snow-off	Eq. 2.7 (Alonzo et al., 2015)
MDC	Mean distance to canopy [m]	snow-off	Eq. 2.20 (Moeser, Morsdorf, et al., 2015)
TGA	Total gap area [m^2]	snow-off	Eq. 2.21 (Moeser, Morsdorf, et al., 2015)
$T_1^{\triangle}$	1° (vertical) light transmittance [-]	snow-on	Voxel ray sampling, Section 2.4.2
$T_1^{\blacktriangle}$	1° (vertical) light transmittance [-]	snow-off	Voxel ray sampling, Section 2.4.2
$T_{15}^{\triangle}$	15° light transmittance [-]	snow-on	Voxel ray sampling, Section 2.4.2
$T_{15}^{\blacktriangle}$	15° light transmittance [-]	snow-off	Voxel ray sampling, Section 2.4.2
$T_{15}^{\bullet}$	15° light transmittance [-]	snow-off	Point reprojection, Section 2.4.1
$T_{15\text{-}30}^{\triangle}$	15°-30° light transmittance [-]	snow-on	Voxel ray sampling, Section 2.4.2
$T_{15\text{-}30}^{\blacktriangle}$	15°-30° light transmittance [-]	snow-off	Voxel ray sampling, Section 2.4.2
$T_{15\text{-}30}^{\bullet}$	15°-30° light transmittance [-]	snow-off	Point reprojection, Section 2.4.1
$LAI_{60}^{\triangle}$	60° leaf area index [-]	snow-on	Voxel ray sampling, Section 2.4.2
$LAI_{60}^{\blacktriangle}$	60° leaf area index [-]	snow-off	Voxel ray sampling, Section 2.4.2
$LAI_{2000}^{\bullet}$	60° Li-Cor LAI-2000 (4 bands) [-]	snow-off	Point reprojection, Section 2.4.1
$C_c^{\triangle}$	Canopy closure [-]	snow-on	Voxel ray sampling, Section 2.4.2
$C_c^{\blacktriangle}$	Canopy closure [-]	snow-off	Voxel ray sampling, Section 2.4.2
$C_c^{\bullet}$	Canopy closure [-]	snow-off	Point reprojection, Section 2.4.1
$V_f^{\triangle}$	Sky view factor [-]	snow-on	Voxel ray sampling, Section 2.4.2
$V_f^{\blacktriangle}$	Sky view factor [-]	snow-off	Voxel ray sampling, Section 2.4.2

4.2.2 Quantifying spatial relationships between snow and canopy metrics

The strengths of monotonic relationships between snow and canopy within the forest plot metrics were assessed using Spearman's rank correlation coefficient (ρ_s, $\alpha = 0.05$). Spearman's rank was indicated due to generally nonparametric canopy metric distributions which displayed nonlinear and heteroscedastic relationships with SWE and ΔSWE estimates. As transmittance and contact number are related by a monotonically decreasing function, they share inversely symmetric ρ_s values with all covariates. As such, only results for transmittances were reported.

Variogram analysis was conducted for all SWE and ΔSWE products within the forest plot, as well as for ray sampled LAI metrics calculated over 1°, 15°, 60° and LAI_{2000} zenith-angle footprints. Characteristic length scales of variation are expressed as a fraction of the mean variation found between points at 30 m apart for each metric. Relative subpixel variance is reported for each analyzed snow and canopy metric, calculated as the variance between pixels within the local 8-connected neighborhood as a fraction of the variance found between points 30 m apart.

4.2.3 Exploring physical processes relating snow and canopy

Beyond quantifying relationships between snow and canopy metrics, there is a need to identify and distinguish the physical processes which are responsible for these relationships in the quest for an physical realism in conceptual and computational models (Clark et al., 2017). To better understand the angular dependence of the observed relationships between branch-scale subcanopy snow accumulation and canopy structure, the relationships between ΔSWE_f and light transmittance were analyzed for angles across the hemisphere. Spearman's correlation coefficient (ρ_s, $\alpha = 0.05$) was calculated between 25 cm-resolution ΔSWE_f estimates from each storm and light transmittance estimates calculated at 1°- angular resolution across the hemisphere from voxel ray sampling of snow-on lidar observation.

To assess the ability of different interception models to explain the observed spatial variation of snow accumulation, the strengths of the monotonic relationships between ΔSWE_f and ΔS_{snow} from throughfall estimates (Eq. 2.22) were evaluated for the Hedstrom-Pomeroy, Moeser et al., and Gaussian snowfall models using Spearman's rank correlation coefficient (ρ_s, $\alpha = 0.05$).

Total storm throughfall was estimated by the Hedstrom-Pomeroy model ($\overline{F_{HP}}\Delta t$) from Eq. 2.28 and Eq. 2.23 using the following spatially varying products: $C_c^{\blacktriangle}$, $LAI^{\blacktriangle}_{2000}$, and CHM. An additional run with LAI estimated by $LAI^{\blacktriangle}_{15}$ was also conducted. Spatially homogenous parameters for the Hedstrom-Pomeroy model were: $\overline{P \Uparrow} \Delta t$ estimated from areal ΔSWE estimates in the clearing for each storm, ρ_{fresh} estimated from Eq. 2.4 for each storm, and $\bar{S}$ = 5.9 kg m^{-2} for spruce trees (Schmidt and Gluns, 1991). The initial snow load within the canopy L_0 was unknown, but preliminary sensitivity analysis showed that the strongest Spearman's rank

correlation values were found at $L_0 = 0$. This value was used to provide an upper bound of the spatial correlation values.

Total storm throughfall was estimated by the Moeser et al. model ($\overline{F_M}\Delta t$) from Eq. 2.31 using the following spatially varying products: MDC, $C_c^{\blacktriangle}$, and TGA. Event precipitation ($\overline{P \Uparrow \Delta t}$) was estimated from areal ΔSWE estimates in the clearing for each storm and was assumed to be spatially homogenous.

Total storm throughfall was estimated by the Gaussian snowfall model ($\overline{F_j}\Delta t$) from Eq. 2.39 using voxel ray sampling estimates of contact number $\chi_{B(i,j)}$ taken at 1° angular resolution over the upper hemisphere and 25 cm resolution over the forest plot. The set of 31,123 spatial points from the 25 cm grid of the forest plot was randomly divided into training (50%) and test (50%) sets. The five parameters $\overline{P \Uparrow \Delta t}$, σ, ω^*/ω, $\phi_{\max}$, and $\theta_{\max}$ were determined by minimizing the squared error between modeled total storm throughfall $\overline{F_j}\Delta t$ and corresponding lidar estimates of ΔSWE_f from the training set using the BFGS algorithm (Wright and Nocedal, 1999), for each of the two snowfall events from Feb. 14 - 19 and from Feb. 19 – 21 as well as for SWE_f estimates for Feb. 21 . Coefficients of determination and Spearman's rank correlation coefficients were calculated between optimized values of $\overline{F_j}\Delta t$ and ΔSWE_f using the test set.

4.3 Results

4.3.1 Spatial distributions of snow and canopy metrics

Figure 4.1 shows a map of snow water equivalent SWE_f for 19 Feb. 2019 at 5 cm spatial resolution over the site, calculated from lidar snow depth and a constant forest snow density estimated from manual observations within the forest. Similar products for February 14th and 21st were also generated. Separate SWE_c maps were calculated for all dates using linear depth-density models from clearing observations (see Table 2.1 for snow density parameters). Horizontal interpolation was limited to a maximum of 10 cm from lidar snow surface returns. Gaps in observations (seen in grey) are due to occlusion of the ground from the perspectives of the lidar sensor by snow-ladened vegetation. Tracks can be seen where the snow was trampled for the completion of snow surveys. All trampled regions were masked prior to analysis of SWE as clear violations of the snow density assumptions. Figure 4.2 shows similar maps of ΔSWE_f for each storm, with corresponding products for ΔSWE_c also calculated (not shown).

Mean areal SWE_f over the forest plot ranged from 38.8 mm to 45.3 mm over the study period, or 32% - 34% of that for SWE_c found for the clearing plot (see *Table* 4.2, Figure 4.9). Forest snowpack coefficients of variations ranged from 0.364 to 0.443 over the study period, or 138% - 159% of those found for the clearing snowpack. Forest SWE_f distributions were well-described

by lognormal distributions for all three days ($R^2_{adj} \geq 0.992$, Figure 4.10). Coefficients of variation consistently increased with time over the study period for both forest and clearing snowpacks.

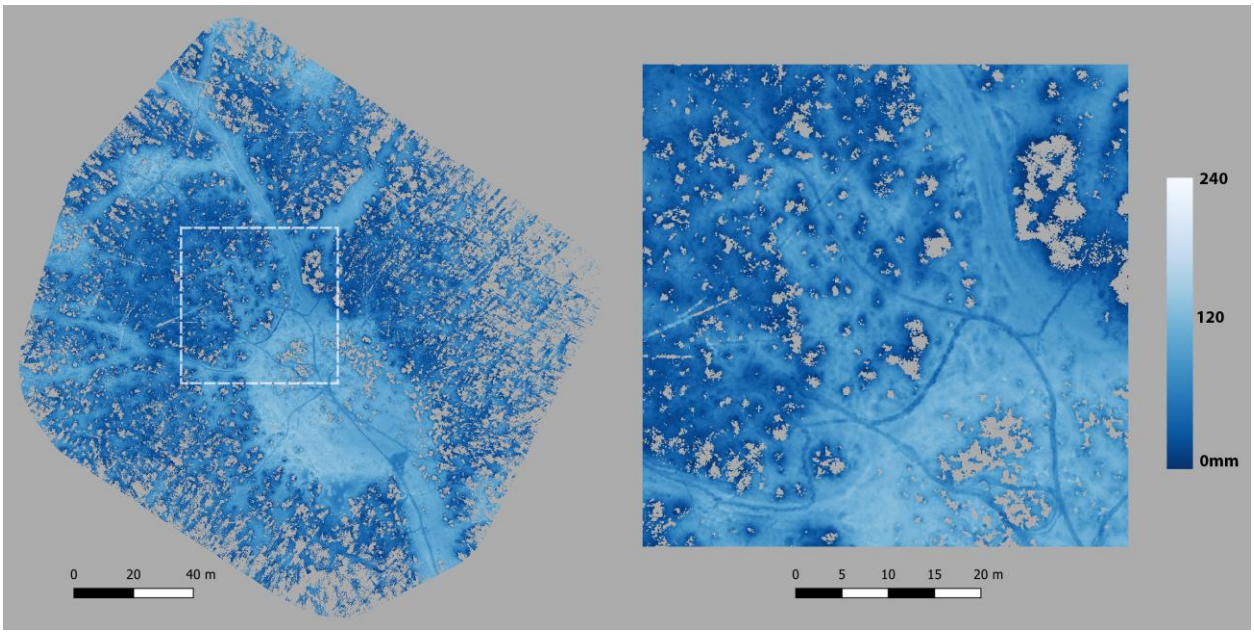

Figure 4.1: Snow water equivalent SWE_f using the forest snow density assumption for 19 Feb. 2019 at 5 cm spatial resolution over the site (closeup on right). SWE maps were generated for all three survey dates using both the forest and clearing density assumptions. Gaps in observations (shown in grey) correspond to regions greater than 10 horizontal cm from lidar snow depth observations.

Table 4.2: Areal means μ and coefficients of variation (c_v) of SWE over the forest and clearing plots, calculated from distributions corrected for sample bias with vegetation by rejection sampling.

Date	DOY	Forest SWE_f		Clearing SWE_c	
		μ [mm]	c_v [-]	μ [mm]	c_v [-]
2019-02-14	045	38.8	0.443	113	0.302
2019-02-19	050	40.4	0.431	122	0.273
2019-02-21	052	45.3	0.364	141	0.266

Mean areal ΔSWE_f over the forest plot was estimated at 1.77 mm for storm 1 and 4.95 mm for storm 2, with respective clearing ΔSWE_c estimates of 3.00 mm and 8.60 mm, resulting in 59% and 58% of clearing snowfall observed within the forest snowfall for each respective storm. Coefficients of variation were calculated at 1.38 and 0.472 for ΔSWE_f within the forest and 0.997 and 0.315 for ΔSWE_c within the clearing, for storms 1 and 2 respectively.

Areal statistics of canopy metrics over the forest plot are shown in Table 4.3. The observed mean distance to nearest tree of 1.29 m corresponds to an average stem density of ~6000 stems ha^{-1} within the forest (Figure 4.3). The median vegetation height was 6.88 m AGS (Figure 4.5), with a maximum crown height of 27.19 m AGS. Mean LAI_{2000} within the forest calculated from reprojected lidar returns of the snow-off canopy was 3.40, with a mean canopy closure of 0.816. Median vertical light transmittance was 63.4% for snow-off canopy conditions compared with 67.0% for the snow-on conditions over the forest plot, calculated from voxel ray sampling of lidar (see Figure 4.7) and decreased to 40.3% and 37.9% respectively when limited to points below canopy. Standard deviation vertical light transmittance was slightly greater for the snow-on canopy (38.1%) than for the snow-off canopy (35.5%), with spatial variation in light transmittance decreasing with increasing zenith angle in both cases (Figure 4.8.c).

Table 4.3: Aggregate statistics of canopy metrics over the forest plot. Medians are reported for both the set of all pixels and the set of canopy pixels only, defined by CHM ≥ 1 m.

Canopy metric	mean	standard deviation	median (all pixels)	median (canopy pixels)	max
CHM [m AGS]	7.55	6.32	7.73	10.7	27.2
DNT [m]	1.29	0.583	1.26	1.09	3.41
DCE [m]	-0.194	0.451	-0.200	-0.300	1.50
MCH [m AGS]	4.87	4.47	4.59	6.88	20.7
fCov [-]	0.604	0.399	0.765	0.889	1.00
LPM-L [-]	0.493	0.374	0.444	0.286	1.00
MDC [m]	22.2	11.4	19.0	15.9	84.2
TGA [m^2]	3223	4768	1641	1047	73958
$T_1^{\triangle}$ [-]	0.465	0.411	0.397	0.113	1.00
$T_1^{\blacktriangle}$ [-]	0.472	0.382	0.430	0.188	1.00
$T_{15}^{\triangle}$ [-]	0.354	0.196	0.329	0.263	1.00
$T_{15}^{\blacktriangle}$ [-]	0.384	0.177	0.362	0.307	0.992
$T_{15}^{\bullet}$ [-]	0.402	0.159	0.377	0.344	0.985
$T_{15\text{-}30}^{\triangle}$ [-]	0.201	0.0983	0.181	0.169	0.642
$T_{15\text{-}30}^{\blacktriangle}$ [-]	0.258	0.0930	0.241	0.233	0.687
$T_{15\text{-}30}^{\bullet}$ [-]	0.269	0.109	0.246	0.242	0.688
$LAI_{60}^{\triangle}$ [-]	8.24	1.02	8.34	8.48	12.8
$LAI_{60}^{\blacktriangle}$ [-]	4.99	0.518	4.97	5.03	7.58
$LAI_{2000}^{\bullet}$ [-]	3.70	0.626	3.67	3.71	5.41
$C_c^{\triangle}$ [-]	0.913	0.0380	0.921	0.927	0.993
$C_c^{\blacktriangle}$ [-]	0.870	0.0379	0.876	0.880	0.971
$C_c^{\bullet}$ [-]	0.842	0.0622	0.859	0.862	0.935
$V_f^{\triangle}$ [-]	0.112	0.0490	0.102	0.094	0.339
$V_f^{\blacktriangle}$ [-]	0.159	0.0476	0.152	0.146	0.396

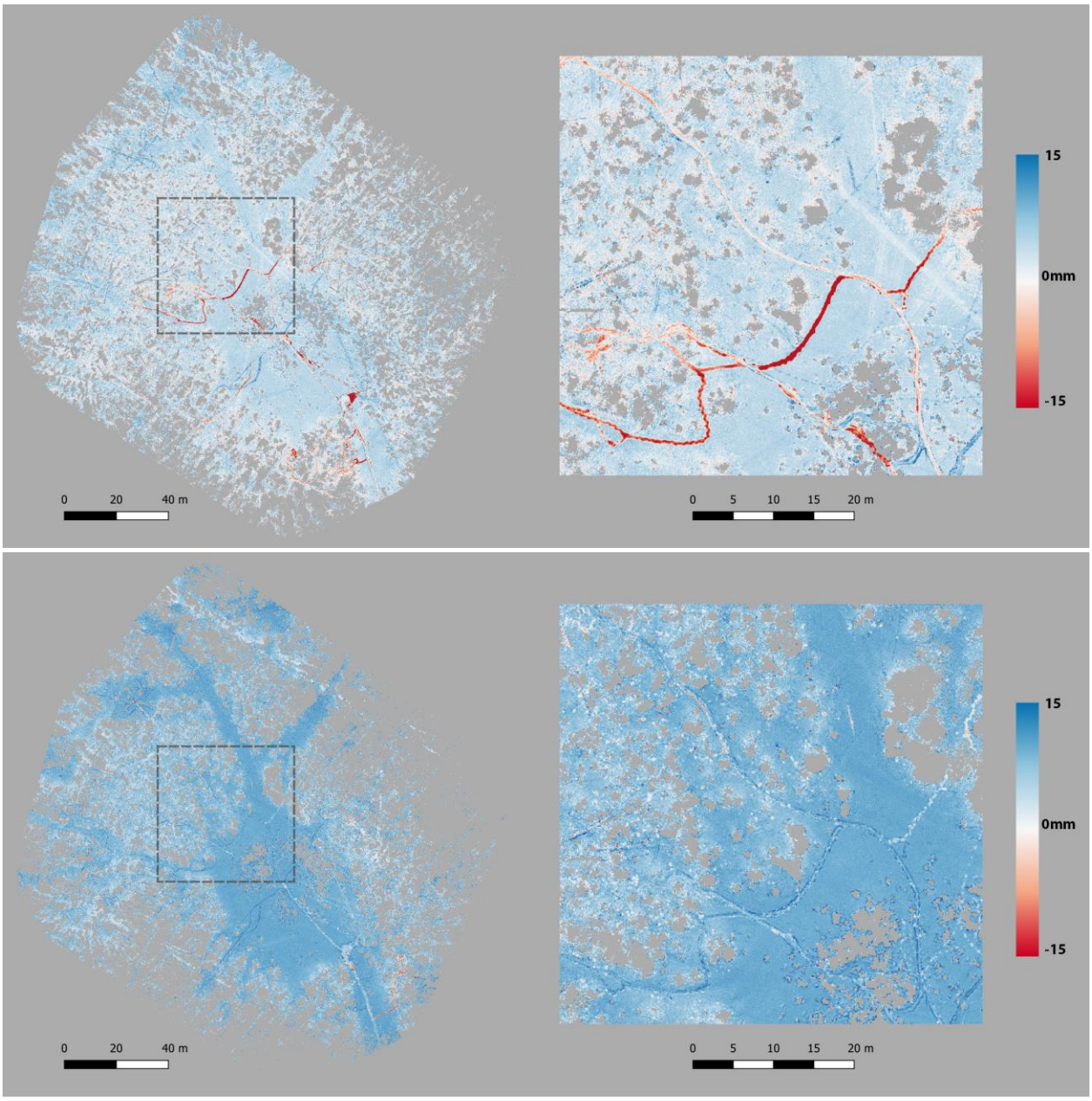

Figure 4.2: Change in snow water equivalent ΔSWE_f estimates for storm 1 (top) and storm 2 (bottom) calculated at 5 cm resolution over the siteusing the new snow density estimated for the forest. Gaps in observations are shown in gray. Tracks can be seen in both cases where snow was disturbed while conducting snow surveys, illustrating a clear violation of the snow density assumptions. All human-disturbed regions were masked prior to analysis. A close-up of the outlined square region is shown on the right.

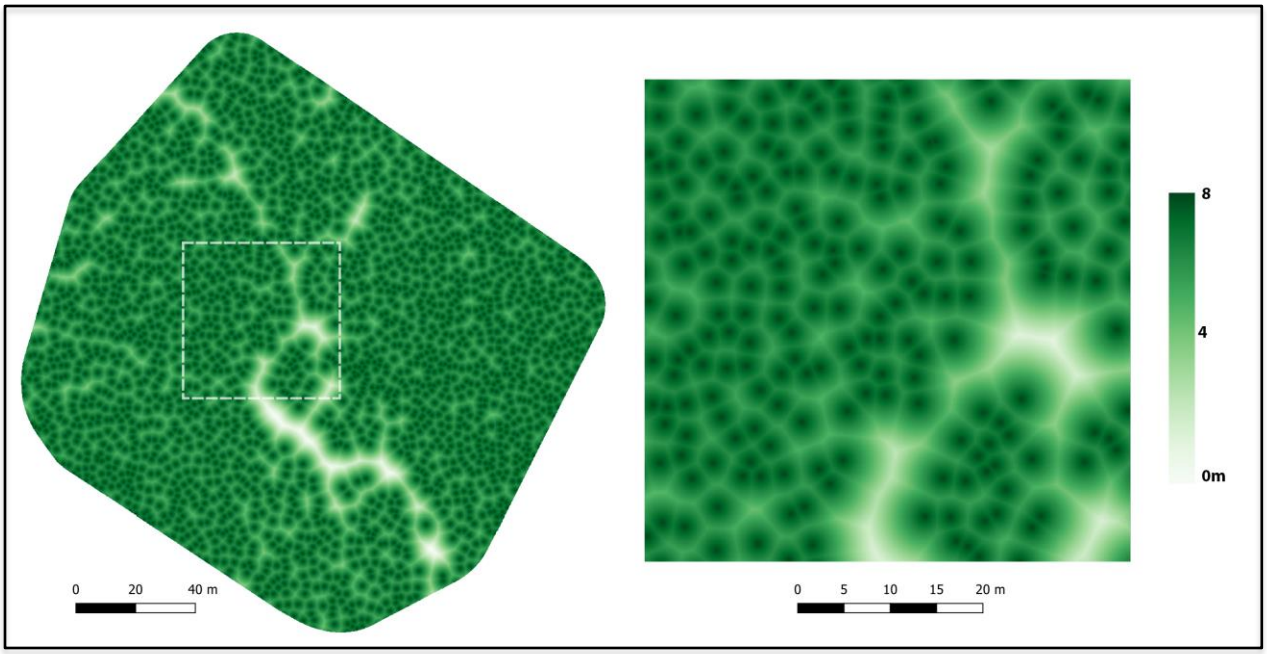

Figure 4.3: (top) Lateral distance to nearest tree (DNT) in meters calculated at 10 cm resolution across the site, using tree-tops to identify trees and assuming vertical trunks. Treetops were identified from the canopy crown height model derived from the snow-free lidar point cloud following Khosravipour et al. (2016). A close-up of the outlined square region is shown on the right.

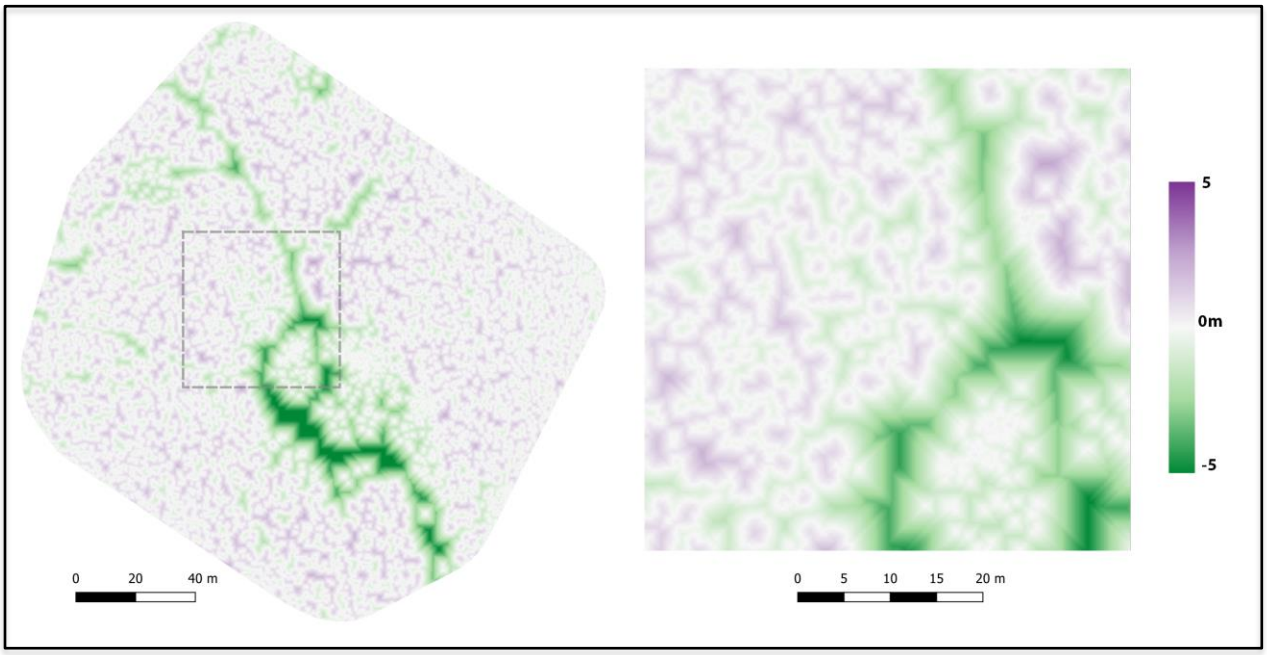

Figure 4.4: (bottom) Lateral distance to canopy edge (DCE) over the site, calculated from the lidar-derived canopy crown height model with 2 m AGS constituting the canopy edge following Mazzotti et al. (2019). A close-up of the outlined square region is shown on the right.

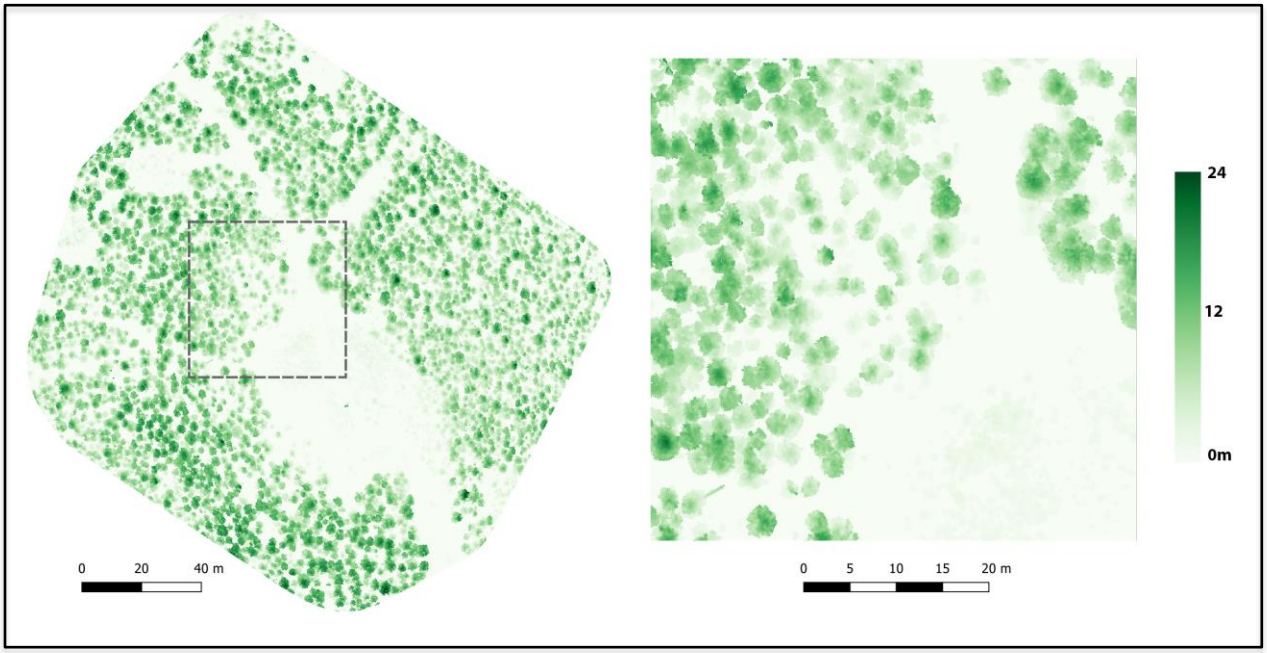

Figure 4.5: (top) Mean canopy height (MCH) [m AGS] calculated at 10 cm resolution over the site from the snow-free lidar point cloud following Khosravipour et al (2016). A close-up of the outlined square region is shown on the right.

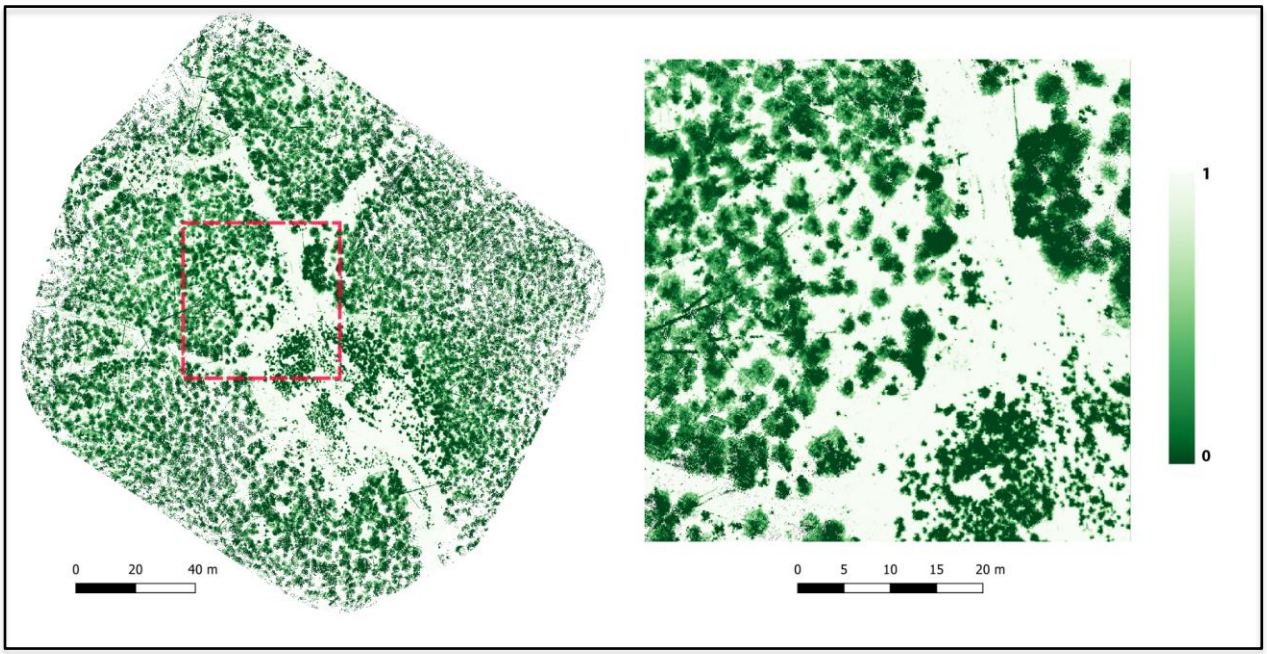

Figure 4.6: (bottom) Laser penetration of canopy (LPM-L) calculated at 10 cm resolution across the site from near vertical (± 15°) lidar samples. A close-up of the outlined square region is shown on the right.

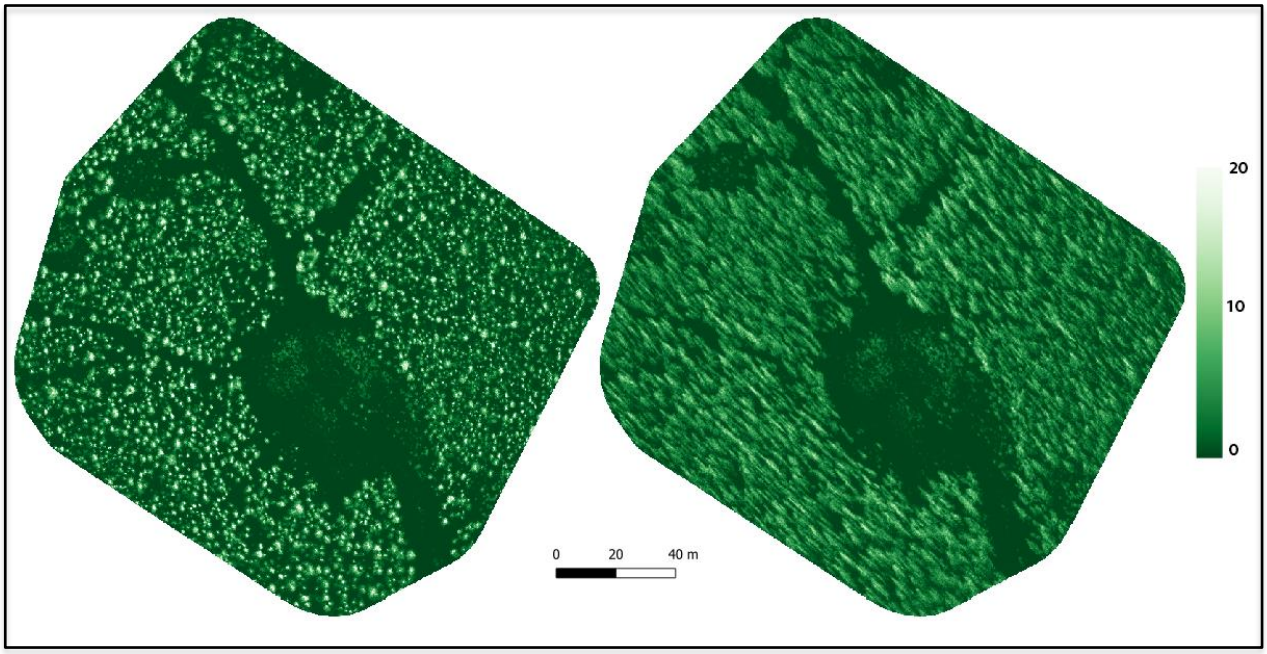

Figure 4.7: Contact numbers calculated for vertical rays (left) and rays 22.5° from zenith to the southeast (right) across the site at 25 cm resolution, from voxel ray sampling of the snow-free lidar point cloud. Contact numbers were calculated for over 30,000 ground points over the Forest plot at 1° angular resolution over the upper hemisphere, and for both snow-on and snow-off canopy conditions, for analysis with snow observations.

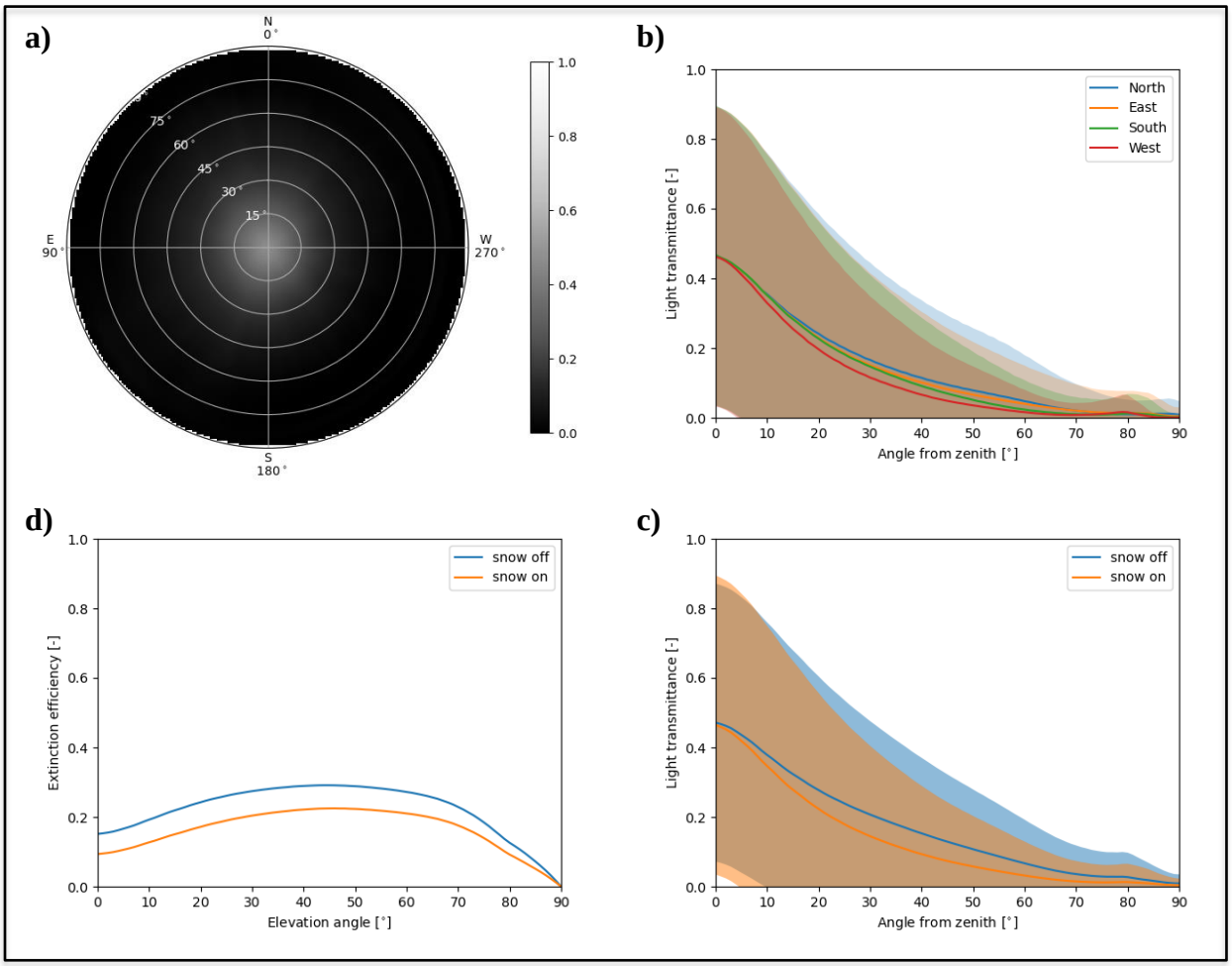

Figure 4.8: Clockwise from upper-left: (a) Mean light transmittance of the forest canopy in snow-on conditions (i.e. including intercepted snow) over the upper hemisphere, and (b) averaged by zenith angle and direction and shaded by standard deviation. (c) Comparison of mean light transmittances and (d) extinction efficiencies with zenith angle for snow-on and snow-off canopy conditions.

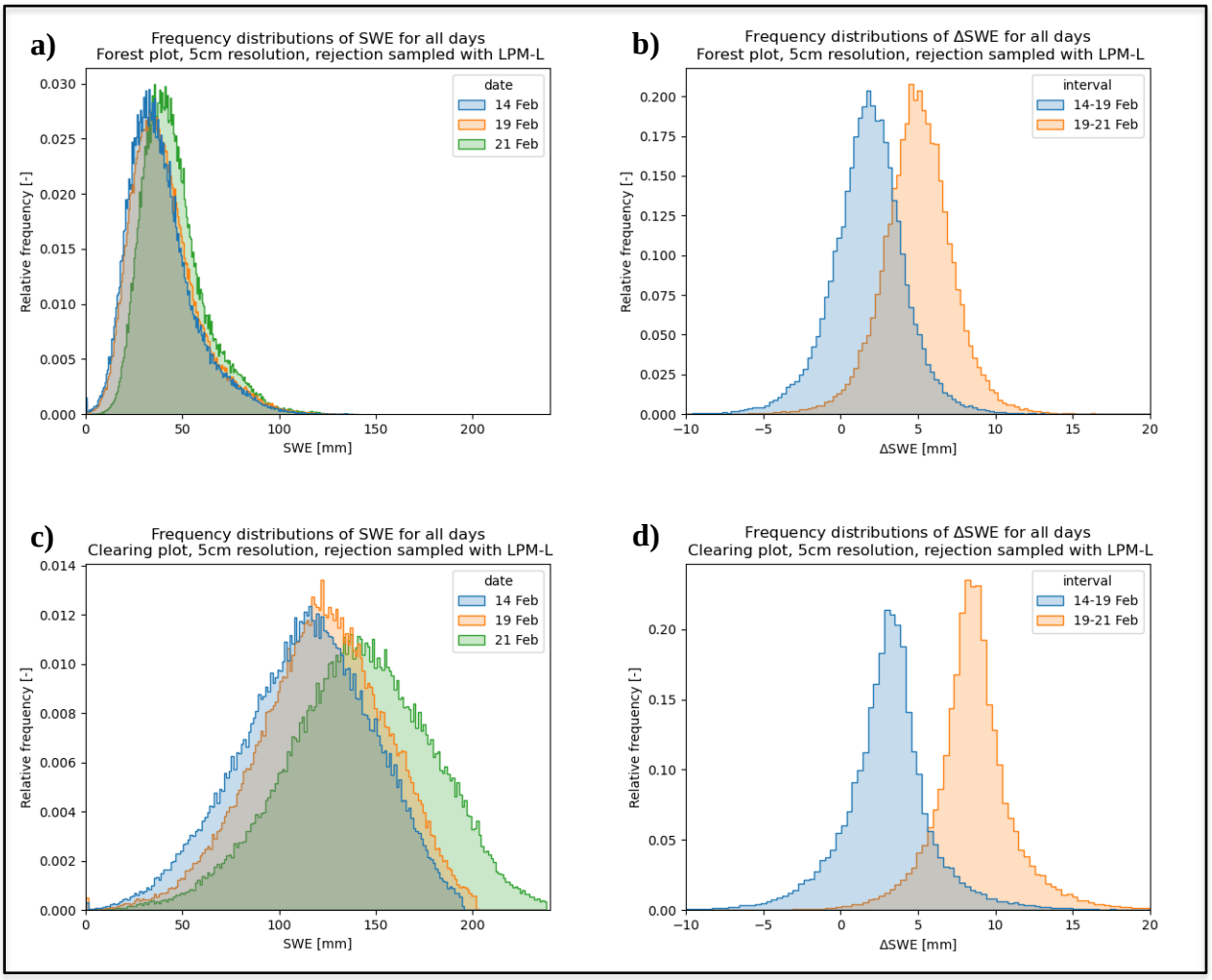

Figure 4.9: Distributions of (a) SWE_f and (b) ΔSWE_f within the forest plot and (c) SWE_c and (d) ΔSWE_c within the clearing plot, for all dates and intervals over the study period. All distributions were adjusted for sample bias by rejection sampling using the laser penetration metric LPM-L as a reference distribution.

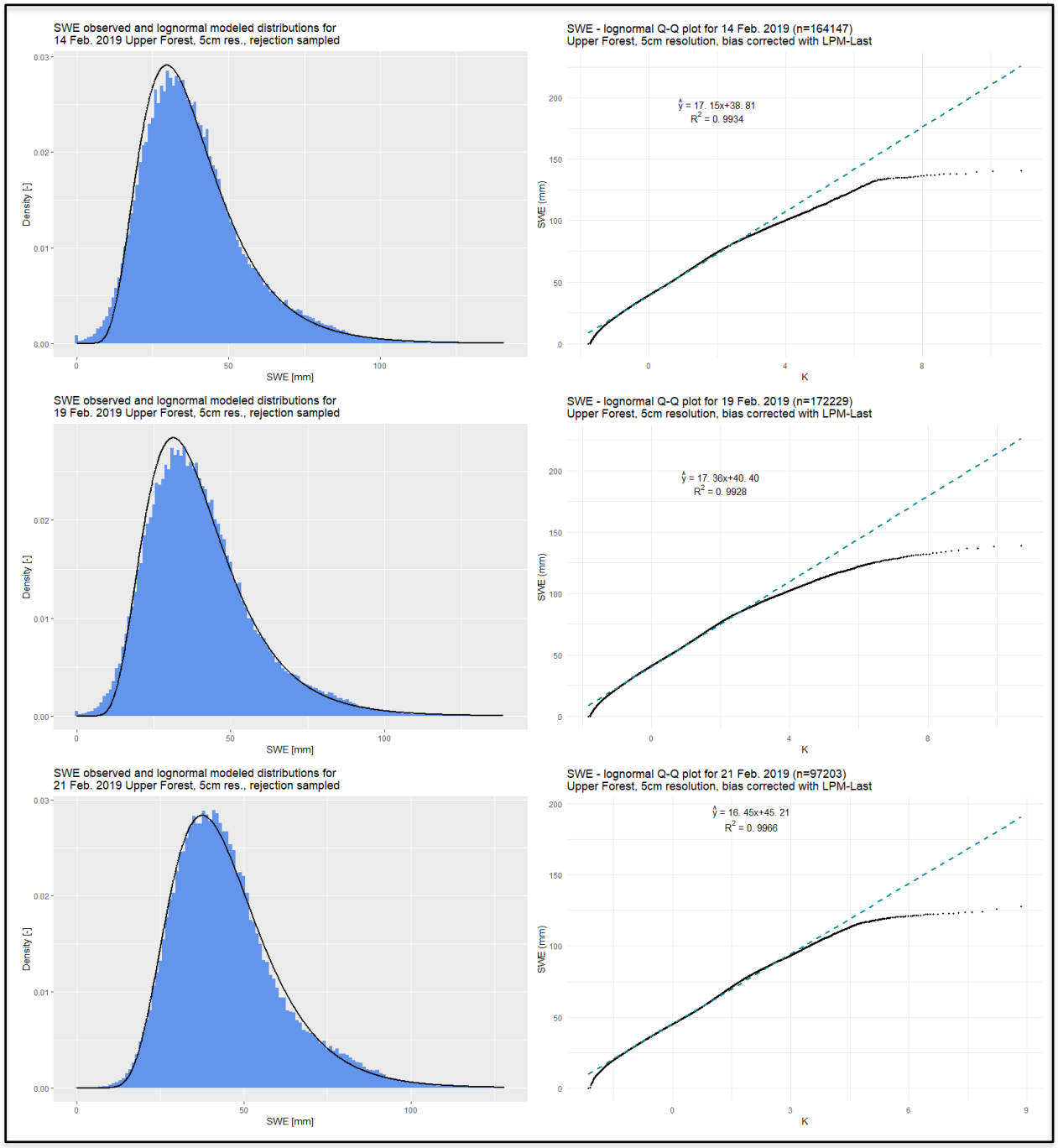

Figure 4.10: SWE distributions corrected for sample bias and fitted lognormal distributions (left) and the corresponding Q-Q plots with model fit (right) for each survey day. Mean and standard deviation of the modeled lognormal distributions correspond to the intercept and slope of the respective Q-Q plot linear regression, following (Shook and Gray, 1997).

4.3.2 Spatial relationships between snow and canopy metrics

The strengths, directions, and significances of the monotonic relationships of canopy metrics with SWE_f and ΔSWE_f within the forest plot are reported as Spearman's rank correlation coefficients (ρ_s) in Table 4.4. Of the individual metrics analyzed, the three 15°-light transmittance metrics (T_{15}) showed the strongest relationships with each SWE_f and ΔSWE_f estimate within the forest, with $T_{15}^{\triangle}$ from snow-on canopy conditions yielding the strongest relationships, followed by $T_{15}^{\blacktriangle}$ and then $T_{15}^{\bullet}$. $T_{15}^{\triangle}$ shared a stronger relationship with ΔSWE_f for storm 1 than for storm 2, while $T_{15\text{-}30}^{\triangle}$ shared a stronger relationship with ΔSWE_f for storm 2 than for storm 1. Ray sampling metrics from snow-on canopy conditions showed stronger relationships with snow metrics than those of snow-off conditions. For snow-off canopy metrics, ray sampling products showed stronger relationships with snow metrics than reprojection products except for *LAI* and C_c for storm 2. Of the canopy metrics not related directly to light transmittance, DCE consistently exhibited the strongest relationship with each snow metrics. The directions of the significant monotonic relationships are consistent across snow metrics for every canopy metric.

Table 4.4: Spearman's rank correlation coefficient (ρ_s) calculated between snow metrics (across) and select canopy metrics (down) over the forest plot. Canopy metric flags correspond to ray sampling under snow on ($^{\triangle}$) and snow-off ($^{\blacktriangle}$) canopy conditions, and snow-off point cloud reprojection ($^{\bullet}$) methods. Significant ρ_s values are marked with an asterisk (*). Corresponding p-values are shown in parentheses below ρ_s for p-value > .001 only.

	SWE Feb 14	SWE Feb 19	SWE Feb 21	ΔSWE Storm 1	ΔSWE Storm 2
CHM	-0.526*	-0.528*	-0.506*	-0.160*	-0.148*
DNT	0.298*	0.301*	0.278*	0.093*	0.074*
DCE	0.618*	0.620*	0.591*	0.187*	0.160*
MCH	-0.489*	-0.491*	-0.479*	-0.149*	-0.145*
fCov	-0.481*	-0.482*	-0.440*	-0.161*	-0.100*
LPM-L	0.455*	0.456*	0.413*	0.150*	0.088*
MDC	0.592*	0.590*	0.583*	0.252*	0.222*
TGA	0.570*	0.566*	0.561*	0.241*	0.216*
$T_1^{\triangle}$	0.620*	0.618*	0.578*	0.261*	0.171*
$T_1^{\blacktriangle}$	0.618*	0.616*	0.569*	0.257*	0.160*
$T_{15}^{\triangle}$	0.775*	0.778*	0.750*	0.340*	0.266*
$T_{15}^{\blacktriangle}$	0.760*	0.762*	0.729*	0.333*	0.257*
$T_{15}^{\bullet}$	0.678*	0.676*	0.674*	0.319*	0.244*
$T_{15-30}^{\triangle}$	0.552*	0.540*	0.532*	0.209*	0.228*
$T_{15-30}^{\blacktriangle}$	0.447*	0.437*	0.421*	0.165*	0.188*
$T_{15-30}^{\bullet}$	0.239*	0.215*	0.240*	0.036 (0.149)	0.144*
$LAI_{60}^{\triangle}$	-0.331*	-0.321*	-0.294*	-0.128*	-0.064*
$LAI_{60}^{\blacktriangle}$	-0.302*	-0.299*	-0.260*	-0.119*	-0.072*
$LAI_{2000}^{\bullet}$	-0.043 (0.071)	-0.026 (0.282)	-0.022 (0.373)	0.048 (0.051)	-0.023 (0.369)
$C_c^{\triangle}$	-0.570*	-0.557*	-0.543*	-0.212*	-0.212*
$C_c^{\blacktriangle}$	-0.453*	-0.445*	-0.417*	-0.162*	-0.162*
$C_c^{\bullet}$	-0.261*	-0.240*	-0.250*	-0.055* (0.027)	-0.136*
$V_f^{\triangle}$	0.621*	0.610*	0.595*	0.236*	0.229*
$V_f^{\blacktriangle}$	0.520*	0.512*	0.484*	0.191*	0.184*

Variogram analysis of SWE_f consistently shows two distinct length scales of variation across days, with the greatest increase in variance found within 5 m of lag distance corresponding to 63% - 72% of the total variance observed at 30 m (Figure 4.11.a). Variances continue to increase from 5 m to 30 m, but at reduced rates. The standard deviation of SWE_f among neighboring pixels (5 cm resolution) is 4.47 mm averaged across days, with corresponding variances below 3% of the variances seen at 30 m for all days. ΔSWE_f exhibits similar length scales of variation, with a consistent scale break around 5 m. A standard deviation of 2.19 mm between neighboring ΔSWE_f pixels (5 cm resolution) averaged across storms corresponds to 51.7% and 42.1% of the total variance observed at 30 m lag distance for storms 1 and 2, with 97% and 90% of the 30 m variance is observed by 5.0 m of lag distance, respectively. 88%% of the change in variance from 7.1 cm to 30 m is found within 2.0 m for storm 1 compared with 76% for storm 2. For 25 cm resolution ΔSWE_f estimates the standard deviation of neighboring pixels averages to 2.03 mm, corresponding to 66% and 63% of the variance observed at 30 m for storms 1 and 2. The relative variance of SWE_f for 21 Feb. 2019 is consistently lower than for the other days at distances below 15 m, and the relative variance of ΔSWE_f for storm 2 remains below that for storm 1 up to 23 m.

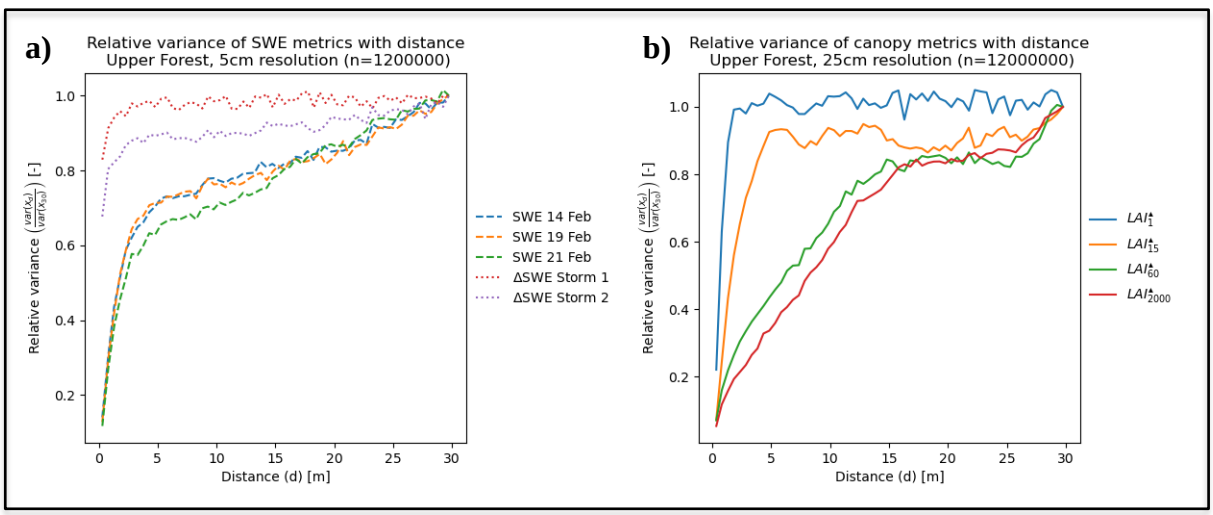

Figure 4.11: Variance with lag distance as a fraction of variance at 30 m for sets of sampled point pairs from (a) SWE and ΔSWE products and (b) ray sampled snow-off LAI metrics.

Variogram analysis of LAI estimates shows a general increase in length scales of variation with increasing angular footprint (Figure 4.11.b). $LAI_1^{\blacktriangle}$ exhibits the shortest length scales of variation of the tested metrics, with 90% of the 30 m variance observed within 1.3 m of lag distance. $LAI_{15}^{\blacktriangle}$ varies slightly slower with 90% of the 30 m variance observed within 4 m of lag distance. Both $LAI_{75}^{\blacktriangle}$ and $LAI_{2000}^{\blacktriangle}$ appear to reach a sill around 15 m lag distance corresponding to approximately 80% of the 30 m variance, with $LAI_{75}^{\blacktriangle}$ showing slightly faster convergence than $LAI_{2000}^{\blacktriangle}$. Variograms of $LAI_{15}^{\blacktriangle}$, $LAI_{75}^{\blacktriangle}$, and $LAI_{2000}^{\blacktriangle}$ all show a notable up-tick in variance between 25 m – 30 m.

4.3.3 Physical processes relating snow and canopy

Figure 4.12 shows Spearman's correlation coefficients (ρ_s) of light transmittance on the snow-on canopy with ΔSWE_f over the forest plot, for angles (ϕ, θ) over the upper hemisphere, for storms 1 and 2. The correlations with the greatest magnitude $|\rho_p|$ within 75° from vertical were consistently positive, with coefficients of 0.318 at (5.0°, 126.9°) for storm 1 and 0.310 at (8.1°, 150.3°) for storm 2. Negative correlations were generally weaker and found at greater zenith angles, with minimum correlation values of -0.0996 at (75.7°, 285.3°) for storm 1 and -0.209 at (63.8°, 283.6°) for storm 2. Figure 4.12 also shows ρ_s of canopy light transmittance with SWE_f for Feb. 21. Correlations were generally much stronger than for the individual storms, with the strongest correlation being 0.639 at (4.24°, 135.0°). The strongest negative correlation was found to be -0.271 at (89.9°, 261.7°).

Optimization of Gaussian snowfall model parameters with the training set differed between storms 1 and 2. The Gaussian distributions of above-canopy precipitation with angle were centered at (ϕ_{max}, θ_{max}) = (7.1°, 139.6°) with standard deviation σ = 6.59° for storm 1, and (ϕ_{max}, θ_{max}) = (14.3°, 138.6°) with σ = 9.20° for storm 2. Azimuthal asymmetry shows general agreement with predominant wind directions from the southeast for both storms (136.3° and 124.7°, respectively). The contact absorption coefficients for snow particles relative to light were optimized at ω^*/ω = 0.178 for storm 1 and ω^*/ω = 0.0881 for storm2. The total above canopy precipitation for the two storms was estimated as $\overline{P \Uparrow} \Delta t$ = 3.22 mm for storm 1 and $\overline{P \Uparrow} \Delta t$ = 6.84 mm for storm 2. Overall, the Gaussian models yielded coefficients of determination of R^2_{adj} = 0.095 for storm 1 and R^2_{adj} = 0.106 for storm 2 when analyzed with the test set. Assuming all of the variance found between neighboring pixels to be a product of noise, the R^2_{adj} values are inflated to 0.280 and 0.287 for storms 1 and 2. Spearman's rank correlation coefficients of ρ_s = 0.378 for storm 1 and ρ_s = 0.370 for storm 2 (p-values < 0.001). Mean areal ΔSWE_f over the forest plot represented 55.0% and 72.4% of estimated above-canopy precipitation for storms 1 and 2, respectively.

Optimization of Gaussian snowfall model parameters from the training set for analysis with SWE_f for Feb. 21 resulted in (ϕ_{max}, θ_{max}) = (6.9°, 134.0°) with σ = 9.41°. The contact absorption coefficients for snow particles relative to light were optimized at ω^*/ω = 0.211. The total above canopy precipitation from the observed snowpack was estimated as $\overline{P \Uparrow} \Delta t$ = 105 mm. Overall, the Gaussian model yielded coefficients of determination of R^2_{adj} = 0.707 and Spearman's rank correlation coefficient of ρ_s = 0.803 (p-value < 0.001) with the test set of SWE_f.

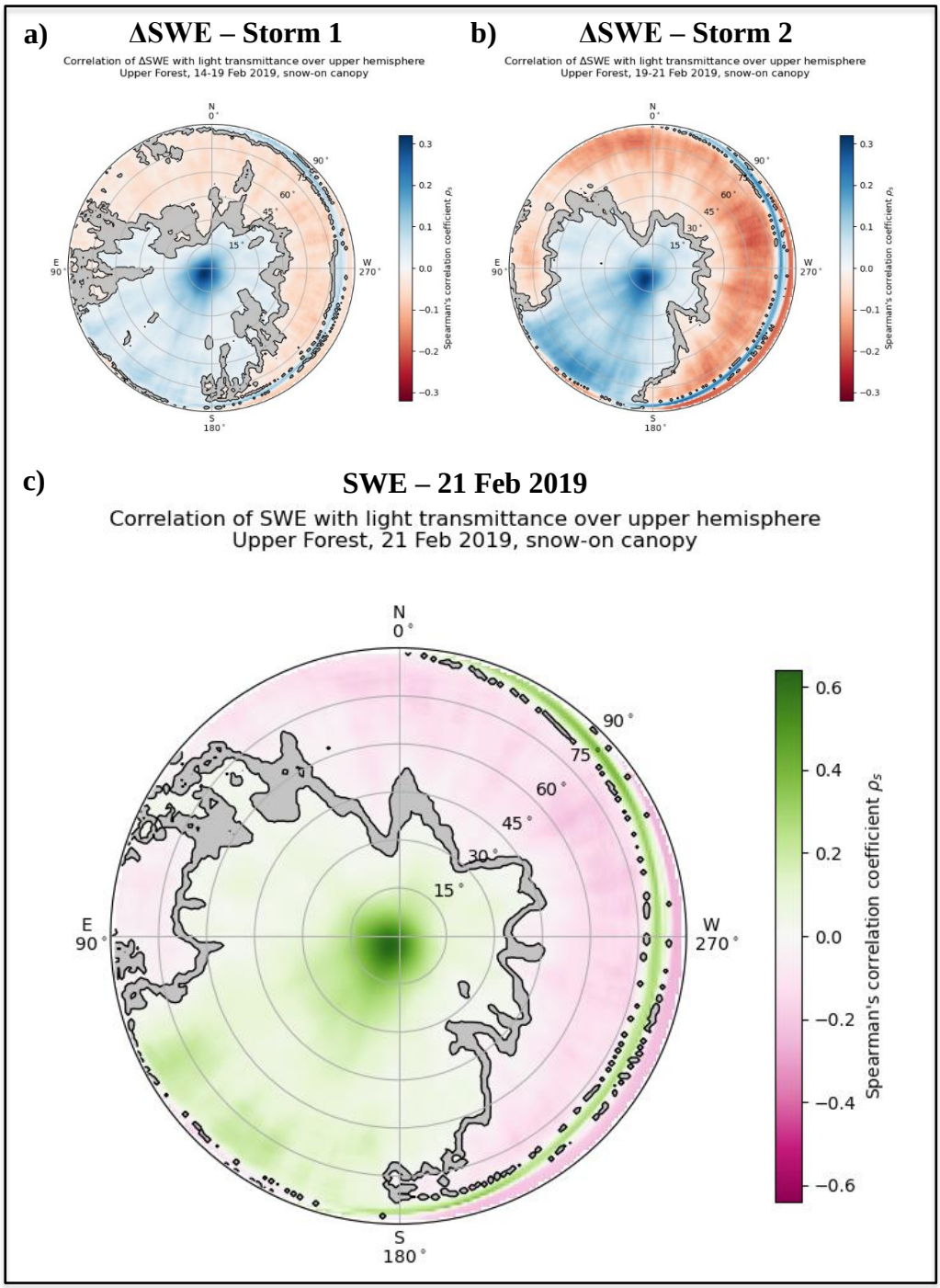

Figure 4.12: (a) Spearman's correlation coefficient (ρ_s) between snow-on light transmittance of the snow-on canopy (T^{Δ}) and ΔSWE_f for storm 1 (a), ΔSWE_f for storm 2 (b), and SWE_f for 21 Feb. 2019 (c) for angles across the hemisphere. The difference in colormaps represents a scale change in ρ_s. T^{Δ} was calculated at 1° angular resolution across hemisphere, with nonsignificant values shaded in grey ($\alpha = 0.05$). All plots are shown using the upward-facing perspective from the ground, with north to the top and east to the left.

Scatter plots ΔSWE_f and modeled throughfall estimates from the three models are shown in Figure 4.13, with corresponding Spearman's rank correlation coefficients (ρ_s) for each plot. Correlations of ΔSWE_f with throughfall estimated by the Gaussian snowfall model (ρ_s = 0.378 for storm 1 and ρ_s = 0.370 for storm 2) were stronger than any other throughfall estimates for both storms and were stronger than any correlations found with individual canopy metrics for the corresponding storm in Table 4.4, and stronger than any correlations with light transmittance of the canopy (Figure 4.13). Comparative performance of the Hedstrom-Pomeroy (ρ_s = 0.249 for storm 1 and ρ_s = 0.230 for storm 2) and Moeser et al. (ρ_s = 0.251 for storm 1 and ρ_s = 0.198 for storm 2) models was mixed, with Moeser et al. throughfall showing stronger monotonicity with ΔSWE_f for storm 1, and Hedstrom-Pomeroy throughfall showing stronger monotonicity for storm 2. Using $LAI^{\blacktriangle}_{15}$ instead of $LAI^{\blacktriangle}_{2000}$ to drive Hedstrom-Pomeroy throughfall estimates resulted in slightly stronger correlations for both storms (ρ_s = 0.262 for storm 1 and ρ_s = 0.258 for storm 2).

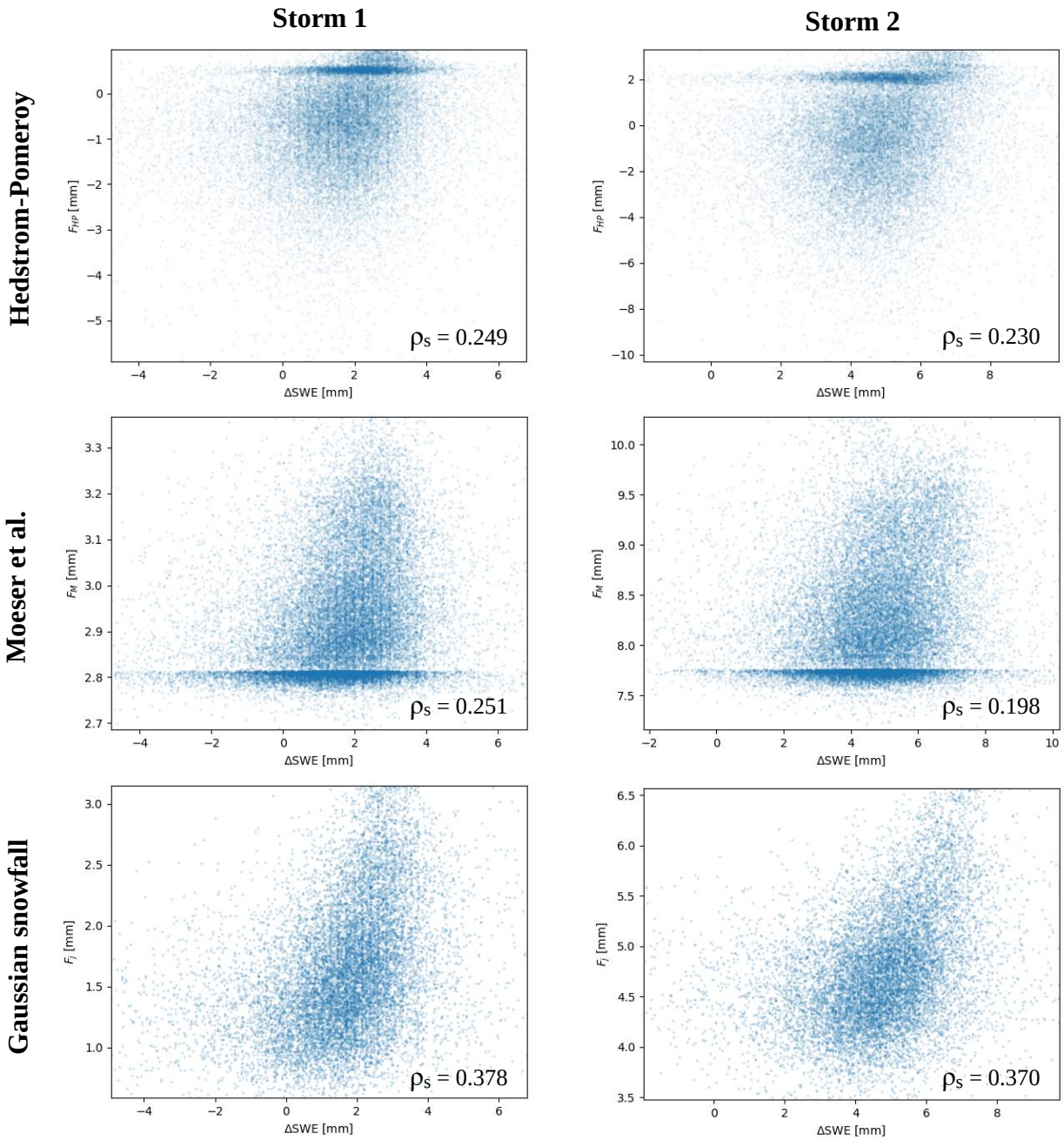

Figure 4.13: Scatter plots of observed ΔSWE_f within the forest (x-axis) vs. throughfall estimates (y-axis), for storm 1 (left) and storm 2 (right) modeled by Hedstrom-Pomeroy (top), Moeser et al. (middle), and the Gaussian snowfall (bottom) models. Spearman's rank correlation coefficients (ρ_s) are shown in the bottom right corner for each plot, with all corresponding p-values < 0.001

4.4 Discussion

4.4.1 Physical processes driving snow-vegetation relationships

Throughfall processes can explain the strongest, near-vertical components of snow-vegetation relationships observed over the sturdy period. Variation in snow accumulation within the forest was most strongly related to near-vertical light transmittance of the canopy with positive correlations indicating greater snow accumulation below near-vertical gaps in the forest canopy and less below dense canopy (Musselman et al., 2008). Of the canopy metrics considered, the strongest monotonic relationships with ΔSWE_f for both storms were found with mean light transmittance within 15° from vertical calculated by voxel ray sampling of lidar (T_{15}^{Δ}, Table 4.4). These correlations were slightly stronger than those with purely vertical light transmittance (T_1^{Δ}) and suggesting that the relationship is primarily, but not purely, vertical. This argument is further supported by the slightly weaker, positive monotonic relationships found with light transmittance from 15°-30° from vertical ($T_{15\text{-}30}^{\Delta}$). Figure 4.12 illustrates the angular spread of relevant near-vertical angles of throughfall over each storm interval. These patterns reveal vertical asymmetry in the near-vertical component of the snow-transmittance relationship, with maximum correlations skewed toward the southeast for both storms as for the Feb. 21 snowpack. Correlations for storm 2 showed greater angular spread and deviation from vertical compared with those for storm 1 and the Feb. 21 snowpack, as seen in the optimized parameters from the Gaussian snowfall model. As light transmittance is nearly vertically symmetric throughout the forest (Figure 4.8.a-b), the observed asymmetry in snow-vegetation relationships is most likely a result of the predominant wind patterns observed over the study period (Figure 2.5). Differences in wind regimes between storms may explain differences in near-vertical snow-transmittance relationships, with greater observed median and maximum wind speeds coinciding with the greater vertical asymmetry of storm 2 compared with those of storm 1. The angular spread of the positive correlations observed near vertical was also greater for storm 2 is likely due to temporal variation of fall vectors throughout each storm down to the scale of horizontal drift of individual falling snowflakes. The standard deviation parameter for the Gaussian snowfall model is therefore representative of random angular drift of particle trajectories in time around a mean fall vector, found to be within 15° from vertical for the two storms in the study period.

More complex relationships between snowfall and vegetation were observed at angles further from vertical and are evidence of the combination of several snowfall processes. Beyond approximately 30° from vertical, ΔSWE_f showed patterns of positive correlation with light transmittance for southern through eastern azimuths, while showing negative correlations with transmittance in other azimuthal directions (Figure 4.12). This pattern is consistent across storms, with notably greater magnitudes of correlations for storm 2 relative to storm 1, also seen in analysis of the Feb. 21 snowpack. The vertical asymmetry of the positive correlations beyond 30° from vertical is consistent with the asymmetry observed at near vertical angles and is likely also a result of the predominant southeasterly wind direction over the study period. The positive

upwind correlations are likely explained by throughfall caried by wind along non-vertical trajectories through the canopy, resulting in greater snowfall at locations within the forest with less upwind vegetation. The throughfall processes considered here are not limited to snow particles that do not touch vegetation, however. Particles that collide with vegetation and intercepted snow often rebound, and even those that are intercepted and unloaded within the time span of a given storm event are represented in the positive correlations observed in Figure 4.12. These upwind patterns may therefore include the downwind unloading of intercepted snow by wind gusts, which is an important example of how snow particles traveling on nonlinear trajectories may manifest in analysis with light transmittance along linear rays. The relatively stronger correlations seen upwind for storm 2 compared with storm 1 are consistent with this explanation. The secondary maximum near the horizon to the southeast in the hemispherical correlations for storm 2 (Figure 4.12.b) and for the Feb. 21 snowpack (Figure 4.12.c) may be an indication of blow-through effects in this forest, where the presence of nearby clearings combined with reduced vegetation densities within a few meters above the ground (Figure 3.2) can result in a secondary maximum in the wind speed profile within a few meters above the ground (Landsberg and James, 1971; Jiao-jun et al., 2004). The presence of blow-through effects may further explain the 13.9° discrepancy between the azimuth of the mean above-canopy wind vector and the azimuth of the observed precipitation maximum of the Gaussian snowfall model for storm 2.

Less apparent is the origin of the negative correlations found between ΔSWE_f and light transmittances beyond 30° from vertical and away from prevailing southeasterly winds (Figure 4.12). Negative correlations might signify greater snow losses with greater downwind transmittance due to wind transport of snow, coinciding with positive correlations at upwind angles near the horizon signifying greater snow gains with greater upwind transmittance. There is no mechanism for wind blown snow under these conditions, however. The low maximum wind speeds observed within the forest both storms (< 0.8 m s^{-1}) likely limited the shear stress on the snowpack, particularly considering the roughness of the nonerodable elements along the forest floor (Pomeroy and Gray, 1990). Furthermore, no obvious signs of wind erosion were noted within the forest while conducting snow surveys.

The observed pattern of negative correlations in Figure 4.12 may alternatively be explained by nonlinear snow particle trajectories around vegetation, resulting in preferential deposition of snow at locations with greater downwind vegetation density (and therefore less downwind light transmittance). This can be understood as a sheltering effect, whereby linear particle trajectories with downwind azimuthal components are deflected toward vertical due to decreased wind speeds in the presence of downwind vegetation, resulting in a concentration of trajectory termini in these regions analogous to the concentration of light by a lens. This effect may also apply to entrained snow particles that have been unloaded from the canopy due to wind gusts. While nonlinear trajectories should be expected for all entrained snow particles falling through a

vertical wind speed gradient, only the *spatial heterogeneity* of these nonlinear effects due to heterogeneous vegetation is expected to contribute the negative correlations observed between snow on the ground and downwind light transmittance of the canopy. Preferential deposition of snow has been observed and modeled for wind-entrained particles around terrain barriers (e.g. Comola et al., 2019), and is an area for future research in the context of vegetation.

The greater wind speeds seen during storm 2 may also explain the lower spatial variance of ΔSWE_f for storm 2 compared with storm 1, and the corresponding lower spatial variance of SWE_f for Feb. 21 (after storm 2) compared with previous days (Figure 4.11.a). Decreasing spatial variation of light transmittance with increasing angle from zenith was observed (Figure 4.8.c-d) and is an artifact of the erectophile structure typical of conifers (Eagleson, 2002). This suggests that greater deflection of snow particle trajectories from vertical results in less spatial variation of snow accumulation, consistent with observations for snow accumulation over storm 2. Such sensitivity of spatial variation of throughfall processes to wind patterns in forests has important implications for snow cover depletion in the melt season and is an area for future research.

While vertical asymmetry in snow-vegetation relationships were apparent in these high-resolution observations, the implications of asymmetry for larger-resolution and basin-scale models are less apparent. Models with spatial resolutions beyond several meters would overlook most of the spatial variation of snow accumulation found within the forest in this study. Representation of spatial variation of SWE is critical for estimating snow cover depletion in the melt season and is therefore commonly represented implicitly in such models (DeBeer and Pomeroy, 2017) – for example by modeling forest SWE with log-normal distributions (Shook and Gray, 1997). Decreasing light transmittance with increasing zenith angle within the forest (Figure 4.8.c) suggests that snow particle vectors further from vertical should see increased collisions with canopy and therefore increased interception rates and is a possible mechanism for reduced areal SWE and ΔSWE means from wind-driven asymmetry. Additionally, decreasing standard deviation of light transmittance with increasing zenith angle within the forest suggests that greater wind-driven asymmetry may yield reduced standard deviation of areal SWE and ΔSWE. Further research is needed to parameterize these relationships for use in larger scale models and should consider combined effects of asymmetry from both wind and slope.

4.4.2 Modeling spatial variation of snow accumulation in forests

Correlations of ΔSWE_f with throughfall estimated by the descriptive Gaussian snowfall model were stronger than those found with either the Hedstrom-Pomeroy or Moeser et al. model outputs (Figure 4.13), stronger than any of those found with the canopy metrics considered (Table 4.4), and stronger than all of those found with light transmittance of the canopy for individual rays across the hemisphere (Figure 4.12.a-b). Comparable (though slightly weaker) correlations with $T_{15}^{\triangle}$ for storm 1 were not surprising as the Gaussian model results in a distribution of significant transmittance weights which are predominantly within 15° from zenith. The notable decrease in correlations of ΔSWE_f with $T_{15}^{\triangle}$ for storm 2 compared with storm 1 were not reflected in Gaussian model outputs, however. This is likely a result of the increased asymmetry seen for storm 2, which is explicitly represented in the Gaussian model but not in the vertically symmetric $T_{15}^{\triangle}$ footprint. Despite showing the strongest correlations in this study, R^2_{adj} values between ΔSWE_f and throughfall from the Gaussian snowfall model remained below 11% for the two storms. This attributed primarily to the high level of spatial noise in the lidar change in snow depth (ΔHS_{lidar}) estimates resulting from measuring changes in snow depth in the range of 2 cm – 5 cm with a lidar system with 10 cm vertical accuracy for individual returns (accuracy is improved by analysis when there are multiple returns within a given pixel). While the noise in the snow depth (HS_{lidar}) measurements is of a similar magnitude, snow depth measurements in the range of 15 cm – 100 cm were generally larger than storm contributions resulting in a much smaller noise to signal ratio (see intercepts in Figure 4.11.a). Higher correlations for the descriptive Gaussian snowfall model compared with the predictive Hedstrom-Pomeroy and Moeser et al. models were not surprising as the former was recalibrated using training data from each storm, while the other two were not calibrated using these observations. The comparison is only used for context, and to inform steps to improve such predictive models.

Using multiple metrics in parallel to parameterize throughfall (as is done in the Hedstrom-Pomeroy and Moeser et al. models) is an encouraging way to capture variation over multiple length scales but can be easily implemented at the expense of a physical understanding of relationships between snow and vegetation. For example, while all throughfall models predict better for storm 1 accumulation compared with storm 2, it is not readily apparent why the Moeser et al. model results in more sensitivity to the differences between the two storms than the Hedstrom-Pomeroy model. Differences in model performance might be explained by the length scales of variation of model outputs which are constant across storms, but which are found to differ between storms 1 and 2 (Figure 4.11.a). Any intuition regarding the length scales of variation of the input canopy metrics for the two models is easily lost among the parametrizations which are used to combine them, however. This is also seen in the improvement of the performance of the Hedstrom-Pomeroy model when using $LAI_{15}^{\blacktriangle}$ rather than $LAI_{2000}^{\blacktriangle}$. From another perspective, because the Moeser et al. model parameters were optimized from observations in conditions with limited winds (Moeser, Stähli, et al., 2015), it seems plausible

that performance may drop for higher-wind conditions. Confirming this hypothesis and anticipating sensitivity to other environmental conditions by inspection of the optimized model parameters is not intuitive, however. In this study, several individual canopy metrics showed stronger spatial correlations with storm ΔSWE_f than either the Hedstrom-Pomeroy or Moeser et al. throughfall models (e.g., $T_{15}^{\triangle}$, $T_{15}^{\blacktriangle}$ and $T_{15}^{\bullet}$). Improved performance combined with more intuitive physical implications for throughfall processes provides a strong argument for using such individual metrics to drive spatial variation in throughfall models in place of the complex parameterization employed in combined models.

Above-canopy precipitation estimates for storms 1 and 2 differed among clearing precipitation gauge observations (9.03 mm and 6.85 mm), rejection sampled areal snowfall estimates over the clearing (3.00 mm and 8.60 mm) and Gaussian snowfall model estimates of above-canopy precipitation over the forest (3.22 mm and 6.84 mm). The large discrepancies in ΔSWE for storm 1 between the precipitation gauge estimate and the two lidar methods suggests a potentially critical issue with the new snow density model, as precipitation gauge values were substantiated by other gauges in the area. This can subsequently be attributed to fresh snow densities which differed from the estimates based on air temperature (all of which were near 68.0 kg m^{-3}; Hedstrom and Pomeroy, 1998), acoustic snow depth sensors which were not representative of plot-wise ΔHS (Lv and Pomeroy, 2020), or a combination thereof. However, error in the new snow density estimates results in spatially homogenous scalar errors in ΔSWE which do not change the results of spatial correlation analysis. There was no evidence of substantial wind transport between the clearing and forest plots was observed, limiting errors from this source (Lundberg and Halldin, 2001). Clumped unloading of intercepted snow into fresh snow below the forest is another possible source of error, which may have resulted in violations of the snow density assumptions used to estimate ΔSWE from ΔHS if unloaded clumps were not represented in snow density samples. Evidence of non-vertical, spatially heterogeneous, and nonlinear particle trajectories within the forest highlight scale limitations for estimating snow interception by the difference between above-canopy precipitation and throughfall (Eq. 1.9). Precipitation gauge, areal clearing, and modeled forest precipitation estimates show better agreement for storm 2.

Negligible ablation of snow assumed under the Gaussian snowfall model is easier to justify over the short time spans of the two storms as the effects of snow accumulation processes are expected to dominate changes in ΔSWE_f in these cases. This assumption is more challenging to justify for the analysis of SWE_f, which carries the effects of inter-storm and between-storm processes from the ~5-month period of preceding seasonal snow accumulation. The high R^2_{adj} values for the lognormal fitting of SWE_f distributions indicate that the observed snowpack is predominantly a result of accumulation processes, rather than ablation processes, assuming that snow accumulation and ablation processes are spatially related (Faria et al., 2000). Despite this, the seasonal above-canopy precipitation of $\overline{P \uparrow} \Delta t$ = 105 mm estimated by the Gaussian snowfall

model is substantially lower than the 187 mm cumulative seasonal precipitation (from October 1, 2018) reported by the clearing precipitation gauge. Early-season ablation from ground heat flux, above-freezing air temperatures, and possible rain on snow events may explain the large discrepancy in seasonal precipitation values and would constitute clear violations of the assumption of negligible ablation. The occurrence of an early, incomplete melt event may explain the heavy tails seen as the largest discrepancy of the SWE distributions from the theoretical log-normal distributions in Figure 4.10.

Optimized relative snow contact absorption coefficients (ω^*/ω) are less than 1 for both storms as well as for the Feb. 21 snowpack, satisfying the expectation that the probability of interception for snow particles given a contact is less than the probability of light absorption in all cases. The larger values for the Feb. 21 snowpack compared with the two storms – and for storm 1 compared with storm 2 – indicate a greater chance of interception earlier in the season compared with later. This is consistent with the understanding of canopy storage being closer to canopy capacity for storm 2 due to previous interception from storm 1 than it had been during storm 1 or earlier in the season. Greater interception probability calculated over the whole season compared with the two storms is consistent with the intercepted load being near capacity for the two storms, as suggested by the unloading events seen in the tree lysimeter (Figure 2.4). While the optimized ω^*/ω values are theoretically useful for estimating the probability of interception given a canopy contact, possible biases due to model assumptions (including linear particle trajectories, Gaussian above-canopy snowfall weights, and no clumped unloading from the canopy) limit the confidence in their explicit interpretation. Furthermore, estimates of ω^*/ω may also carry compensation for error in the estimate of ωc_χ from validation with thresholded hemispherical photography. In practice, therefore, these terms are useful for comparing relative probabilities of interception between storms but may be less robust in this application for estimating explicit interception probabilities.

Despite the improved performance for explaining spatial variation of SWE_f and ΔSWE_f, remaining unexplained variance (even after accounting for subpixel noise in ΔSWE_f) suggests gaps in the Gaussian snowfall model. The optimized Gaussian distributions effectively ignore snowfall contributions outside of 30° from vertical due to the relatively narrow, near-vertical Gaussian snowfall distributions fit for each storm as for the Feb. 21 snowpack. The Gaussian distribution was applied in this case to represent near-vertical throughfall processes with random drift around a central angle, but this parameterization overlooks off-vertical such as unloading from wind gusts or downwind sheltering by vegetation. The assumptions of homogenous above-canopy precipitation, linear particle trajectories and no wind transport explicitly limits this model to representing only positive correlations between snowfall transmittance and ΔSWE_f, in contrast to the observed positive and negative correlations with canopy transmittance in Figure 4.12. Furthermore, while the Gaussian snowfall model allows for some asymmetry in the selection of an arbitrary ($\phi_{\max}, \theta_{\max}$), it assumes a circularly symmetric relationship about ($\phi_{\max}, \theta_{\max}$) which

may be unrealistic in some conditions. Unexplained variance in an indicator of the importance of snow accumulation processes that are missed by these simplifying assumptions. The relatively narrow angular region which this model considers likely limits error from the assumption of a constant ω^* with angle, which may need to be more closely considered in other contexts. Further research is needed to balance the physical relevance, explanatory power, and scalability of canopy metrics for parametrizing snow accumulation processes in forests. Refining understandings of physical processes which drive snow accumulation in forests is important for anticipating model suitability and limitations and is central to informing land, water, and forest management decisions (Varhola et al., 2010).

The Gaussian snowfall model was implemented as a descriptive model in this research, but further work could be done to operationalize it as a predictive model. This work should involve parameterizing the five model parameters ($\overline{P \uparrow} \Delta t$, $\phi_{\max}$, $\theta_{\max}$, σ, and ω^*) by meteorological and forest structure variables. Above-canopy precipitation ($\overline{P \uparrow} \Delta t$) could be measured directly or estimated from clearing precipitation (Friesen et al., 2015). The azimuth of maximum throughfall ($\theta_{\max}$) could be estimated by mean wind direction for level forests but may also be dependent on ground slope angle and azimuth. Zenith angle of maximum throughfall ($\phi_{\max}$) might be parametrized by a combination of above canopy wind regimes, mean particle fall velocity, and either below-canopy wind regimes, or a canopy structure metric relevant for wind attenuation. Standard deviation of the gaussian distribution (σ) can be expected to depend on the standard deviation of wind speeds and directions within the forest, as well as aerodynamic particle factors (Nemes et al., 2017). And the snow particle contact absorption coefficient (ω^*) can be expected to depend on temperature (e.g. Kobayashi, 1987) in addition to canopy capacity and maximum storage (e.g. Hedstrom and Pomeroy, 1998).

4.4.3 Assessing canopy metrics for modeling snow accumulation

Length scales of variation of snow accumulation are a great indicator of the appropriateness of canopy metrics for explaining spatial patterns of snow accumulation in forests. In this study over 75% of the change in variance of ΔSWE_f observed in the variogram analysis for the two storms was found among points within 2.0 m apart (Figure 4.11.a). As spatial variation in snow at these scales is predominantly driven by variation in vegetation (Clark et al., 2011), canopy metrics that vary slower than ΔSWE_f are likely not representative of the most relevant canopy phenomena and are therefore poorly suited for linearly and independently characterizing the majority of variance in ΔSWE_f. The relatively lower Spearman's rank correlations between ΔSWE_f and the commonly-used wide-angle footprints LAI_{2000}, CC, and V_f (Table 4.4) are an indication of these limitations, as is the improved performance of the Hedstrom-Pomeroy spatial model using the smaller-footprint $LAI_{15}^{\blacktriangle}$ compared with $LAI_{2000}^{\blacktriangle}$. While metrics with small angular footprints are more appropriate for characterizing the small-scale variations in ΔSWE_f, too small a footprint may miss relevant variation at larger length scales. This can be seen in the rapid convergence of the variogram of LAI_1 (Figure 4.11.b) and is likely the source of the lower Spearman's rank values

of T_1 with ΔSWE_f compared with those of T_{15} (Table 4.4). Additionally, light transmittance metrics with small angular footprints show greater sensitivity to sample anomalies than those from larger footprints, and therefore may benefit more from the use of resampling methods such as voxel ray sampling of lidar. Ultimately, angular footprints should be selected which match the footprint of physical snowfall processes within the forest to accurately represent spatial variation in snow accumulation.

Correlations between ΔSWE_f and light transmittance of the canopy for angles over the hemisphere (seen in Figure 4.12.a-b) are useful for explaining the advantages and limitations of parameterizing snow accumulation by other metrics in terms of transmittance. For example, physical drivers of the observed difference in sign of correlations between C_c and V_f can be understood in terms of the difference in weights of hemispherical regions corresponding to near-vertical and off-vertical snow accumulation processes between the two metrics, which share different signs with vegetation when averaged over different zenith angle bands. Correlation coefficients over the hemisphere in Figure 4.12 are also useful for explaining differences in metric correlations between storms (Table 4.4), such as attributing the higher correlations found with $T_{15\text{-}30}$ over storm 2 to greater deviation from vertical symmetry compared with storm 1. Figure 4.12 also is useful for identifying the significance of vertical asymmetry in snow-vegetation relationships, which is overlooked by analysis with vertically symmetric metrics.

Of the metrics considered which are not explicitly related to light transmittance, distance from canopy edge (DCE) and mean distance to canopy (MDC) consistently showed stronger correlation with SWE_f and ΔSWE_f metrics (Table 4.4). DCE correlations comparable to those found with vertical transmittance T_1, combined with the ability to calculate directional DCE metrics, flexibility in length scale, and relatively small data and computation requirements all speak to the utility of DCE for modeling snow accumulation below around vegetation (Mazzotti et al., 2019). While slightly more computationally expensive, MDC and TGA are conceptually related to DCE and share many of these favorable attributes. Relationships between such distance-to-canopy metrics and vegetation density depend on patterns in crown shape which vary among species, sites, and the presence or absence of intercepted snow, and are sensitive to the threshold height used for metric calculation (Roth and Nolin, 2019). Further research to better understand relationships between distance-to-canopy and transmittance metrics across forests and conditions has the potential to strengthen physical interpretations and direct comparisons of distance-to-canopy and snow-vegetation relationships across forests and conditions.

Several canopy metrics including MDC, CHM, LPM-L, and fCov show saturation values whereby many pixels evaluate to a single metric value. These metrics cannot be used to explain variation among pixels which evaluate to the same value. This is the cause of the clumping observed in the scatter plots for the Moeser et al. model (due to MDC) and Hedstrom-Pomeroy model (due to CHM) in Figure 4.13, and limits model performance in both cases. In the case of

MDC, singular values arise for points below the canopy with a value close to zero, which might be avoided by following the DCE methodology of applying negative values to below-canopy points (Mazzotti et al., 2019). In the case of CHM, singular values arise in canopy gaps where canopy height is 0 m AGS and could be mitigated for this application by smoothing in space with a 2-D kernel. Spatial variation of LPM-L and fCov are sensitive to spatial resolution, whereby smaller resolutions yield bimodal distributions with singularities at 0 and 1. In all these cases, singularities result in a loss of information for a given data input and should therefore be mitigated or avoided where possible.

4.4.4 Feedbacks between snow interception and canopy structure

Canopy structure metrics derived from lidar observations from snow-on canopy conditions (i.e., forest canopy plus intercepted snow) consistently shared stronger correlations with SWE_f and ΔSWE_f estimates than equivalent metrics derived from snow-off canopy conditions (Table 4.4). This is consistent with previous research which has shown that snow interception alters the structure of the canopy, such that further snow accumulation patterns are affected (Hedstrom and Pomeroy, 1998). While in most cases the differences in explanatory power between canopy metrics were slight, these findings suggest that assumptions of a static canopy may result in non-intuitive parameterizations and reduced model performance.

While voxel ray sampling of lidar does not explicitly quantify the effects of intercepted snow on forest structure, differences between metrics derived from observations of snow-on and snow-off canopy conditions over the forest plot (Table 4.3) provided an indication of which structural changes were implicitly captured by voxel ray sampling outputs. Reduced median vertical light transmittance of over canopy pixels for snow-on conditions was consistent with the bridging of gaps between needles and branches by snow (Schmidt and Gluns, 1991). At the same time, standard deviation of vertical light transmittance of the canopy was greater for snow-on conditions due in part to branch compression by intercepted snow (Schmidt and Pomeroy, 1990) such that gaps between trees are greater with snow in the canopy (Figure 4.8.c). These two processes combined manifested in snow-on conditions corresponding to larger gaps and denser trees relative to snow-off canopy conditions.

4.5 Conclusions

High resolution, rejection-sampled forest SWE distributions were well-described by theoretical log-normal distributions, with higher coefficients of variation compared with those found for the clearing consistent with the literature. Most of the spatial variation in SWE and ΔSWE within the forest was found within 2.0 m of horizontal distance, emphasizing the need for observations of snow and canopy metrics at or below this scale to inform further development of snow accumulation models. Spatial variation in subcanopy SWE and ΔSWE showed the strongest correlations with near-vertical light transmittance of the canopy under snow-on conditions, as calculated from voxel ray sampling of lidar. Significant vertical asymmetry in was observed in

correlations between ΔSWE and light transmittance over the hemisphere which coincided with predominant wind directions over each storm. Surrounding canopy showed a complex relationship with snow accumulation, with upwind vegetation associated with less snow accumulation and downwind vegetation associated with more snow accumulation, and which appears to be sensitive to wind speeds during precipitation events.

Throughfall estimated from a descriptive Gaussian snowfall model explained more of the spatial variation in event snow accumulation than did estimates from either the predictive Hedstrom-Pomeroy or Moeser et al. models, with the advantage of allowing for explicit asymmetry in snow-vegetation relationships observed in this study and explained by prevailing wind directions. Despite these advantages, however, the Gaussian snowfall model only represented near-vertical throughfall and interception while neglecting snow-vegetation relationships at angles further from vertical corresponding to wind transport and sheltering processes. The Gaussian snowfall model is descriptive as the parameters were recalibrated for each of the two events studied, and therefore its utility as a predictive model needs further study. Further efforts to observe and characterize the contributions of these and other processes to snow accumulation in forests will result in greater robustness in models and the decisions that are informed by them.

Chapter 5: Conclusions

In this research, UAV lidar observations were combined with ground-based snowpack and canopy structure surveys to calculate snow and canopy metrics at the scale of branches and over the extent of a forest stand. Novel methods were developed and tested for improving analysis of lidar observations at these scales, including a novel voxel ray sampling method for modeling light transmittance properties of the canopy, and a rejection sampling method for addressing vegetation bias in areal snow depth estimates. These methods combined with others from the literature provided a deeper understanding of the physical processes driving branch-scale spatial patterns of snow accumulation in needleleaf forests.

Patterns of snow accumulation on the forest floor were found to encode patterns of interactions between falling snow and forest vegetation, with different snowfall processes explaining different angular relationships between snow accumulation and surrounding vegetation. Significant vertical asymmetry in spatial relationships between snow and canopy structure metrics within the forest was observed through hemispherical analysis and was explained by prevailing wind directions. At near-vertical zenith angles, reduced throughfall was generally associated with greater overhead vegetation due to greater interception, with the strongest associations skewed slightly upwind from vertical. The role of surrounding vegetation at greater zenith angles in shaping snowfall patterns showed sensitivity to both wind speeds and directions. Greater upwind vegetation corresponded to less snow accumulation particularly for the windier of the two observed storms, consistent with preferential deposition of throughfall along off-vertical particle trajectories. Surrounding vegetation away from prevailing winds exhibited a sheltering effect, whereby greater downwind vegetation was associated with greater snow accumulation, suggesting that preferential deposition may play an important role in shaping spatial heterogeneity of snow accumulation in forests. A novel, physically motivated Gaussian snowfall model was developed to explicitly characterized the observed asymmetry and showed the strongest correlations with observed forest ΔSWE of all metrics and models tested. Observed snow-vegetation relationships were stronger for metrics derived from snow-on canopy conditions than for those from snow-off conditions, emphasizing the importance of feedbacks between snow interception and canopy structure in accumulation processes. The physical realism of snow accumulation models stands to be improved by parameterizations which can represent vertical asymmetry and structural feedbacks in snow-vegetation relationships.

Most of the spatial variability in SWE and ΔSWE within the forest stand was found between points with distances from 0 m to 2 m apart, with limited marginal variation observed between points at greater distances. Areal SWE distributions calculated from 5 cm resolution observations were well described by theoretical log-normal distributions, consistent with previous observations in the literature reported for observations at larger resolution. Efforts to characterize spatial variation of snow accumulation should consider variation at or below the dominant length

scales of variation, whether implicitly or explicitly, in the interest of physical realism. For explicit models, this requires consideration of canopy metrics at similar length scales.

Significant covariance was observed between snow depths and ground point densities from UAV lidar observations resulting from lidar beam occlusion by vegetation, and which resulted in significant biases in areal snow depth estimates when standard interpolation methods were used to fill gaps in ground surface observations. Rasterization beyond the dominant length scales of variation of the snowpack was found to mask these biases. Similarly, vegetation height distributions estimated from UAV lidar return clouds were found to be skewed away from the lower canopy compared with resampled estimates due to occlusion of the lidar beam by vegetation. Resampling methods were found to reduce bias in areal snow depth, snow water equivalent (SWE), and vegetation height estimates and were therefore used throughout this study.

5.1.1 Future directions

This study was limited to two accumulation events over a single field site on the eastern slope of the Canadian Rockies. Confirmatory studies conducted over different environmental conditions for forests with different specie compositions, canopy structures, slopes, and aspects will facilitate a more robust understanding of relationships between snow accumulation and vegetation structure. Snow density assumptions represented a significant source of uncertainty for SWE and ΔSWE estimates which could be improved in future studies by more extensive manual snow surveys to accompany lidar surveys. Relationships between vegetation structure and snow redistribution and ablation processes were not explicitly considered in this analysis but are known to occur in parallel with throughfall and interception processes to shape spatial distributions of snow. Furthermore, while the methods used in this study were applied over forest stands, some may be challenging to implement at similar resolutions over the extent of hydrological basins due to current logistical and computational limitations. Despite these limitations, however, the findings from this research inform the further development of stand- and basin-scale models which consider the underlying physics of snow accumulation, redistribution, and ablation processes.

While the Gaussian snowfall model presents some advantages for modeling snow accumulation in forests, it relies on large data inputs and is motivated by assumptions which may be challenging to justify in certain conditions. Correlations between forest ΔSWE and light transmittance demonstrate the importance of snow-vegetation relationships which manifest across the upper hemisphere, not just at near-vertical angles. Further work to parameterize processes seen at greater zenith angles will make this model more physically realistic. Preferential deposition effects due to nonlinear particle trajectories or trajectories with non-uniform weights (e.g., Mazzotti et al., 2020) may be incorporated into future ray sampling metrics to better represent the physics of snow particles falling through forests. Furthermore, the

large data requirements due to the high dimensionality of ray sampling analysis over the hemisphere may be reduced by principal component analysis (PCA), machine learning, or other dimension reduction methods, ideally while preserving the physical interpretation of processes such as throughfall and interception which this model was developed to represent. Clever navigation of assumptions may also yield more convenient analytical solutions to the integral in Eq. 2.38, similar to those used in Nijssen and Lettenmaier (1999). Parametrizations used in existing models such as Hedstrom-Pomeroy and Moeser et al. could be informed by observations of interception processes such as those presented in this study, to improve their ability to explain spatial variation in snow accumulation in forests. Further research is needed to better understand the drivers of the patterns observed in this study, as well as what may have been overlooked by these observations.

Canopy metrics calculated from voxel ray sampling of lidar showed consistently stronger relationships with SWE and ΔSWE than metrics derived from reprojection of the lidar point cloud. Combined with the capacity for canopy analysis at high angular resolution, this method shows great promise for overcoming some of the issues that come with other methods. There remains a great potential for further development to improve the robustness of metrics derived from voxel ray sampling of lidar, including the utilization of lidar return intensity information, incorporation of non-spherical leaf angle distributions and variable reflectance of canopy, and explicit consideration of beam intensity and footprint size with distance. Additionally, further work is needed to characterize errors in the analysis of thresholded hemispherical imagery associated with the thresholding and commutation assumptions discussed in this study. These steps will allow for voxel ray sampling of lidar to be utilized as a standalone method, to be applied in parallel with hemispherical photography analysis rather than in series.

Chapter 6: References

Alexander, C., Moeslund, J. E., Bøcher, P. K., Arge, L., & Svenning, J. C. (2013). Airborne laser scanner (LiDAR) proxies for understory light conditions. *Remote Sensing of Environment*, *134*, 152–161. https://doi.org/10.1016/j.rse.2013.02.028

Alonzo, M., Bookhagen, B., McFadden, J. P., Sun, A., & Roberts, D. A. (2015). Mapping urban forest leaf area index with airborne lidar using penetration metrics and allometry. *Remote Sensing of Environment*, *162*, 141–153. https://doi.org/10.1016/j.rse.2015.02.025

Andreadis, K. M., Storck, P., & Lettenmaier, D. P. (2009). Modeling snow accumulation and ablation processes in forested environments. *Water Resources Research*, *45*(5), 1–13. https://doi.org/10.1029/2008WR007042

Béland, M., Parker, G., Sparrow, B., Harding, D., Chasmer, L., Phinn, S., … Strahler, A. (2019). On promoting the use of lidar systems in forest ecosystem research. *Forest Ecology and Management*, *450*(June). https://doi.org/10.1016/j.foreco.2019.117484

Béland, M., Widlowski, J. L., & Fournier, R. A. (2014). A model for deriving voxel-level tree leaf area density estimates from ground-based LiDAR. *Environmental Modelling and Software*, *51*, 184–189. https://doi.org/10.1016/j.envsoft.2013.09.034

Béland, M., Widlowski, J. L., Fournier, R. A., Côté, J. F., & Verstraete, M. M. (2011). Estimating leaf area distribution in savanna trees from terrestrial LiDAR measurements. *Agricultural and Forest Meteorology*, *151*(9), 1252–1266. https://doi.org/10.1016/j.agrformet.2011.05.004

Bolstad, W. M. (2009). Monte Carlo Sampling from the Posterior. *Understanding Computational Bayesian Statistics*, 25–46. https://doi.org/10.1002/9780470567371.ch2

Bolstad, W. M., & Curran, J. M. (2016). *Introduction to Bayseian Statistics*. https://doi.org/10.1080/00220973.1968.11011114

Broxton, P. D., Harpold, A. A., Biederman, J. A., Troch, P. A., Molotch, N. P., & Brooks, P. D. (2015). Quantifying the effects of vegetation structure on snow accumulation and ablation in mixed-conifer forests. *Ecohydrology*, *8*(6), 1073–1094. https://doi.org/10.1002/eco.1565

Broxton, P. D., van Leeuwen, W. J. D., & Biederman, J. A. (2019). Improving Snow Water Equivalent Maps With Machine Learning of Snow Survey and Lidar Measurements. *Water Resources Research*, *55*(5), 3739–3757. https://doi.org/10.1029/2018WR024146

Calder, I. (1990). *Evaporation in the uplands*. Chichester, New York: Wiley.

Campbell Scientific Canada. (2009). *SR50A Sonic Ranging Sensor: Instruction manual*. Edmonton, Alberta: Campbell Scientific Canada Corp.

Chasmer, L., Hopkinson, C., Smith, B., & Treitz, P. (2006). Examining the influence of changing laser pulse repetition frequencies on conifer forest canopy returns. *Photogrammetric Engineering and Remote Sensing*, *72*(12), 1359–1367. https://doi.org/10.14358/PERS.72.12.1359

Chen, J.M., & Black, T. A. (1991). Measuring leaf area index of plant canopies with branch architecture. *Agricultural and Forest Meteorology*, *57*(1–3), 1–12. https://doi.org/10.1016/0168-1923(91)90074-Z

Chen, Jing M., & Cihlar, J. (1995). Quantifying the Effect of Canopy Architecture on Optical Measurements of Leaf Area Index Using Two Gap Size Analysis Methods. *IEEE Transactions on Geoscience and Remote Sensing*, *33*(3), 777–787. https://doi.org/10.1109/36.387593

Chen, Jing M., Rich, P. M., Gower, S. T., Norman, J. M., & Plummer, S. (1997). Leaf area index of boreal forests: Theory, techniques, and measurements. *Journal of Geophysical Research*

Atmospheres, *102*(24), 29429–29443. https://doi.org/10.1029/97jd01107
Clark, M. P., Bierkens, M. F. P., Samaniego, L., Woods, R. A., Uijlenhoet, R., Bennett, K. E., … Peters-Lidard, C. D. (2017). The evolution of process-based hydrologic models: Historical challenges and the collective quest for physical realism. *Hydrology and Earth System Sciences*, *21*(7), 3427–3440. https://doi.org/10.5194/hess-21-3427-2017
Clark, M. P., Hendrikx, J., Slater, A. G., Kavetski, D., Anderson, B., Cullen, N. J., … Woods, R. A. (2011). Representing spatial variability of snow water equivalent in hydrologic and land-surface models: A review. *Water Resources Research*, *47*(7). https://doi.org/10.1029/2011WR010745
Comola, F., Giometto, M. G., Salesky, S. T., Parlange, M. B., & Lehning, M. (2019). Preferential Deposition of Snow and Dust Over Hills: Governing Processes and Relevant Scales. *Journal of Geophysical Research: Atmospheres*, *124*(14), 7951–7974. https://doi.org/10.1029/2018JD029614
Curtis, P. G., Slay, C. M., Harris, N. L., Tyukavina, A., & Hansen, M. C. (2018). Classifying drivers of global forest loss. *Science*, *361*(6407), 1108–1111. https://doi.org/10.1126/science.aau3445
DeBeer, C. M., & Pomeroy, J. W. (2010). Simulation of the snowmelt runoff contributing area in a small alpine basin. *Hydrology and Earth System Sciences*, *14*(7), 1205–1219. https://doi.org/10.5194/hess-14-1205-2010
DeBeer, C. M., & Pomeroy, J. W. (2017). Influence of snowpack and melt energy heterogeneity on snow cover depletion and snowmelt runoff simulation in a cold mountain environment. *Journal of Hydrology*, *553*, 199–213. https://doi.org/10.1016/j.jhydrol.2017.07.051
Deems, J. S., Fassnacht, S. R., & Elder, K. J. (2006). Fractal Distribution of Snow Depth from Lidar Data. *Journal of Hydrometeorology*, *7*(2), 285–297. https://doi.org/10.1175/JHM487.1
Deems, J. S., & Painter, T. H. (2006). Lidar measurement of snow depth: accuracy and error sources. *Proceedings of the 2006 International Snow Science Workshop: Telluride, Colorado, USA, International Snow Science Workshop*, *330*, 330–338.
Deems, J. S., Painter, T. H., & Finnegan, D. C. (2013). Lidar measurement of snow depth: A review. *Journal of Glaciology*, *59*(215), 467–479. https://doi.org/10.3189/2013JoG12J154
Dickerson-Lange, S. E., Gersonde, R. F., Hubbart, J. A., Link, T. E., Nolin, A. W., Perry, G. H., … Lundquist, J. D. (2017). Snow disappearance timing is dominated by forest effects on snow accumulation in warm winter climates of the Pacific Northwest, United States. *Hydrological Processes*, *31*(10), 1846–1862. https://doi.org/10.1002/hyp.11144
Eagleson, P. S. (2002). *Ecohydrology*. https://doi.org/10.1017/CBO9780511535680
Ellis, C. R., Pomeroy, J. W., Brown, T., & MacDonald, J. (2010). Simulation of snow accumulation and melt in needleleaf forest environments. *Hydrology and Earth System Sciences*, *14*(6), 925–940. https://doi.org/10.5194/hess-14-925-2010
Ellis, C. R., Pomeroy, J. W., & Link, T. E. (2013). Modeling increases in snowmelt yield and desynchronization resulting from forest gap-thinning treatments in a northern mountain headwater basin. *Water Resources Research*, *49*(2), 936–949. https://doi.org/10.1002/wrcr.20089
Essery, R., Bunting, P., Hardy, J., Link, T., Marks, D., Melloh, R., … Rutter, N. (2008). Radiative transfer modeling of a coniferous canopy characterized by airborne remote sensing. *Journal of Hydrometeorology*, *9*(2), 228–241. https://doi.org/10.1175/2007JHM870.1

Essery, R., Pomeroy, J. W., Parviainen, J., & Storck, P. (2003). Sublimation of Snow from Coniferous Forests in a Climate Model. *Journal of Climate*, *16*(11), 1855–1864. https://doi.org/10.1175/1520-0442(2003)016<1855:SOSFCF>2.0.CO;2

Fang, X., Pomeroy, J. W., Ellis, C. R., MacDonald, M. K., Debeer, C. M., & Brown, T. (2013). Multi-variable evaluation of hydrological model predictions for a headwater basin in the Canadian Rocky Mountains. *Hydrology and Earth System Sciences*, *17*(4), 1635–1659. https://doi.org/10.5194/hess-17-1635-2013

Fang, Xing, Pomeroy, J. W., Debeer, C. M., Harder, P., & Siemens, E. (2019). Hydrometeorological data from Marmot Creek Research Basin, Canadian Rockies. *Earth System Science Data*, *11*(2), 455–471. https://doi.org/10.5194/essd-11-455-2019

Faria, D. A., Pomeroy, J. W., & Essery, R. L. H. (2000). Effect of covariance between ablation and snow water equivalent on depletion of snow-covered area in a forest. *Hydrological Processes*, *14*(15), 2683–2695. https://doi.org/10.1002/1099-1085(20001030)14:15<2683::AID-HYP86>3.0.CO;2-N

Frei, A., Tedesco, M., Lee, S., Foster, J., Hall, D. K., Kelly, R., & Robinson, D. A. (2012). A review of global satellite-derived snow products. *Advances in Space Research*, *50*(8), 1007–1029. https://doi.org/10.1016/j.asr.2011.12.021

Friesen, J., Lundquist, J., & Van Stan, J. T. (2015). Evolution of forest precipitation water storage measurement methods. *Hydrological Processes*, *29*(11), 2504–2520. https://doi.org/10.1002/hyp.10376

Gelfan, A. N., Pomeroy, J. W., & Kuchment, L. S. (2004). Modeling Forest Cover Influences on Snow Accumulation, Sublimation, and Melt. *Journal of Hydrometeorology*, *5*(5), 785–803. https://doi.org/10.1175/1525-7541(2004)005<0785:MFCIOS>2.0.CO;2

Golding, D. L., & Swanson, R. H. (1978). Snow accumulation and melt in small forest openings in Alberta. *Canadian Journal of Forest Research*, *8*(4), 380–388. https://doi.org/10.1139/x78-057

Grotti, M., Calders, K., Origo, N., Puletti, N., Alivernini, A., Ferrara, C., & Chianucci, F. (2020). An intensity, image-based method to estimate gap fraction, canopy openness and effective leaf area index from phase-shift terrestrial laser scanning. *Agricultural and Forest Meteorology*, *280*, 107766. https://doi.org/10.1016/j.agrformet.2019.107766

Grünewald, T., & Lehning, M. (2015). Are flat-field snow depth measurements representative? A comparison of selected index sites with areal snow depth measurements at the small catchment scale. *Hydrological Processes*, *29*(7), 1717–1728. https://doi.org/10.1002/hyp.10295

Hancock, S., Anderson, K., Disney, M., & Gaston, K. J. (2017). Measurement of fine-spatial-resolution 3D vegetation structure with airborne waveform lidar: Calibration and validation with voxelised terrestrial lidar. *Remote Sensing of Environment*, *188*, 37–50. https://doi.org/10.1016/j.rse.2016.10.041

Harder, P., Pomeroy, J. W., Helgason, W. D., & Helgason, W. D. (2020). Improving sub-canopy snow depth mapping with unmanned aerial vehicles: Lidar versus structure-from-motion techniques. *Cryosphere*, *14*(6), 1919–1935. https://doi.org/10.5194/tc-14-1919-2020

Harding, D. J., Lefsky, M. A., Parker, G. G., & Blair, J. B. (2001). Laser altimeter canopy height profiles methods and validation for closed-canopy, broadleaf forests. *Remote Sensing of Environment*, *76*(3), 283–297. https://doi.org/10.1016/S0034-4257(00)00210-8

Harestad, A. S., & Bunnell, F. L. (1981). Prediction of snow-water equivalents in coniferous forests. *Canadian Journal of Forest Research*, *11*(4), 854–857. https://doi.org/10.1139/x81-

126
Harpold, A. A., Biederman, J. A., Condon, K., Merino, M., Korgaonkar, Y., Nan, T., … Brooks, P. D. (2014). Changes in snow accumulation and ablation following the Las Conchas Forest Fire, New Mexico, USA. *Ecohydrology*, *7*(2), 440–452. https://doi.org/10.1002/eco.1363
Harpold, A. A., Krogh, S. A., Kohler, M., Eckberg, D., Greenberg, J., Sterle, G., & Broxton, P. D. (2020). Increasing the efficacy of forest thinning for snow using high-resolution modeling: A proof of concept in the Lake Tahoe Basin, California, USA. *Ecohydrology*, *13*(4). https://doi.org/10.1002/eco.2203
Hedstrom, N. R., & Pomeroy, J. W. (1998). Measurements and modelling of snow interception in the boreal forest. *Hydrological Processes*, *12*(10), 1611–1625. https://doi.org/10.1002/(SICI)1099-1085(199808/09)12:10/11<1611::AID-HYP684>3.0.CO;2-4
Helbig, N., Moeser, D., Teich, M., Vincent, L., Lejeune, Y., Sicart, J. E., & Monnet, J. M. (2020). Snow processes in mountain forests: Interception modeling for coarse-scale applications. *Hydrology and Earth System Sciences*, *24*(5), 2545–2560. https://doi.org/10.5194/hess-24-2545-2020
Hopkinson, C., & Chasmer, L. (2009). Testing LiDAR models of fractional cover across multiple forest ecozones. *Remote Sensing of Environment*, *113*(1), 275–288. https://doi.org/10.1016/j.rse.2008.09.012
Hopkinson, C., Chasmer, L. E., Sass, G., Creed, I. F., Sitar, M., Kalbfleisch, W., & Treitz, P. (2005). Vegetation class dependent errors in lidar ground elevation and canopy height estimates in a boreal wetland environment. *Canadian Journal of Remote Sensing*, *31*(2), 191–206. https://doi.org/10.5589/m05-007
Hovi, A., Liang, J., Korhonen, L., Kobayashi, H., & Rautiainen, M. (2016). Quantifying the missing link between forest albedo and productivity in the boreal zone. *Biogeosciences*, *13*(21), 6015–6030. https://doi.org/10.5194/bg-13-6015-2016
Huerta, M. L., Molotch, N. P., & McPhee, J. (2019). Snowfall interception in a deciduous Nothofagus forest and implications for spatial snowpack distribution. *Hydrological Processes*, *33*(13), 1818–1834. https://doi.org/10.1002/hyp.13439
Isenburg, M. (2020). *LAStools*. Retrieved from https://rapidlasso.com/lastools/
Jiao-jun, Z., Xiu-fen, L., Yutaka, G., & Takeshi, M. (2004). Wind profiles in and over trees. *Journal of Forestry Research*, *15*(4), 305–312. https://doi.org/10.1007/bf02844959
Johnston, L. M., Wang, X., Erni, S., Taylor, S. W., McFayden, C. B., Oliver, J. A., … Flannigan, M. D. (2020). Wildland fire risk research in Canada. *Environmental Reviews*, *28*(2), 164–186. https://doi.org/10.1139/er-2019-0046
Khosravipour, A., Skidmore, A. K., & Isenburg, M. (2016). Generating spike-free digital surface models using LiDAR raw point clouds: A new approach for forestry applications. *International Journal of Applied Earth Observation and Geoinformation*, *52*(June), 104–114. https://doi.org/10.1016/j.jag.2016.06.005
Kobayashi, D. (1987). Snow accumulation on a narrow board. *Cold Regions Science and Technology*, *13*(3), 239–245. https://doi.org/10.1016/0165-232X(87)90005-X
Landsberg, J. J., & James, G. B. (1971). Wind Profiles in Plant Canopies: Studies on an Analytical Model. *The Journal of Applied Ecology*, *8*(3), 729. https://doi.org/10.2307/2402680
Li-Cor. (1992). *LAI-2000 plant canopy analyzer - Operating manual*. LI-COR, Inc.
Liu, J., Skidmore, A. K., Jones, S., Wang, T., Heurich, M., Zhu, X., & Shi, Y. (2018). Large off-

nadir scan angle of airborne LiDAR can severely affect the estimates of forest structure metrics. *ISPRS Journal of Photogrammetry and Remote Sensing*, *136*, 13–25. https://doi.org/10.1016/j.isprsjprs.2017.12.004

Lundberg, A., Calder, I., & Harding, R. (1998). Evaporation of intercepted snow: measurement and modelling. *Journal of Hydrology*, *206*(3–4), 151–163. https://doi.org/10.1016/S0022-1694(97)00016-4

Lundberg, A., & Halldin, S. (2001). Snow interception evaporation. Review of measurementtechniques, processes, and models. *Theoretical and Applied Climatology*, *70*(1–4), 117–133. https://doi.org/10.1007/s007040170010

Lundberg, A., & Koivusalo, H. (2003). Estimating winter evaporation in boreal forests with operational snow course data. *Hydrological Processes*, *17*(8), 1479–1493. https://doi.org/10.1002/hyp.1179

Lv, Z., & Pomeroy, J. W. (2019). Detecting intercepted snow on mountain needleleaf forest canopies using satellite remote sensing. *Remote Sensing of Environment*, *231*(March), 111222. https://doi.org/10.1016/j.rse.2019.111222

Lv, Z., & Pomeroy, J. W. (2020). Assimilating snow observations to snow interception process simulations. *Hydrological Processes*, *34*(10), 2229–2246. https://doi.org/10.1002/hyp.13720

Ma, L., Zheng, G., Eitel, J. U. H., Magney, T. S., & Moskal, L. M. (2017). Retrieving forest canopy extinction coefficient from terrestrial and airborne lidar. *Agricultural and Forest Meteorology*, *236*, 1–21. https://doi.org/10.1016/j.agrformet.2017.01.004

Mazzotti, G., Currier, W. R., Deems, J. S., Pflug, J. M., Lundquist, J. D., & Jonas, T. (2019). Revisiting Snow Cover Variability and Canopy Structure Within Forest Stands: Insights From Airborne Lidar Data. *Water Resources Research*, 2019WR024898. https://doi.org/10.1029/2019WR024898

Mazzotti, G., Essery, R., Moeser, C. D., & Jonas, T. (2020). Resolving Small-Scale Forest Snow Patterns Using an Energy Balance Snow Model With a One-Layer Canopy. *Water Resources Research*, *56*(1). https://doi.org/10.1029/2019WR026129

Miller, D. H. (1964). Interception Processes During Snowstorms. In *US Forest Service Research Paper PSW-RP-18*.

Miller, J. B. (1967). A formula for average foliage density. *Australian Journal of Botany*, *15*(1), 141–144. https://doi.org/10.1071/BT9670141

Miralles, D. G., Gash, J. H., Holmes, T. R. H., De Jeu, R. A. M., & Dolman, A. J. (2010). Global canopy interception from satellite observations. *Journal of Geophysical Research Atmospheres*, *115*(16), 1–8. https://doi.org/10.1029/2009JD013530

Moeser, D., Mazzotti, G., Helbig, N., & Jonas, T. (2016). Representing spatial variability of forest snow: Implementation of a new interception model. *Water Resources Research*, 1208–1226. https://doi.org/10.1002/2015WR017961

Moeser, D., Morsdorf, F., & Jonas, T. (2015). Novel forest structure metrics from airborne LiDAR data for improved snow interception estimation. *Agricultural and Forest Meteorology*, *208*, 40–49. https://doi.org/10.1016/j.agrformet.2015.04.013

Moeser, D., Roubinek, J., Schleppi, P., Morsdorf, F., & Jonas, T. (2014). Canopy closure, LAI and radiation transfer from airborne LiDAR synthetic images. *Agricultural and Forest Meteorology*, *197*, 158–168. https://doi.org/10.1016/j.agrformet.2014.06.008

Moeser, D., Stähli, M., & Jonas, T. (2015). Improved snow interception modeling using canopy parameters derived from airborne LiDAR data. *Water Resources Research*, *51*(7), 5041–

5059. https://doi.org/10.1002/2014WR016724
Molotch, N. P., Blanken, P. D., Williams, M. W., Turnipseed, A. A., Monson, R. K., & Margulis, S. A. (2007). Estimating sublimation of intercepted and sub-canopy snow using eddy covariance systems. *Hydrological Processes*, *21*(12), 1567–1575. https://doi.org/10.1002/hyp.6719
Musselman, K. N., Molotch, N. P., & Brooks, P. D. (2008). Effects of vegetation on snow accumulation and ablation in a mid-latitude sub-alpine forest. *Hydrological Processes*, *22*(15), 2767–2776. https://doi.org/10.1002/hyp.7050
Musselman, K. N., Pomeroy, J. W., & Link, T. E. (2015). Variability in shortwave irradiance caused by forest gaps: Measurements, modelling, and implications for snow energetics. *Agricultural and Forest Meteorology*, *207*, 69–82. https://doi.org/10.1016/j.agrformet.2015.03.014
Natural Resources Canada. (2021). Precise Point Positioning. Retrieved July 8, 2021, from https://webapp.geod.nrcan.gc.ca/geod/tools-outils/ppp.php
Nemes, A., Dasari, T., Guala, M., Hong, J., & Coletti, F. (2017). Lagrangian trajectories and settling velocity of snowflakes: Observation of particle-turbulence dynamics. *10th International Symposium on Turbulence and Shear Flow Phenomena, TSFP 2017*, *3*.
Nijssen, B., & Lettenmaier, D. P. (1999). A simplified approach for predicting shortwave radiation transfer through boreal forest canopies. *Journal of Geophysical Research Atmospheres*, *104*(D22), 27859–27868. https://doi.org/10.1029/1999JD900377
Nilson, T. (1971). A theoretical analysis of the frequency of gaps in plant stands. *Agricultural Meteorology*, *8*(1966), 25–38. https://doi.org/10.1016/0002-1571(71)90092-6
Nyquist, H. (1928). Certain Topics in Telegraph Transmission Theory. *Transactions of the American Institute of Electrical Engineers*, *47*(2), 617–644. https://doi.org/10.1109/T-AIEE.1928.5055024
Parviainen, J., & Pomeroy, J. W. (2000). Multiple-scale modelling of forest snow sublimation: initial findings. *Hydrological Processes*, *14*(15), 2669–2681. https://doi.org/10.1002/1099-1085(20001030)14:15<2669::AID-HYP85>3.0.CO;2-Q
Peters-Lidard, C. D., Clark, M., Samaniego, L., Verhoest, N. E. C., Van Emmerik, T., Uijlenhoet, R., … Woods, R. (2017). Scaling, similarity, and the fourth paradigm for hydrology. *Hydrology and Earth System Sciences*, *21*(7), 3701–3713. https://doi.org/10.5194/hess-21-3701-2017
Pfister, R., & Schneebeli, M. (1999). Snow accumulation on boards of different sizes and shapes. *Hydrological Processes*, *13*(14–15), 2345–2355. https://doi.org/10.1002/(SICI)1099-1085(199910)13:14/15<2345::AID-HYP873>3.0.CO;2-N
Pomeroy, & Goodison, B. (1997). Winter and snow. In *The Surface Climates of Canada* (pp. 68–100). Retrieved from http://www.jstor.org/stable/j.ctt7zmr8
Pomeroy, & Gray, D. M. (1995). *Snowcover: Accumulation, Relocation and Management* (NHRI Scien). Saskatoon: Environment Canada.
Pomeroy, J. W., Fang, X., & Ellis, C. (2012). Sensitivity of snowmelt hydrology in Marmot Creek, Alberta, to forest cover disturbance. *Hydrological Processes*, *26*(12), 1892–1905. https://doi.org/10.1002/hyp.9248
Pomeroy, J. W., & Gray, D. M. (1990). Saltation of snow. *Water Resources Research*, *26*(7), 1583–1594. https://doi.org/10.1029/90WR00006
Pomeroy, J. W., Gray, D. M., Hedstrom, N. R., & Janowicz, J. R. (2002). Prediction of seasonal snow accumulation in cold climate forests. *Hydrological Processes*, *16*(18), 3543–3558.

https://doi.org/10.1002/hyp.1228
Pomeroy, J. W., Gray, D. M., Shook, K. R., Toth, B., Essery, R. L. H., Pietroniro, A., & Hedstrom, N. (1998). An evaluation of snow accumulation and ablation processes for land surface modelling. *Hydrological Processes*, *12*(15), 2339–2367. https://doi.org/10.1002/(SICI)1099-1085(199812)12:15<2339::AID-HYP800>3.0.CO;2-L
Pomeroy, J. W., Parviainen, J., Hedstrom, N., & Gray, D. M. (1998). Coupled modelling of forest snow interception and sublimation. *Hydrological Processes*, *12*(15), 2317–2337. https://doi.org/10.1002/(SICI)1099-1085(199812)12:15<2317::AID-HYP799>3.0.CO;2-X
Pomeroy, & Schmidt, R. A. (1993). The Use of Fractal Geometry in Modelling Intercepted Snow Accumulation and Sublimation. *50th Annual Eastern Snow Conference*, 231–239. Quebec City.
Ross, J. (1981). *The radiation regime and architecture of plant stands*. The Hague: Dr. W. Junk Publishers.
Roth, T. R., & Nolin, A. W. (2019). Characterizing maritime snow canopy interception in forested mountains. *Water Resources Research*. https://doi.org/10.1029/2018WR024089
Rothwell, R., Hillman, G., & Pomeroy, J. W. (2016). Marmot Creek Experimental Watershed Study. *The Forestry Chronicle*, *92*, 32–36. https://doi.org/10.5558/tfc2016-010
Rutter, N., Essery, R., Pomeroy, J. W., Altimir, N., Andreadis, K., Baker, I., … Yamazaki, T. (2009). Evaluation of forest snow processes models (SnowMIP2). *Journal of Geophysical Research Atmospheres*, *114*(6). https://doi.org/10.1029/2008JD011063
Ryan, W. A., Doesken, N. J., & Fassnacht, S. R. (2008). Preliminary results of ultrasonic snow depth sensor testing for National Weather Service (NWS) snow measurements in the US. *Hydrological Processes*, *22*(15), 2748–2757. https://doi.org/10.1002/hyp.7065
Satterlund, D. R., & Haupt, H. F. (1967). Snow catch by Contier Crowns. *Water Resources Research*, *3*(4), 1035–1039. https://doi.org/10.1029/WR003i004p01035
Schleppi, P., Conedera, M., Sedivy, I., & Thimonier, A. (2007). Correcting non-linearity and slope effects in the estimation of the leaf area index of forests from hemispherical photographs. *Agricultural and Forest Meteorology*, *144*(3–4), 236–242. https://doi.org/10.1016/j.agrformet.2007.02.004
Schmidt, R. A., & Gluns, D. R. (1991). Snowfall interception on branches of three conifer species. *Canadian Journal of Forest Research*, *21*(8), 1262–1269. https://doi.org/10.1139/x91-176
Schmidt, R. A., & Pomeroy, J. W. (1990). Bending of a conifer branch at subfreezing temperatures: implications for snow interception. *Canadian Journal of Forest Research*, *20*(8), 1251–1253. https://doi.org/10.1139/x90-165
Sellers, P. J., Hall, F. G., Kelly, R. D., Black, A., Baldocchi, D., Berry, J., … Guertin, F. E. (1997). BOREAS in 1997: Experiment overview, scientific results, and future directions. *Journal of Geophysical Research: Atmospheres*, *102*(D24), 28731–28769. https://doi.org/10.1029/97JD03300
Shook, K. R., & Gray, D. M. (1994). Determining the snow water equivalent of shallow prairie snowcovers. *Proc. 51st Eastern Snow Conference*, 89–95.
Shook, K. R., & Gray, D. M. (1997). Synthesizing shallow seasonal snow covers. *Water Resources Research*, *33*(3), 419–426. https://doi.org/10.1029/96WR03532
Smith, C. D. (2007). Correcting the wind bias in snowfall measurements made with a Geonor T-200B precipitation gauge and alter wind shield. *87th American Meteorology Society Annual Meeting*. San Antonio, TX.

Solberg, S., Næsset, E., Hanssen, K. H., & Christiansen, E. (2006). Mapping defoliation during a severe insect attack on Scots pine using airborne laser scanning. *Remote Sensing of Environment*, *102*(3–4), 364–376. https://doi.org/10.1016/j.rse.2006.03.001

Stenberg, P., Linder, S., Smolander, H., & Flower-Ellis, J. (1994). Performance of the LAI-2000 plant canopy analyzer in estimating leaf area index of some Scots pine stands. *Tree Physiology*, *14*(7-8–9), 981–995. https://doi.org/10.1093/treephys/14.7-8-9.981

Storck, P. (2000). *Trees, snow and flooding: an investigation of forest canopy effects on snow accumulation and melt at the plot and watershed scales in the pacific northwest*. University of Washington.

Sturm, M. (1992). Snow Distribution and Heat Flow in the Taiga. *Arctic and Alpine Research*, *24*(2), 145. https://doi.org/10.2307/1551534

Thimonier, A., Sedivy, I., & Schleppi, P. (2010). Estimating leaf area index in different types of mature forest stands in Switzerland: A comparison of methods. *European Journal of Forest Research*, *129*(4), 543–562. https://doi.org/10.1007/s10342-009-0353-8

Troendle, C. A., & Leaf, C. F. (1980). Effects of timber harvest in the snow zone on volume and timing of water yield. *Interior West Watershed Management*, 231–243.

Trujillo, E., Molotch, N. P., Goulden, M. L., Kelly, A. E., & Bales, R. C. (2012). Elevation-dependent influence of snow accumulation on forest greening. *Nature Geoscience*, *5*(10), 705–709. https://doi.org/10.1038/ngeo1571

Trujillo, E., Ramírez, J. A., & Elder, K. J. (2007). Topographic, meteorologic, and canopy controls on the scaling characteristics of the spatial distribution of snow depth fields. *Water Resources Research*, *43*(7). https://doi.org/10.1029/2006WR005317

Varhola, A., & Coops, N. C. (2013). Estimation of watershed-level distributed forest structure metrics relevant to hydrologic modeling using LiDAR and Landsat. *Journal of Hydrology*, *487*, 70–86. https://doi.org/10.1016/j.jhydrol.2013.02.032

Varhola, A., Coops, N. C., Weiler, M., & Moore, R. D. (2010). Forest canopy effects on snow accumulation and ablation: An integrative review of empirical results. *Journal of Hydrology*, *392*(3–4), 219–233. https://doi.org/10.1016/j.jhydrol.2010.08.009

Varhola, A., Frazer, G. W., Teti, P., & Coops, N. C. (2012). Estimation of forest structure metrics relevant to hydrologic modelling using coordinate transformation of airborne laser scanning data. *Hydrology and Earth System Sciences*, *16*(10), 3749–3766. https://doi.org/10.5194/hess-16-3749-2012

Volney, W. J. A., & Fleming, R. A. (2000). Climate change and impacts of boreal forest insects. *Agriculture, Ecosystems and Environment*, *82*(1–3), 283–294. https://doi.org/10.1016/S0167-8809(00)00232-2

Wallace, L., Lucieer, A., Watson, C., & Turner, D. (2012). Development of a UAV-LiDAR System with Application to Forest Inventory. *Remote Sensing*, *4*(6), 1519–1543. https://doi.org/10.3390/rs4061519

Webster, C. (2017). *Measurement and modelling of sub-canopy radiation to seasonal snow in alpine forests*. University of Northumbria.

Webster, C., & Jonas, T. (2018). Influence of canopy shading and snow coverage on effective albedo in a snow-dominated evergreen needleleaf forest. *Remote Sensing of Environment*, *214*(May), 48–58. https://doi.org/10.1016/j.rse.2018.05.023

Webster, C., Mazzotti, G., Essery, R., & Jonas, T. (2020). Enhancing airborne LiDAR data for improved forest structure representation in shortwave transmission models. *Remote Sensing of Environment*, *249*(July), 112017. https://doi.org/10.1016/j.rse.2020.112017

Westling, F., Mahmud, K., Underwood, J., & Bally, I. (2020). Replacing traditional light measurement with LiDAR based methods in orchards. *Computers and Electronics in Agriculture*, *179*(September), 105798. https://doi.org/10.1016/j.compag.2020.105798

Wright, & Nocedal. (1999). *Numerical Optimization* (J. Nocedal & S. J. Wright, Eds.). https://doi.org/10.1007/b98874

Wulder, M. A., White, J. C., Nelson, R. F., Næsset, E., Ørka, H. O., Coops, N. C., … Gobakken, T. (2012). Lidar sampling for large-area forest characterization: A review. *Remote Sensing of Environment*, *121*, 196–209. https://doi.org/10.1016/j.rse.2012.02.001

Yan, G., Hu, R., Luo, J., Weiss, M., Jiang, H., Mu, X., … Zhang, W. (2019). Review of indirect optical measurements of leaf area index: Recent advances, challenges, and perspectives. *Agricultural and Forest Meteorology*, *265*(March 2018), 390–411. https://doi.org/10.1016/j.agrformet.2018.11.033

Zhao, K., & Popescu, S. (2009). Lidar-based mapping of leaf area index and its use for validating GLOBCARBON satellite LAI product in a temperate forest of the southern USA. *Remote Sensing of Environment*, *113*(8), 1628–1645. https://doi.org/10.1016/j.rse.2009.03.006

Zheng, Z., Kirchner, P. B., & Bales, R. C. (2015). Orographic and vegetation effects on snow accumulation in the southern Sierra Nevada: A statistical summary from LiDAR data. *Cryosphere Discussions*, *9*(4), 4377–4405. https://doi.org/10.5194/tcd-9-4377-2015

Appendices

Appendix A: Surveys beyond study period

A total of six UAV surveys were collected at the field site over the 2018-2019 winter season, with accompanying snow surveys when snow was present on the ground. Once the field season was finished, the study period was established to focus on observations which would best inform the research questions. As a result, two of the field surveys fell outside of the study period and are reported in Table A.1: . Those within the study period, as well as the snow-free survey are reported in Table 2.1.

Table A.1: Snow survey observations for two dates lying outside of the study period.

Date	DOY	UAV survey end time	Clearing precip. gauge SWE [mm]	Clearing SR50 HS [m]	Forest SR50 HS [m]	Clearing snow density intercept b_c [kg m^{-3}]	Clearing snow density slope m_c [kg m^{-4}]	Forest snow density constant ρ_f [kg m^{-3}]
2019-04-17	107	11:02	223.52	0.263	0.326	263	0.982	263
2019-05-03	123	11:12	280.33	0.168	0.365	255	0.735	291

The additional surveys shown in Table A.1: resulted in two additional date intervals which fell outside of the study period, shown in Table A.2: . The intervals within the study period are reported in Table 2.2.

Table A.2: Interval dates and corresponding snow observations for two intervals lying outside of the study period.

Date interval	DOY interval	UC Geonore ΔSWE [mm]	UC SR50 ΔHS [m]	UF SR50 ΔHS [m]
2019-02-21 to 2019-04-17	052-107	36.3692	-0.421	-0.08
2019-04-17 to 2019-05-03	107-123	56.8078	-0.095	0.039

Appendix B: Validation of lidar snow depth, density, and SWE estimates

Lidar snow depth products (HS_{lidar}) were compared with georeferenced manual snow depth samples from snow surveys to assess for systematic bias due to georeferencing of the GNSS base station (Figure B.1). Snow depth biases were all negative and were found to vary with the spatial resolution of HS_{lidar}. All snow depth products were subsequently bias-corrected using the mean bias of the 5 cm resolution product for the corresponding survey day, with final errors reported in Figure B.2.

Significant linear relationships between snow depth and density were observed among snow survey observations within the clearing for 19 Feb. (n = 10, p-value = 0.0122) and 21 Feb. (n = 10, p-value = 0.00224), but was nonsignificant for 14 Feb. (n = 9, p-value = 0.112). Within the forest, all linear relationships between depth and density were nonsignificant: 14 Feb. (n = 0, p-value = NA), 19 Feb. (n = 6, p-value = 0.404), and 21 Feb. (n = 7, p-value = 0.232). Linear depth-density models were used within the clearing for all three days, while constant density models were used within the forest (Figure B.3). SWE samples within the forest were limited due to thin snowpack which was often below the 20 cm depth cut-off used for quality control. No snow survey observations within the forest on 14 Feb. (19_045) passed quality-control. Instead, snow density for this day was estimated as 165 kg m^{-3} by interpolating forest snow densities in time from previous and subsequent snow surveys. Resulting lidar SWE errors are reported in Figure B.4.

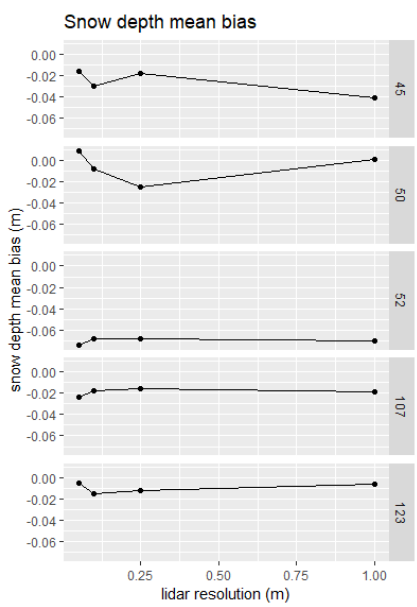

Figure B.1: Lidar snow depth bias with manual snow depth measurements for each Julian day (45, 50, …).

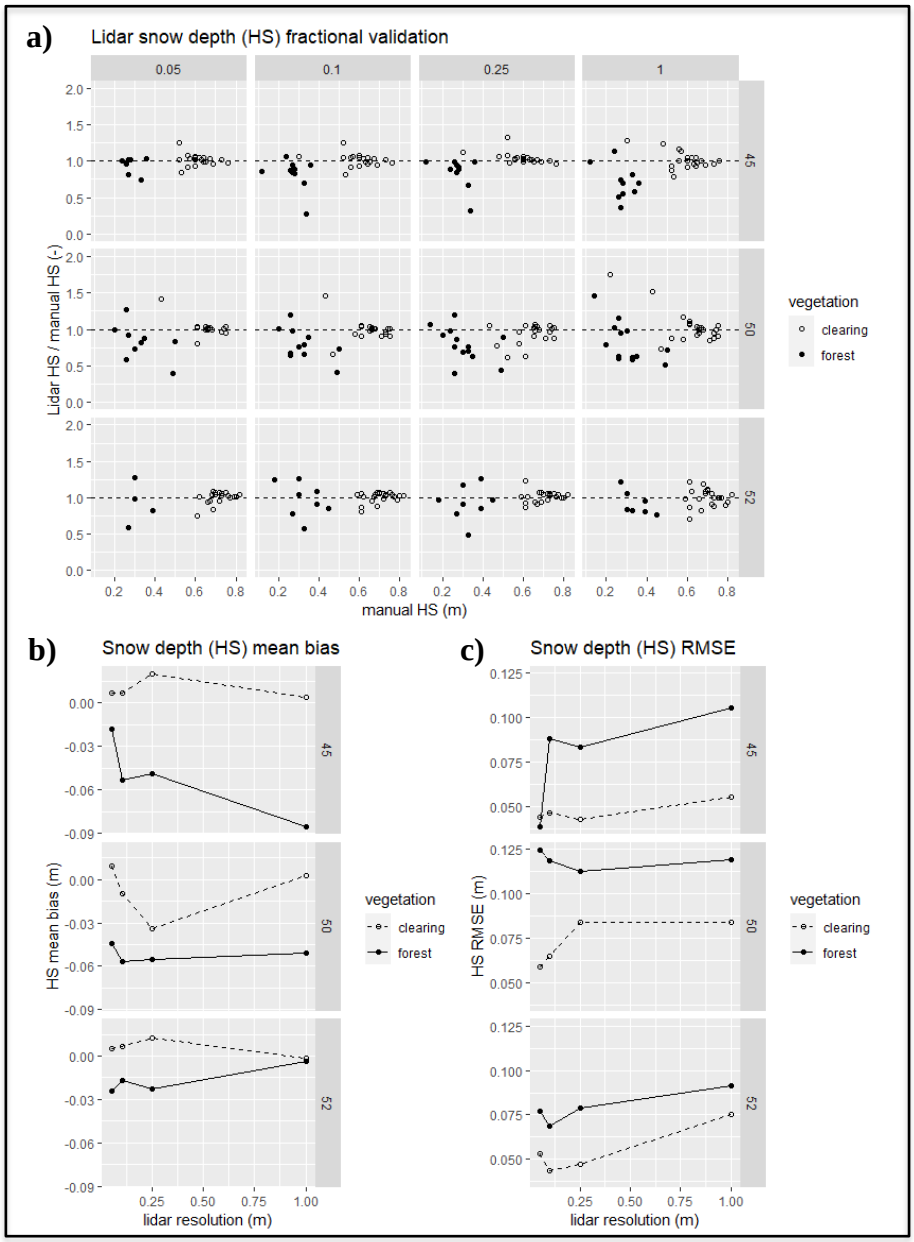

Figure B.2: Lidar snow depth validation with snow survey observations: (a) fractional error, (b) mean bias, and (c) root mean squared error (RMSE), after correction for mean bias of snow depth, for each Julian day within the study period (45, 50, 52).

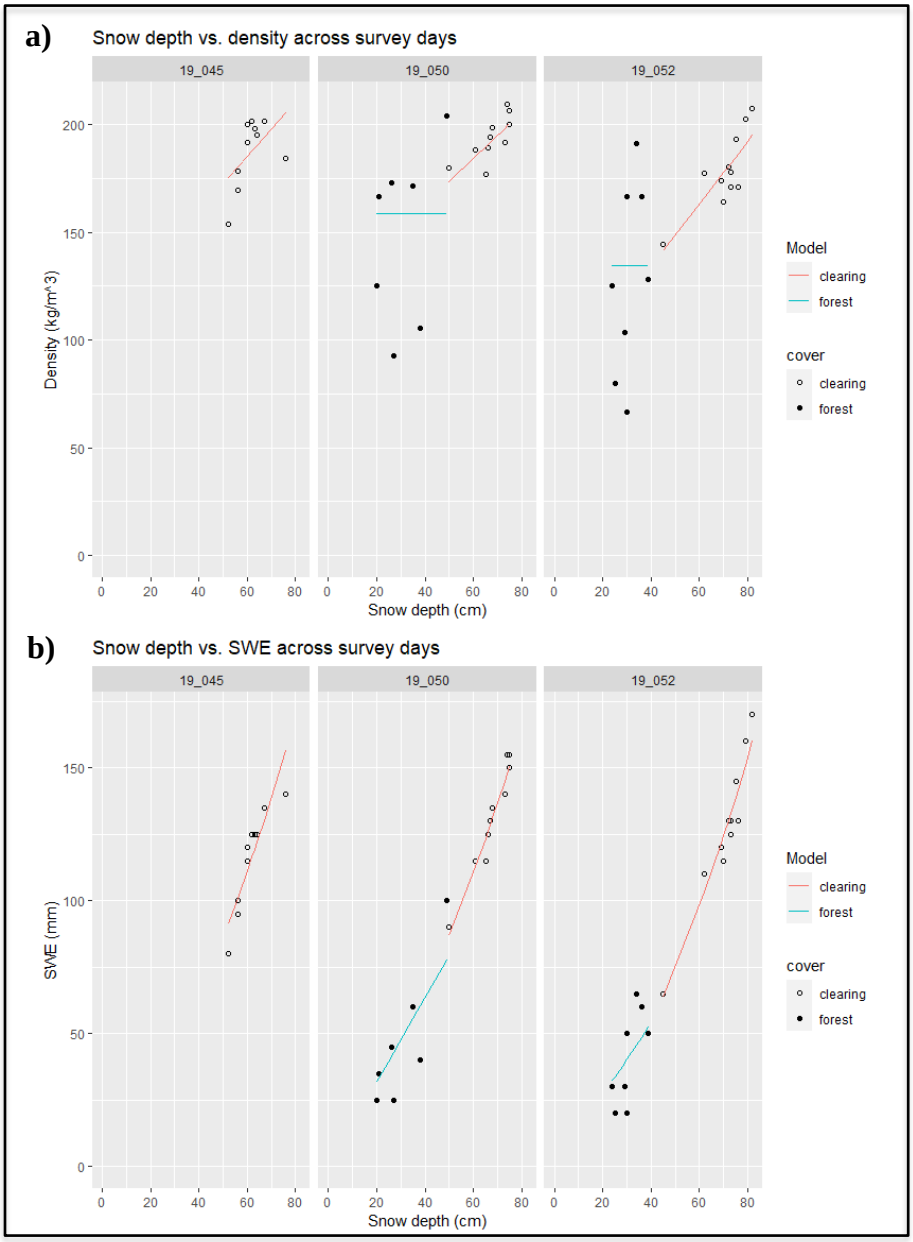

Figure B.3: (a) Snow depth vs. density and (b) Snow depth vs. SWE from snow survey observations for each day, plotted with corresponding density models (Model parameters are reported in Table 2.1).

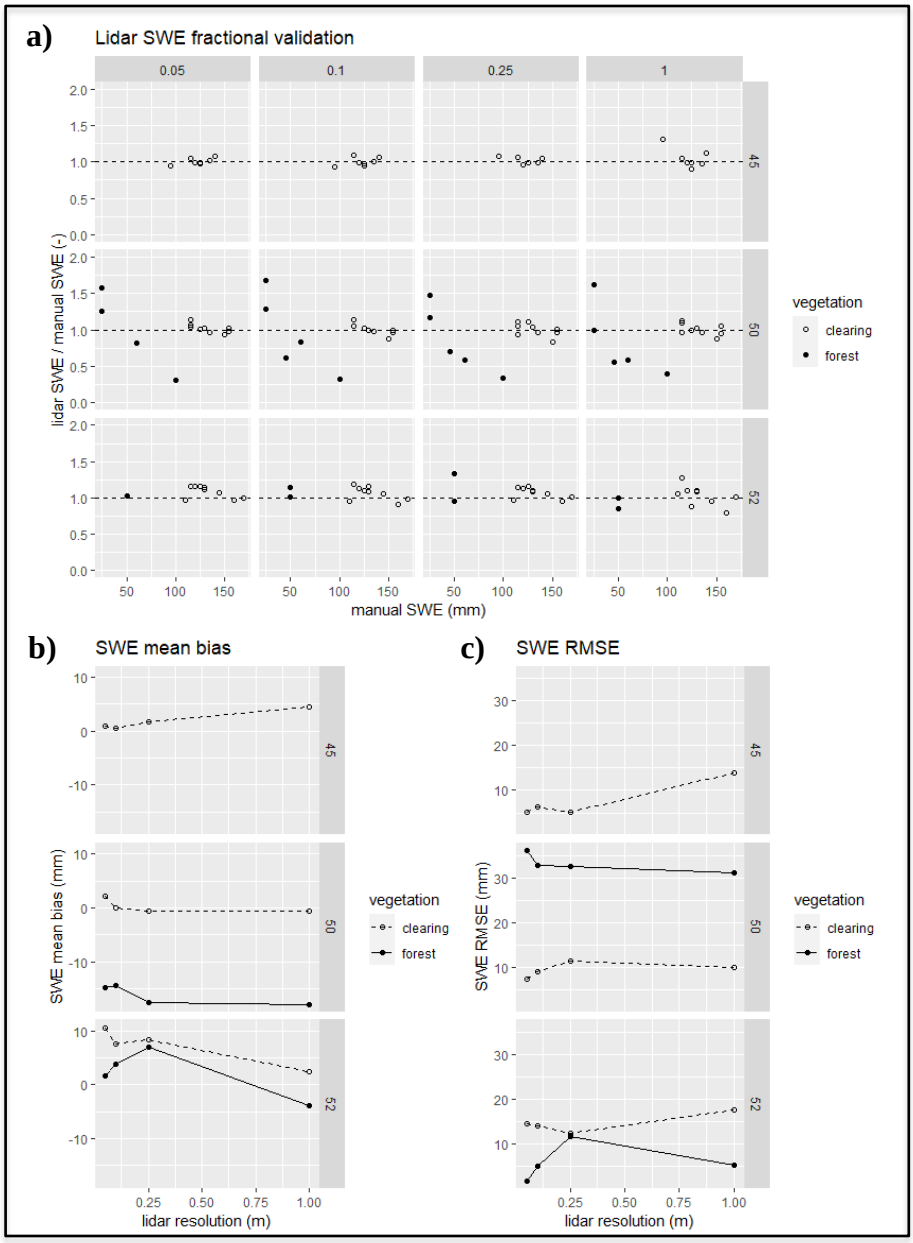

Figure B.4: Lidar SWE estimated using the Hedstrom-Pomeroy (1998) fresh snow density assumption compared with snow survey observations: (a) fractional error, (b) mean bias, and (c) root mean squared error (RMSE)

Appendix C: Optimization of light transmittance from lidar point cloud reprojection

Synthetic hemispherical images were generated by hemispherical reprojection of the lidar return point cloud generated from observations of the canopy under snow-off conditions, following (Moeser et al., 2014). All images were produced with dimensions were 10 inches by 10 inches with 100 pixels per inch for a total of 1000 pixels by 1000 pixels squared. Plotted point area a_p [pixels^2] was related to distance form the origin r [m] by:

$$a_p = \frac{c^2 \cdot \langle f \rangle^2 \cdot s}{r^2} \qquad \text{Eq. 6.1}$$

where c = 3937 [pixels m^{-1}] is a unit length conversion, ⟨f⟩ = 0.15 [m] is an estimate of the diameter of the lidar footprint intersecting the canopy, and s is the point size scalar which is determined by optimization. This is equivalent to a first-order approximation of point radius related to the arctangent of the inverse of distance from origin, following the geometrical model of a 2-dimensional projection of uniform spheres in 3-dimensional space. Four light transmittance estimates were calculated from each synthetic hemispherical image corresponding to each of the 15° analysis bands ranging from 0° to 60° from zenith, with error metrics weighted by solid angle of the corresponding ring. Solid-angle weighted root mean squared error (WRMSE) and solid-angle weighted mean bias (WMB) were calculated for light transmittance estimates from thresholded synthetic images compared with similar values from collocated thresholded hemispherical photography, for different values of point size scalar s (Figure C.1).

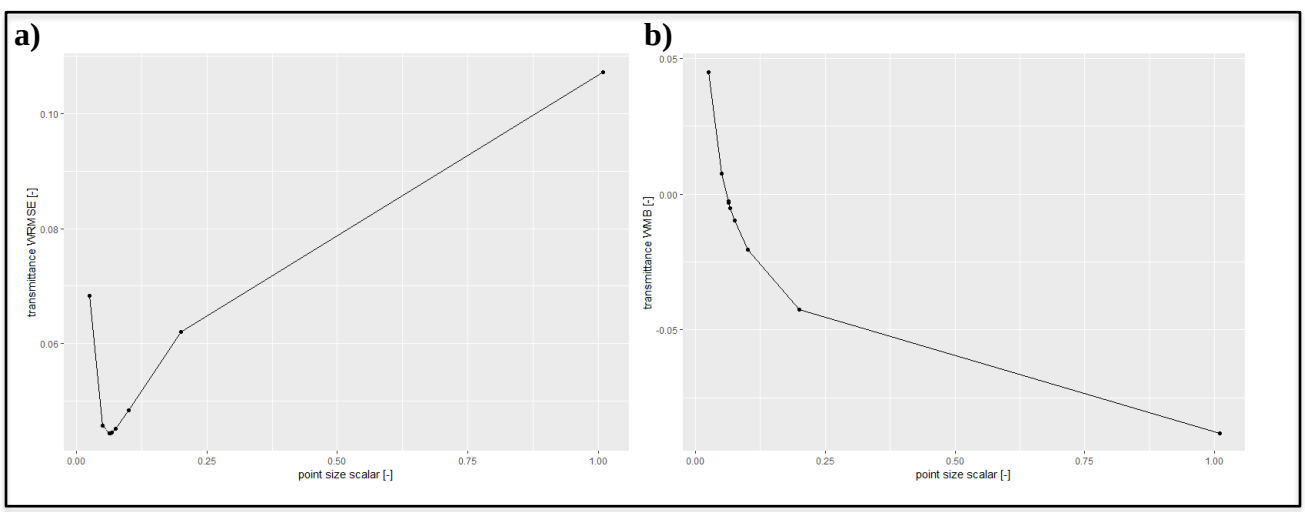

Figure C.1:(a) Weighted root mean squared error (WRMSE) and (b) weighted mean bias (WMB) of light transmittance calculated from synthetic hemispheres from lidar point cloud reprojection compared with values from corresponding hemispherical photographs taken below the canopy under snow-off canopy conditions (n = 15).

WRMSE was minimized at s = 0.063 and showed minimal bias for this optimized value (WRMSE = 0.0444, WMB= -2.70 x 10^{-3}, n=15). For this value of s, a lidar return 1 m away from the origin (or "viewpoint") was plotted with a diameter of 148 pixels corresponding to a 26.6° angular footprint, while a point 10 m away was plotted with a diameter of 14.8 pixels corresponding to a 2.66° angular footprint (e.g. Figure 3.3.c). Separate RMSE values for each of the four zenith angle bands are reported in Table 3.2 (see Figure C.2). A total of 1944 synthetic hemispheres were generated by point reprojection the snow-off lidar point cloud for a 1 m square lattice of viewpoints over the upper forest plot, using the optimized point size scalar value.

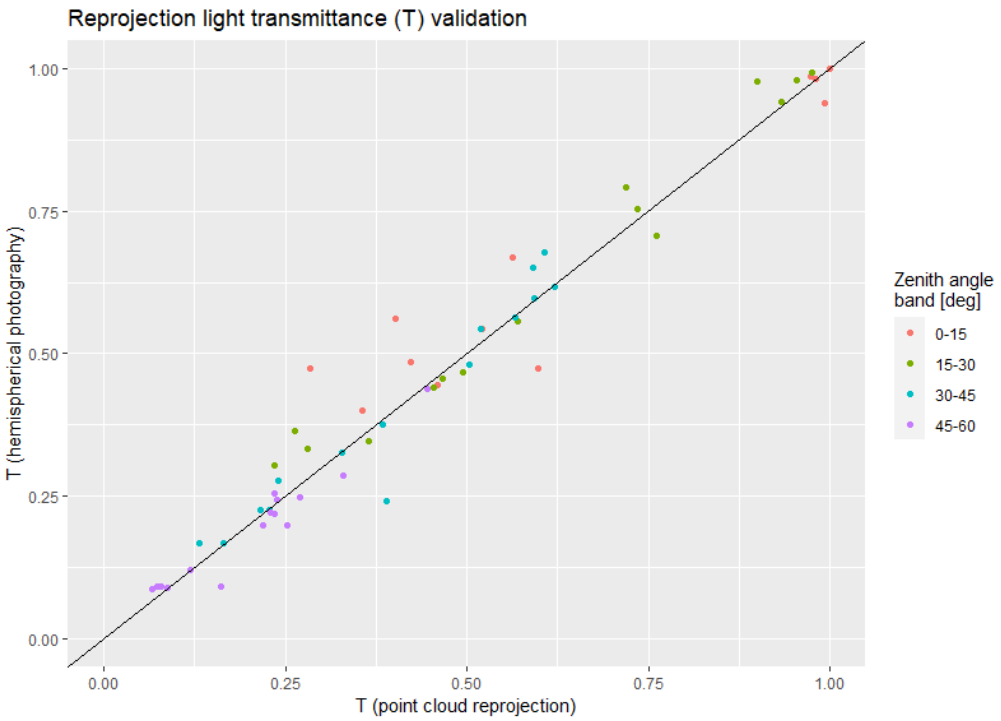

Figure C.2: Comparisons of band-wise light transmittance estimated from lidar point cloud reprojection (x-axis) with light transmittance estimated from thresholded hemispherical photography (y-axis) of the snow-off canopy, for the optimized point size scalar value of s = 0.063.

Appendix D: Parameter fitting of contact number correction factor ωc_χ for voxel ray sampling of lidar

Estimates of canopy contact number (χ) along rays through the forest canopy were estimated by lidar return estimates from voxel ray sampling of lidar, using a correction factor ωc_χ determined by least-squares regression with estimates from validating hemispherical photography. Contact number estimates were calculated separately for snow-on and snow-off canopy conditions, with separate validation sets of hemispherical photographs collected under each set of conditions. ωc_χ was determined for each case by minimizing the solid-angle-weighted root mean squared error (WRMSE) between mean zenith-angle band-wise transmittance from ray sampling (Eq. 2.19) and those from corresponding georeferenced and thresholded hemispherical photography (Figure D.1).

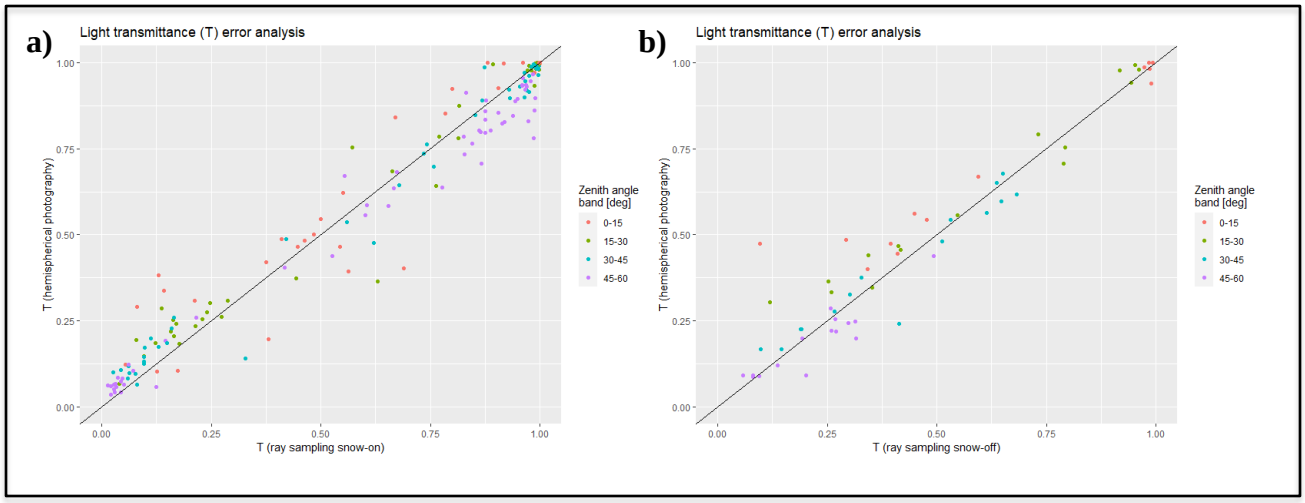

Figure D.1: Comparisons of band-wise light transmittance estimated by ray sampling (x-axis) with corresponding values from thresholded hemispherical photography (y-axis) for (a) snow-on and (b) snow-off canopy conditions.

For snow-on canopy conditions, WRMSE was minimized at ωc_χ = 0.372 and showed minimal bias (WRMSE = 0.0635, WMB= 7.27 x 10^{-3}, n=57). For snow-off canopy conditions, WRMSE was minimized at ωc_χ = 0.387 and showed minimal bias (WRMSE = 0.0663, WMB= 7.51 x 10^{-4}, n=15). The similar optimized correction factor values between snow-on and snow off conditions suggests that the presence of snow in the canopy does not greatly change the probability of a lidar return given a lidar sample which contacts the canopy. These results are generally expected with wavelength of the lidar laser beam, which may result in different relationships with reflectance of canopy and snow surfaces that were seen here. A total of 31,123 synthetic hemispheres with 1° angular resolution (or 25,445 angles each) were generated for each of the snow-on and snow-off canopy conditions over a 25 cm square lattice over the upper forest plot, using the optimized correction factor values.

Appendix E: Sensitivity analysis of band-wise ray sampled contact number

Sets of synthetic hemispheres generated from voxel ray sampling of lidar under slightly different assumptions were compared to assess for sensitivity of zenith-angle band-wise outputs to angular resolution, maximum distance, light transmittance thresholding, and commutation of mean and natural log functions. The results informed the choice of methods used for the analysis in this thesis and identifies some of the sensitivities that should be considered in future applications of these and related methods.

The sensitivity of zenith-angle band-wise contact number estimates to angular resolution of voxel ray sampling was assessed by comparing 181 x 181 hemispherical (or 1°) sample outputs with 1000 x 1000 hemispherical (or 0.18°) sample outputs, calculated separately for snow-on and snow-off canopy conditions using the same set of locations used for validation with hemispherical photography. Voxel ray sampling of lidar operates on approximately *O(n)* time for *n* samples within an image, such that the computation time of the 0.18° products was approximately 30x that of the corresponding 1° products.

Outputs aggregated over zenith-angle bands showed very close agreement (Figure E.1), with $R^2_{adj} > 0.9999$ for both snow on (n = 57) and snow-off (n = 15) conditions. No visual differences were seen among specific angle bands. This agreement suggested that band-wise estimates from 1° outputs were a good representation of the higher-resolutions products with a substantial reduction in computation time. Synthetic hemispheres from voxel ray sampling of lidar were therefore generated at 1° angular resolution for subsequent analysis.

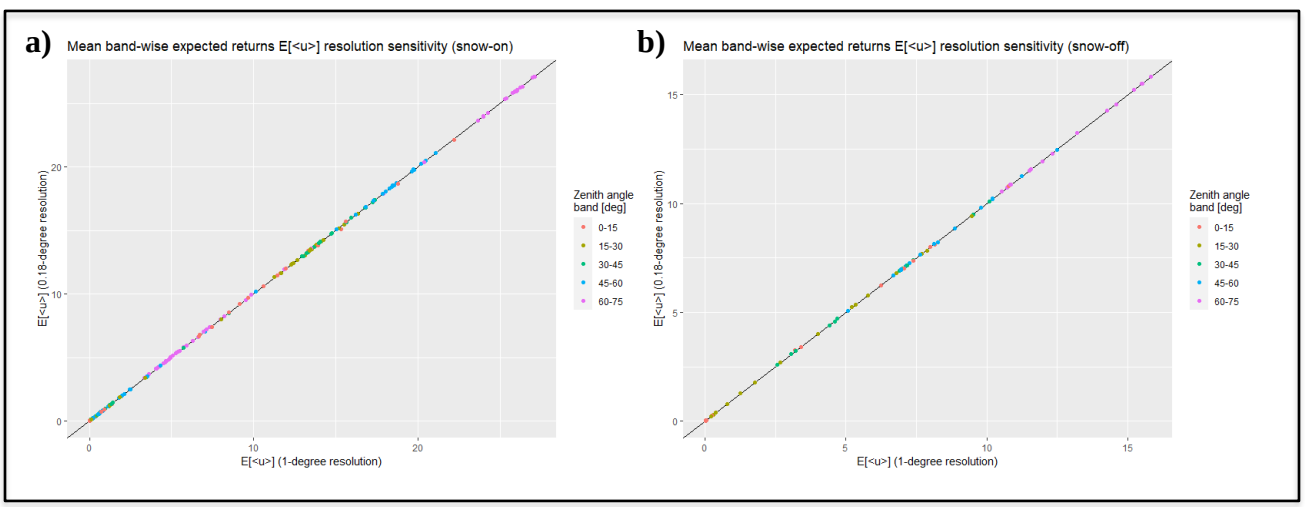

Figure E.1: Comparison of contact numbers by zenith angle bands calculated by voxel ray sampling of lidar at 1° (x-axis) vs. 0.18° (y-axis) angular resolutions over the upper hemisphere, for (a) snow-on and (b) snow-off canopy conditions.

Methods for generating synthetic hemispheres from both voxel ray sampling of lidar and point reprojection of lidar employ a “maximum distance” cut-off to focus computation efforts on the parts of the canopy which have the greatest influence on light regimes. Points in the point cloud beyond the maximum distance from the origin (or “viewpoint”) are dropped prior to generating the synthetic hemispheres. Sensitivity of band-wise contact number values to maximum distance primarily depends on the height of vegetation, and therefore was assessed for both methods using only outputs from voxel ray sampling of lidar. Sensitivity was assessed by comparing band-wise contact numbers from outputs with a 50 m maximum distance cut-off with those from outputs with a 150 m maximum distance, calculated separately for snow-on and snow-off canopy conditions using the same set of locations used for the validation with hemispherical photography. Voxel ray sampling of lidar operates on approximately $O(d^2)$ time for maximum distance d, such that the computation time of the 150 m products was approximately 9x that of the corresponding 50 m products. Random access memory storage also becomes a limitation for when increasing maximum distance cut-offs.

Outputs for the 60° - 75° zenith angle band showed visible bias in the 50 m products compared with the 150 m products for both snow-on and snow-off conditions (Figure E.1). Minimal bias was seen for the other four angle bands. Analysis was therefore limited to within 60° from vertical for analysis of synthetic hemispherical images where possible.

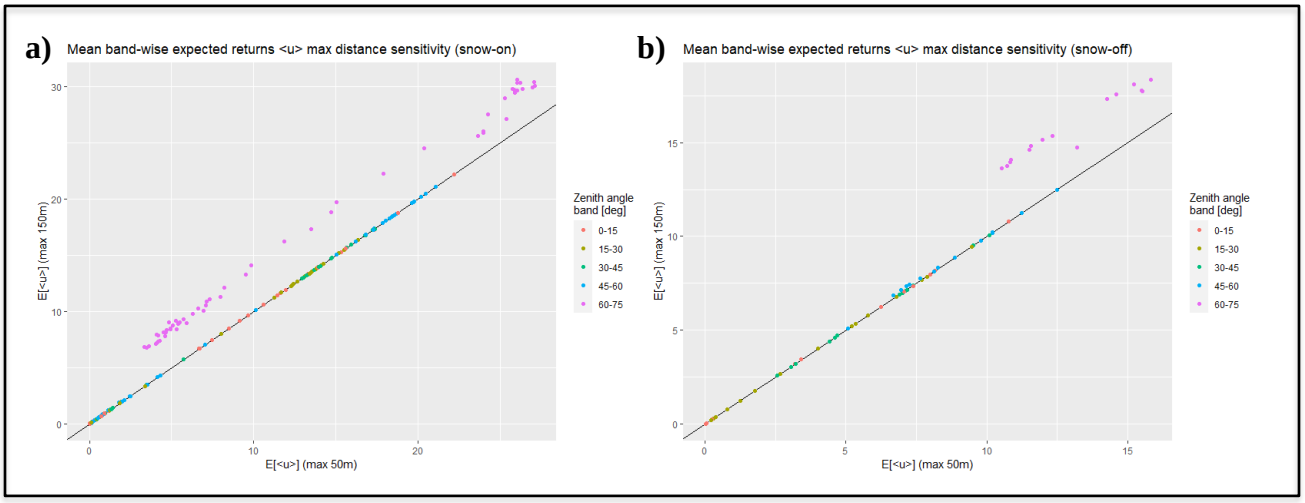

Figure E.2: Comparison contact numbers by zenith angle bands calculated by voxel ray sampling of lidar for rays up to a maximum distance of 50 m (x-axis) vs. 150 m (y-axis) from the origin, for (a) snow-on and (b) snow-off canopy conditions.

The effects of the thresholding assumption (Eq. 3.1) and commutation assumption (Eq. 3.2) were assessed using transmittances from voxel ray sampling of lidar. This type of analysis was not possible for synthetic hemispheres from point reprojection or hemispherical photography because the estimation of transmittances in these cases relies on these assumptions.

To examine the effects of the thresholding assumption on light transmittance metrics, solid-angle weighted band-wise means of light transmittance were calculated both directly from light transmittance over the hemisphere ($T^{\blacktriangle}_{a\text{-}b}$) and by first thresholding transmittances ($T^{\dagger}_{a\text{-}b}$) following Eq. 3.1, for each zenith angle band for each band a°-b°. (Schleppi et al., 2007). A transmittance threshold value of $T' = 0.772$ was used, taken from the mean threshold applied to hemispherical photography of the snow-off canopy to match the process used for analysis of hemispherical photography ($\gamma = 2.2$, Thimonier et al., 2010). Band-wise contact numbers ($\chi^{\blacktriangle}_{a\text{-}b}$) and band-wise thresholded contact numbers ($\chi^{\dagger}_{a\text{-}b}$) were then calculated from corresponding band-wise transmittances following Eq. 1.15. Both contact number calculations use the commutation assumption, discussed further on, the effects of which would be cancelled out if the error introduced by thresholding were negligible.

Visible discrepancies between band-wise contact numbers between these two methods suggests that the error introduced by the threshold assumption is not negligible (Figure E.3). Thresholding in this case results in an under-estimation of contact numbers compared with those calculated without thresholding. The errors are greater for angle bands with less transmittance (and greater contact number). These errors can be conceptually reproduced by considering a zenith-angle band with a homogenous transmittance less than the threshold but greater than 1. Selecting a different value of T' could result in less error overall, but likely would not address the spread of values due to error from thresholding. Selection of a better value of T' is also limited by not knowing true transmittances a priori, as is the case for analysis of binary hemispherical imagery.

To examine the effects of the commutation assumption, band-wise means of contact numbers ($\chi_{a\text{-}b}$) were compared with corresponding values calculated from band-wise means of transmittance by:

$$\chi'_{a-b} = ln(E[e^{\chi_{a-b}}]) \qquad \text{Eq. 6.2}$$

Clear discrepancies between band-wise contact numbers between these two methods illustrates the noncommutative property of the natural logarithm (ln[x]) and mean (E[x]) functions (Figure E.4). The assumption of their commutativity is used when mean band-wise contact number is estimated as the natural logarithm of mean band-wise transmittance, as is common practice in analysis of binary hemispherical images. Error introduced by this assumption has ramifications for LAI_{2000}, calculated from contact numbers estimated under this assumption.

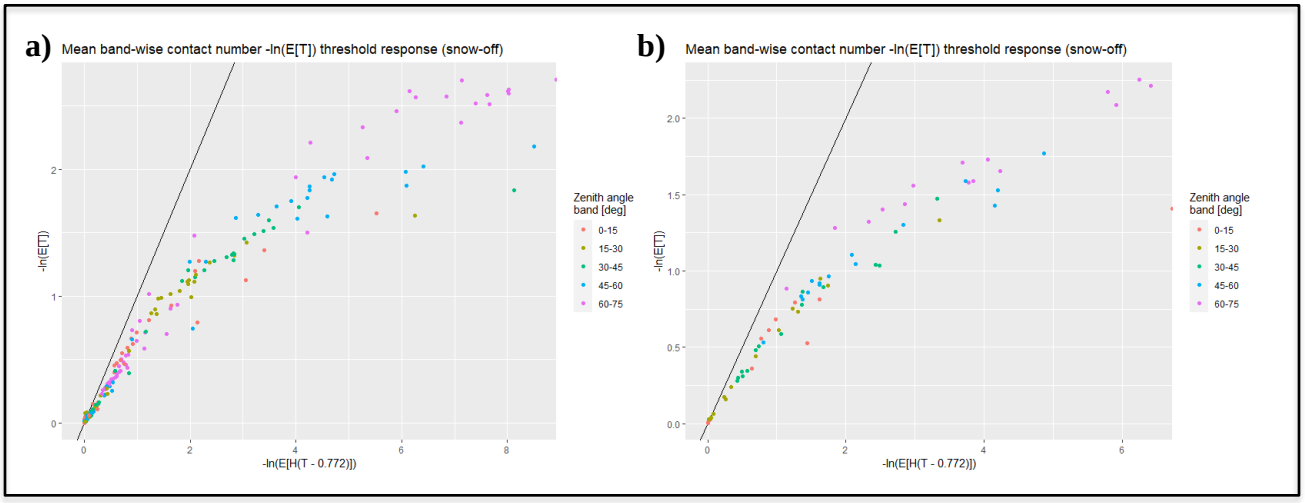

Figure E.3: Band-wise contact numbers calculated from mean thresholded transmittance (x-axis) vs. mean transmittance (y-axis) for voxel ray sampling optimization products, for (a) snow-on and (b) snow-off canopy conditions. Transmittances were thresholded at T = 0.772, represented by the Heaviside function H(T – 0.772).

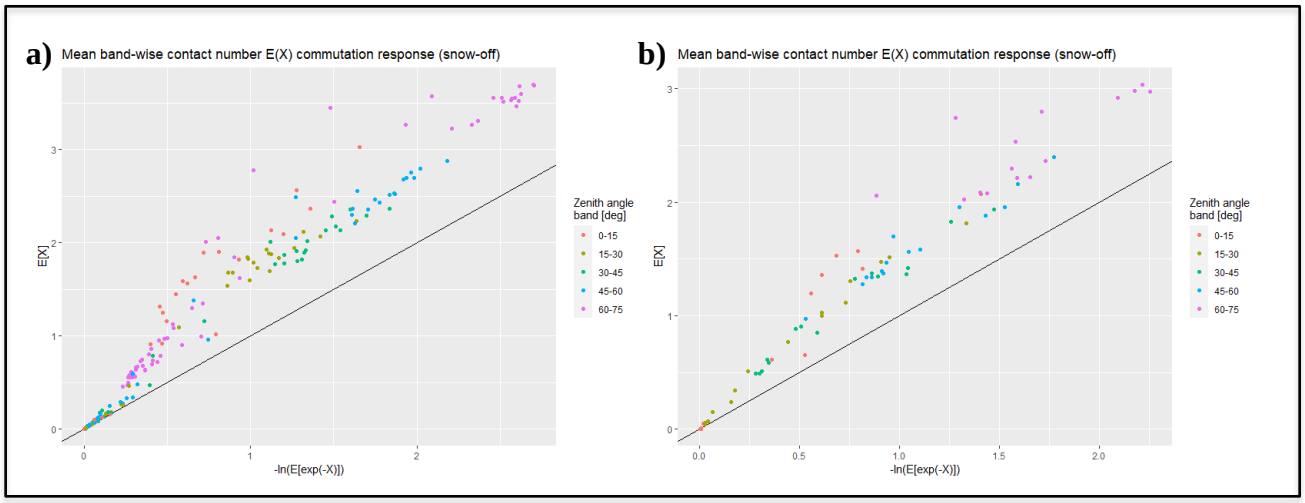

Figure E.4: Band-wise contact numbers calculated by the natural logarithm of mean band-wise light transmittance (x-axis) compared with mean band-wise contact number (y-axis), for (a) snow-on and (b) snow-off canopy conditions, calculated from voxel ray sampling products collocated with corresponding hemispherical photography.

To understand what role the thresholding and commutation effects had on the methodological comparison of synthetic hemispheres in Section 3.4.2 and Figure 3.4, light transmittance metrics which rely on these two assumptions were compared with those that did not. Both sets of metrics were calculated from voxel ray sampling products calculated over a 25 cm square grid across the forest plot, under snow-off canopy conditions. Visible discrepancies among all metrics show the combined effects of the thresholding and commutation assumptions (Figure E.5). Visual similarities between Figure E.5 and Figure 3.4 suggest that differences between synthetic the two lidar methods assessed in Section 3.4.2 may be heavily influences by the use of these two assumptions in the point reprojection methodology. These assumptions are also used in the analysis of the hemispherical photographs used for validation of the two methods.

To provide a better comparison of the methodological differences outside of these two assumptions between the two lidar synthetic hemisphere methods, light transmittance metrics were compared from the two methods which both make use of the thresholding and commutation assumptions. Reduced bias was observed between all three metrics in Figure E.6, contrasting the disagreements shown for the unthresholded voxel ray sampling estimates in Figure 3.4. As both methods in this case use the threshold and commutation assumptions, the consequent errors are expected to be similar for both, allowing for visual comparison of additional methodological differences between the two methods.

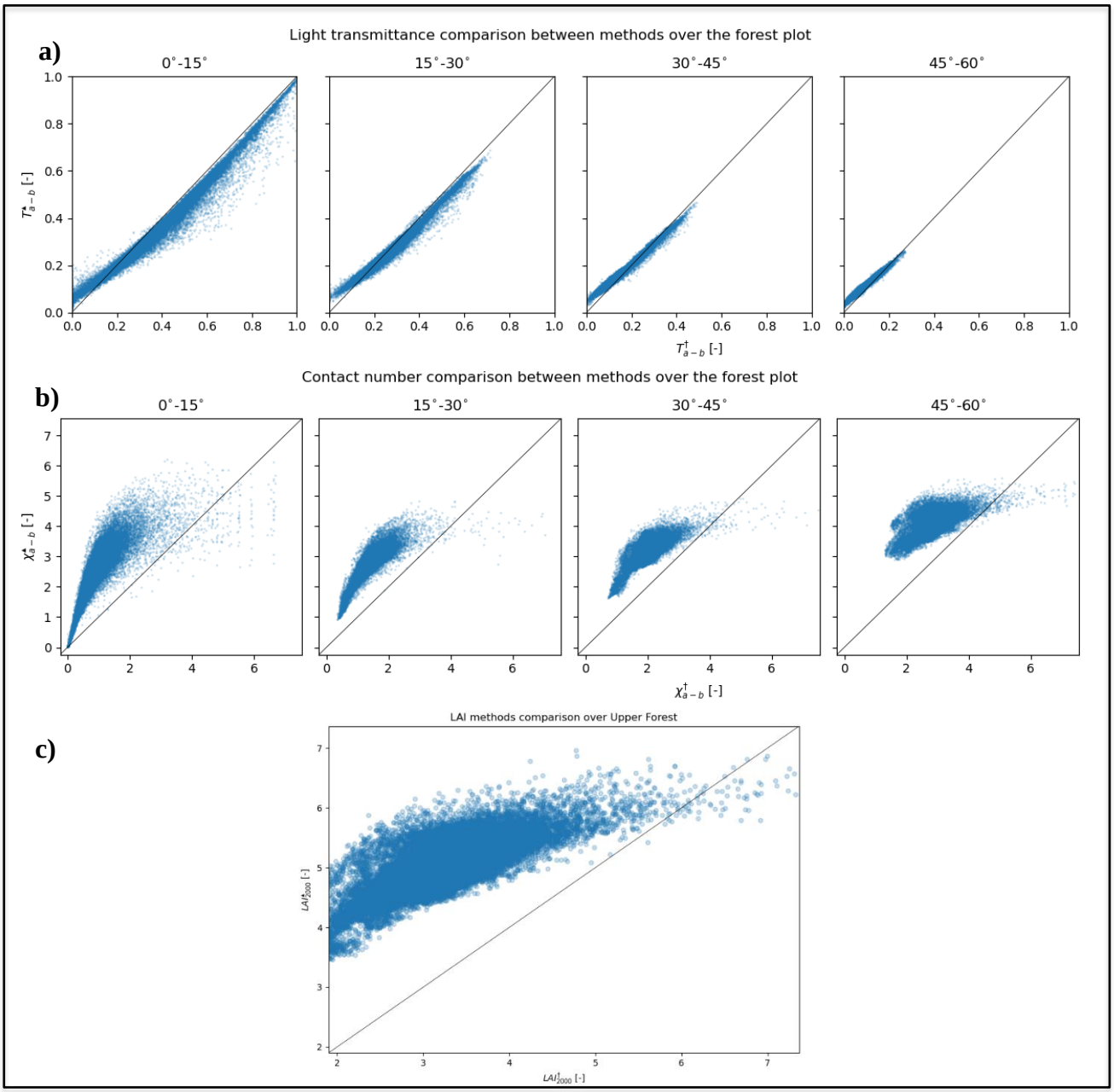

Figure E.5: Comparisons of (a) light transmittance and (b) contact number estimates from synthetic hemispheres generated by thresholded voxel ray sampling of lidar (x-axis) with those from unthresholded voxel ray sampling of lidar (y-axis) for each of the four zenith angle analysis bands, with 1-to-1 line. (c) Comparison of leaf area index (LAI_{2000}) between the two methods, with 1-to-1 line.

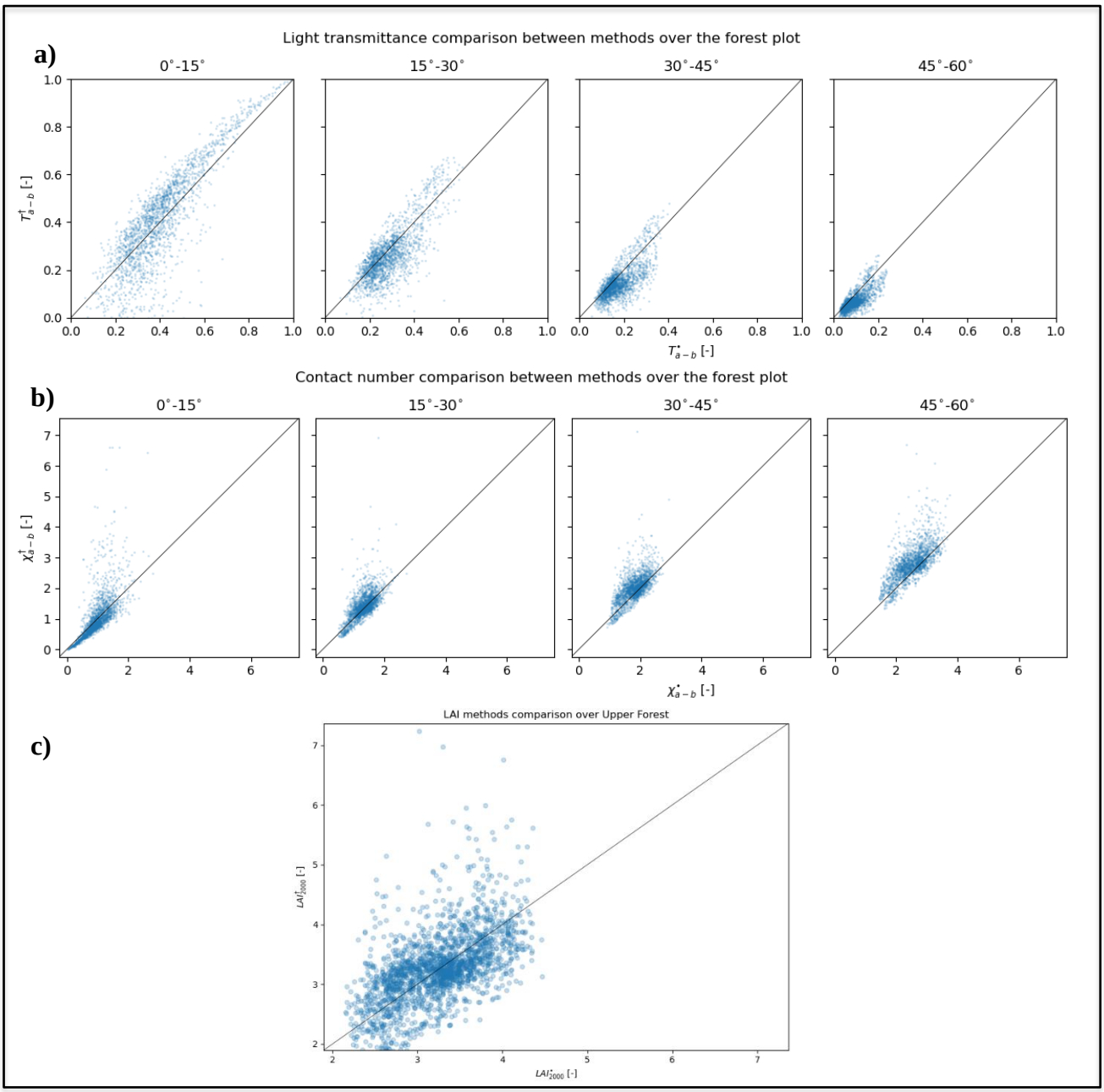

Figure E.6: Comparisons of (a) light transmittance and (b) contact number estimates from synthetic hemispheres generated by lidar point cloud reprojection (x-axis) with those from thresholded voxel ray sampling of lidar (y-axis) for each of the four zenith angle analysis rings, with 1-to-1 line. (c) Comparison of leaf area index (LAI_{2000}) between the two methods, with 1-to-1 line.

Appendix F: Sensitivity analysis of Gaussian snowfall model parameters

The optimization landscapes of Gaussian snowfall model parameters σ and ω^* were calculated using one-at-a-time (OAT) analysis. This was done to visually illustrate the differences in parameter confidence between the two storms. Landscapes for storm 1 (Figure F.1), storm 2 (Figure F.2) showed similar patterns, with the primary difference being a sharper curve and therefore greater confidence in ω^* for storm 2 than for storm 1. Landscapes for SWE_f for 21 Feb. 2019 (Figure F.3) showed similar patterns to storm 1, but with much higher maximum R^2 values.

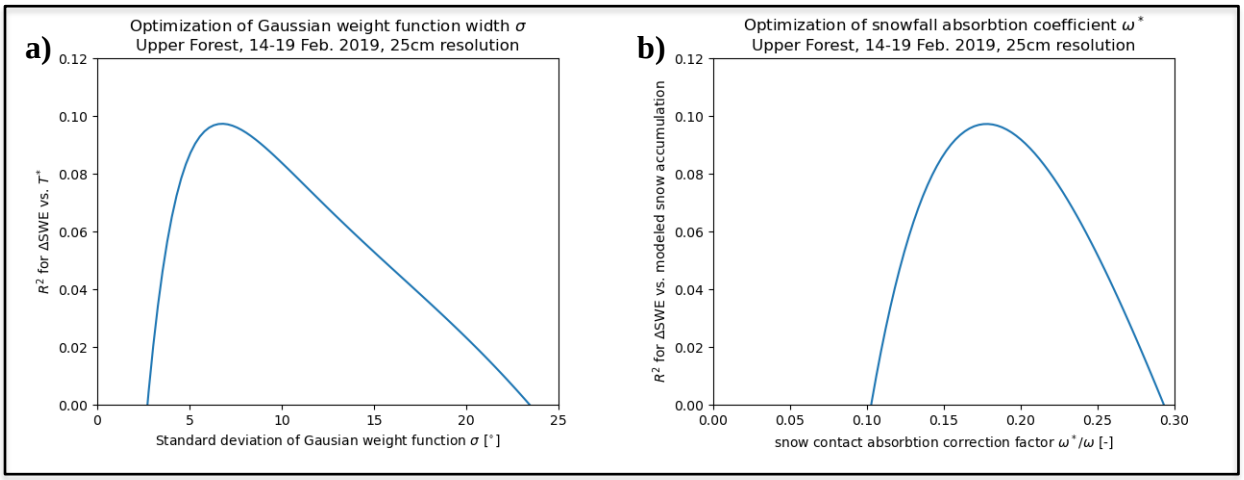

Figure F.1: Optimization landscape of (a) standard deviation (σ) and (b) snow contact absorption coefficient (ω^*) for ΔSWE_f for Storm 1.

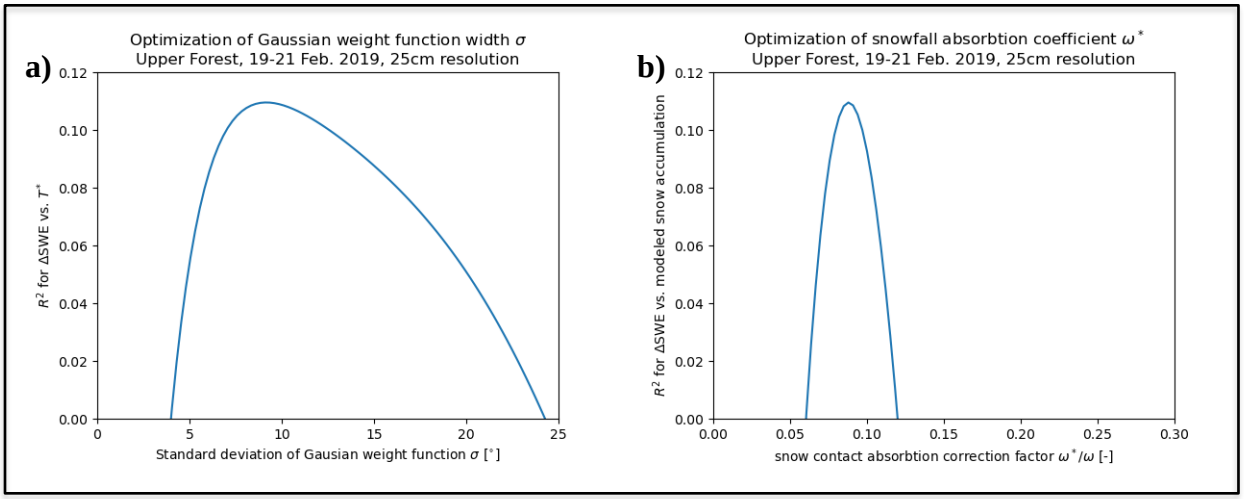

Figure F.2: Optimization landscape of (a) standard deviation σ and (b) snow contact absorption coefficient ω^* for ΔSWE_f for Storm 2.

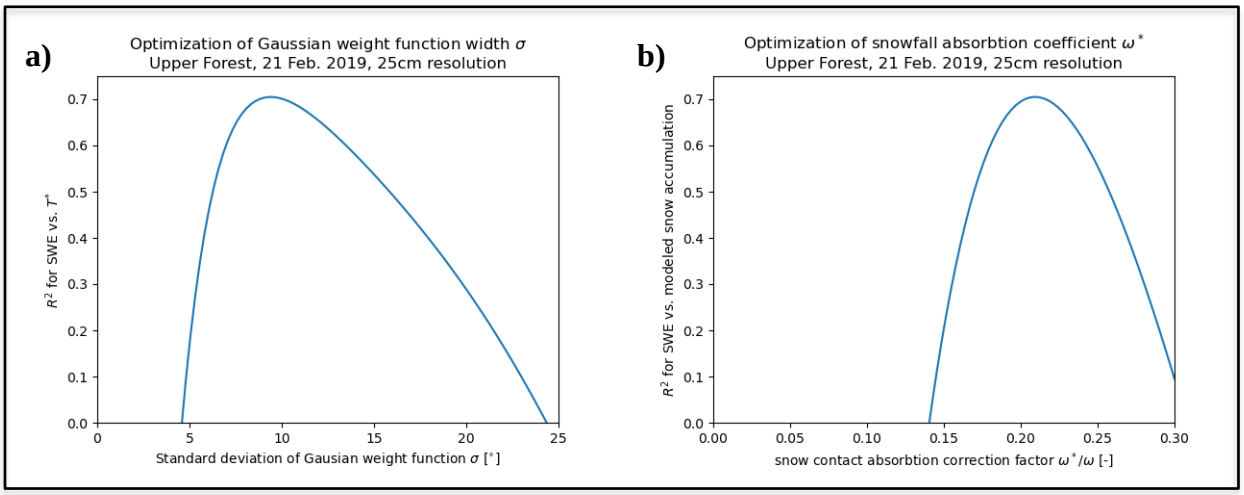

Figure F.3: Optimization landscape of (a) standard deviation σ and (b) snow contact absorption coefficient ω^* for SWE_f for 21 Feb. 2019.